ACS APPLIED

ENERGY MATERIALS © Cite This: ACS Appl. Energy Mater. XXXX, XXX. XXX.

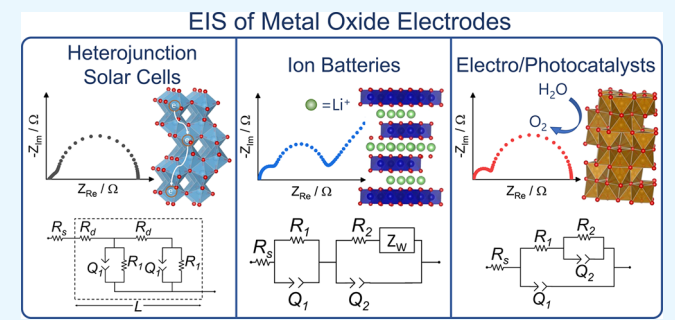
www.acsaem.org

# **Electrochemical Impedance Spectroscopy of Metal Oxide Electrodes** for Energy Applications

Alexandria R. C. Bredar, Amanda L. Chown, Andricus R. Burton, and Byron H. Farnum\*

Department of Chemistry and Biochemistry, Auburn University, Auburn, Alabama 36849, United States

ABSTRACT: Metal oxides have been of great importance to the development of energy conversion and storage technologies including heterojunction solar cells, Li-ion batteries, and electrocatalysts/photocatalysts for water splitting and CO2 reduction. The role of metal oxides in these devices has been diverse, from charge transport layers to catalytic surfaces to protective blocking layers. Understanding the fundamental structural and electronic properties of these materials will continue to allow for advancement in the field of renewable energy. Electrochemical impedance spectroscopy (EIS) is one of the most utilized methods to characterize these electrodes in the context of energy applications. The utility of EIS stems



from its ability to differentiate multiple interfaces (i.e., solid/electrolyte, solid/solid) within devices on the basis of their frequency response to a modulated potential and the subsequent decoupling of resistive and capacitive circuit components. In this review, the fundamental theory of EIS is first described with a physical and mathematical basis, followed by a discussion of equivalent circuit modeling. The review then covers examples from the literature where EIS has been particularly important in the understanding of electronic properties related to metal oxide electrodes within energy conversion and storage devices. A specific focus is placed on metal oxides that are used as heterojunction solar cells, ion batteries, and photocatalysts/ electrocatalysts. Common themes are discussed within each application such as the study of electron and hole diffusion in solar cells, the dependence of recombination reactions and catalysis on surface defect/trap states for solar cells and photocatalysts, and the formation of passivation layers at the solid electrolyte interface in Li-ion batteries.

KEYWORDS: impedance, metal oxide, solar energy conversion, energy storage, photoelectrocatalysis

### 1. INTRODUCTION

Electrochemical impedance spectroscopy (EIS) is a versatile technique for the study of electrode materials relevant to energy applications such as heterojunction solar cells, Li-ion batteries, and electro/photocatalysis. 1-6 Metal oxide electrodes have been highly studied in these fields due to their stability, ease of synthesis, and diverse range of structures and metal atoms which allow for tunable applications based on optoelectronic properties. Metal oxides can behave as insulators, semiconductors, or metals depending on their atomic nature, crystal structure, and extent of doping. In general, the conduction band for metal oxides is defined by metal-based s- and d-orbitals depending on the metal atom. The symmetry of these orbitals along with the crystal structure of the oxide determine the extent of overlap with strong overlap leading to larger electron mobilities. The valence band of metal oxides consists of largely localized oxygen p-orbitals. This makes p-type conduction through metal oxides difficult without mixing metal d-orbital character into the valence band such as in the case of NiO, Cu<sub>2</sub>O, and copper delafossites.

For energy applications, metal oxides with semiconductor and metallic properties are of interest because of the need to conduct charge through an electrical device. These materials are therefore found ubiquitously throughout energy applica-

tions including solar-to-electrical and solar-to-fuel energy conversion as well as energy storage in batteries and supercapacitors. For example, wide band gap semiconductor metal oxides such as TiO2, ZnO, and NiO have been heavily studied as n-type and p-type electrodes in heterojunction solar cells such as dye-sensitized solar cells (DSSCs), organic photovoltaics (OPV), quantum-dot-sensitized solar cells (QDSCs), and perovskite solar cells (PSCs).<sup>7-11</sup> Likewise, narrow band gap semiconductor metal oxides such as Fe<sub>2</sub>O<sub>3</sub>, Cu<sub>2</sub>O, BiVO<sub>4</sub>, and CuFeO<sub>2</sub> have been studied as direct light absorbers capable of driving photocatalytic H<sub>2</sub>O oxidation, H<sup>+</sup> reduction, and CO<sub>2</sub> reduction. <sup>2,5,12,13</sup> Metal oxides with more metallic character have shown promise in electrocatalytic applications, where certain spinels and perovskites have been targeted toward electrochemical fuel production. In terms of electrical energy storage, metal oxides are heavily featured as cathodes in Li-ion batteries where the crystal structures of materials such as LiCoO  $_2$  and LiMn  $_2O_4$  create ion channels for lithium intercalation.  $^{3,14-17}$ 

Special Issue: Young Investigator Forum

Received: October 5, 2019 Accepted: December 17, 2019

As an alternating current (AC) technique, EIS is capable of distinguishing between resistive and capacitive responses of metal oxide interfaces based on the frequency dependence of the observed current. Central to this is the fact that the impedance of a resistor does not depend on the frequency of the modulated voltage; however, the impedance of a capacitor is inversely proportional to this frequency. Therefore, EIS offers the ability to study these components independently over a selected voltage range based on a frequency dependent current response. By comparison, a direct current technique such as cyclic voltammetry (CV) shows capacitive and resistive features simultaneously, such that differentiating the two can sometimes be difficult.

Figure 1 shows the simplest equivalent circuit used to model metal oxide interfaces, called a Randles circuit. The parallel

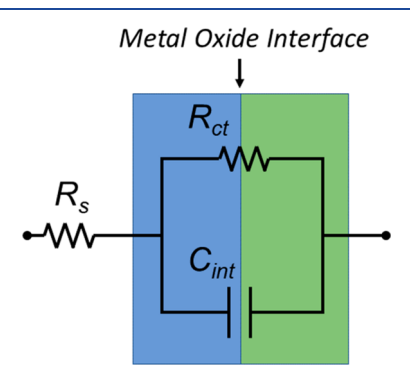


**Figure 1.** Simple circuit model which describes the flow of current across a metal oxide interface. Faradaic current is correlated with a charge transfer resistance  $(R_{\rm ct})$  while non-Faradaic current is correlated with an interfacial capacitance  $(C_{\rm int})$ . A series resistance term  $(R_{\rm s})$  is shown to represent resistance due to wires, contacts, and solutions which complete the circuit.

combination of charge transfer resistance ( $R_{\rm ct}$ ) and interfacial capacitance ( $C_{\rm int}$ ) describes the flow of Faradaic and non-Faradaic current through the interface, respectively. The nature of the metal oxide interface may be a solid/solid or solid/liquid interface where one side is the metal oxide electrode and the other is a dissimilar material depending on the application. For metal oxide electrodes in energy applications,  $R_{\rm ct}$  is associated with electron transfer reactions such as electron—hole recombination with a chromophore/semiconductor or catalysis by metal oxide surface sites. Interfacial capacitance is an equivalent capacitance that considers the series combination of

the capacitances for the metal oxide and the dissimilar material with which it is in contact. This material may be an electrolyte in either a solution or solid/gel form or a semiconductor as in the case of QDSCs, OPVs, and PSCs.

Here we present a review of how EIS has been used to characterize metal oxide electrodes specifically used in energy applications. Other reviews of EIS in the context of DSSCs, emerging photovoltaics, and thin films have previously been published. 1,6,18 We specifically discuss EIS in the context of modulating an applied potential and measuring the magnitude and phase angle associated with the resulting current. This is by far the most common method used in the field of EIS; however, it should be noted that similar methods of modulating an illumination intensity, such as intensity modulated photocurrent and photovoltage spectroscopies (IMPS/IMVS), have been reported but are not discussed here.<sup>20,21</sup> The applications covered in this review include heterojunction solar cells such as DSSCs, QDSC, and PSCs; ion batteries such as Li-ion, Na-ion, and Zn-ion; and electro/ photocatalysts used to drive water oxidation and oxygen reduction reactions. In each case, the discussion is focused on what properties of the metal oxide can be elucidated by EIS. Common themes emerge within each application such as the study of electron (e<sup>-</sup>) and hole (h<sup>+</sup>) diffusion in solar cells, the dependence of recombination reactions and catalysis on surface defect/trap states for solar cells and photocatalysts, and the formation of passivation layers at the solid electrolyte interface in Li-ion batteries. Particular interest is placed on morphological changes to the electrode materials and how EIS can be used to better understand these complex interfaces. A high degree of attention is also placed on the modeling of EIS data using equivalent circuits, which can often be the most debated aspect of EIS studies, to shed light on which models are most effective at describing the observed data. To do this, we first begin with a brief background on EIS as an AC technique, discussing how different circuit elements such as resistors, capacitors, and constant phase elements are used to describe EIS data.

#### 2. EIS BACKGROUND

EIS is fundamentally an AC technique in which an applied potential E(t) is modulated over time with a small amplitude (| $E_0$ |  $\sim 5-10$  mV) at a controlled frequency ( $\omega$ ) according to eq 1. Here,  $\omega$  is an angular frequency defined by  $\omega = 2\pi f$ , and f is the frequency in Hz. The small perturbation in potential

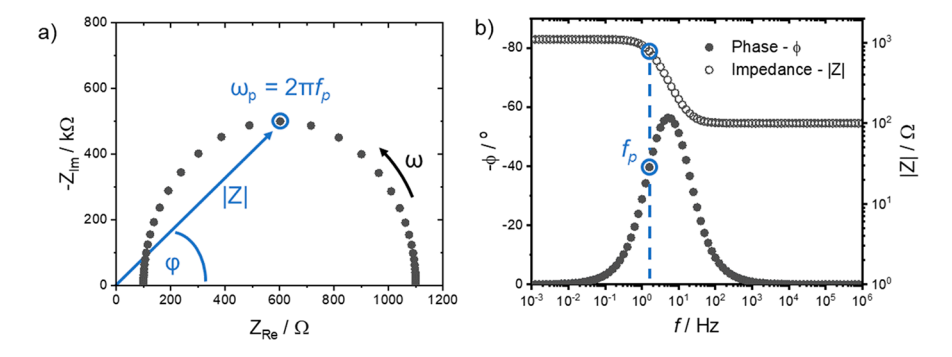


Figure 2. (a) Nyquist and (b) Bode plots representing the same EIS data simulated by a the circuit shown in Figure 1 ( $R_s = 100 \Omega$ ,  $R_{ct} = 1000 \Omega$ ,  $C_{int} = 100 \mu F$ ). In the Nyquist plot, the modulus |Z| and phase angle  $\varphi$  define the position of each frequency dependent data point in a complex plane. In the Bode plot, |Z| and  $\varphi$  are plotted against the modulation frequency. The angular frequency associated with the  $-Z_{Im}$  peak in the Nyquist plot is labeled  $\omega_p$  and corresponds to points labeled  $f_p$  in the Bode plot.

defined by  $|E_0|$  is required to ensure linear behavior of the current following the Butler–Volmer model.<sup>22</sup> The measured current response I(t) is matched in frequency but offset by a phase angle  $(\varphi)$  depending on the parameters of the electrochemical circuit, eq 2. Impedance is defined as the AC analogue to resistance and is thus related to the alternating potential and current through Ohm's law shown in eq 3 and is expressed in units of ohms  $(\Omega)$ .

$$E(t) = |E_0|\sin(\omega t) \tag{1}$$

$$I(t) = |I_0|\sin(\omega t + \varphi) \tag{2}$$

$$Z(\omega) = E(t)/I(t) \tag{3}$$

In a typical EIS experiment, the modulation frequency is sampled over a wide range ( $\sim$ 1 mHz to 1 MHz) for a fixed applied potential ( $E_{\rm app}$ ) on top of which the small modulation amplitude  $|E_0|$  is applied such that  $E(t)=E_{\rm app}+|E_0|\sin(\omega t)$ . When the frequency range is completed,  $E_{\rm app}$  is shifted to a new value and the process is repeated. For a single potential, experiments may take anywhere from a few seconds to tens of minutes depending on the frequency range of interest. Therefore, it is not uncommon for experiments to take many hours to fully collect EIS data over a wide potential range and/or with a small step size between applied potentials.

Collected data is then interpreted using a variety of plots. The most important is the Nyquist plot, in which impedance is plotted as a complex number  $(j = \sqrt{-1})$  according to eq 4 with  $Z_{\rm Im}$  (Z") along the y-axis and  $Z_{\rm Re}$  (Z') along the x-axis (Figure 2). The characteristic semicircle arc arises from the parallel combination of a resistor and capacitor described in Figure 2. Each data point in a Nyquist plot represents a different frequency with  $\omega$  decreasing from left to right. At infinitely low frequencies, the applied potential is essentially constant, and this condition is considered the DC limit where  $Z_{Re} = R_s + R_{ct}$ . This condition is often relevant when relating EIS data to other DC electrochemical techniques such as cyclic voltammetry. For each frequency, the impedance is defined by a vector originating from the origin with magnitude |Z| and phase angle  $\varphi$ . These two terms are defined with respect to  $Z_{Re}$  and  $Z_{Im}$  by eqs 5 and 6.

$$Z(\omega) = |Z|(\cos(\varphi) - j\sin(\varphi)) = Z_{Re} - jZ_{Im}$$
 (4)

$$|Z| = (Z_{Re}^2 + Z_{Im}^2)^{1/2}$$
 (5)

$$\tan \varphi = Z_{\rm Im}/Z_{\rm Re} \tag{6}$$

Another method of graphing EIS data is the Bode plot, which is a combination of two plots that show the magnitude of impedance |Z| and the phase angle  $\varphi$  on the y-axis and the modulation frequency f along the x-axis. Again, each data point represents a unique frequency which can now be correlated directly with |Z| and  $\varphi$ . The Bode plot therefore allows for the frequency dependence of impedance to be more clearly observed than what is shown in the Nyquist plot. Sometimes, |Z| and  $\varphi$  are combined into a single Bode plot with two different y-axes while at other times they are separated into Bode-Z and Bode-phase plots. A simulated Bode plot is shown in Figure 2 with the same parameters used in the Nyquist plot for comparison. Note that although the peak shape observed for  $\varphi$  results from the semicircle arc shown in the Nyquist plot, the frequencies associated with each peak are not identical. The peak in the Nyquist plot is directly related to  $R_{ct}$  and  $C_{int}$ 

at the electrode surface according to  $f_{\rm p}=1/R_{\rm ct}C_{\rm int}$  where  $R_{\rm ct}C_{\rm int}$  is known as the time constant for the parallel circuit. The peak in the Bode-phase plot, however, does not correlate with  $f_{\rm p}$  and can sometimes be difficult to interpret directly due to the presence of additional circuit elements such as series resistance. We caution the use of Bode plots to directly interpret EIS data and instead encourage all data to be fit according to a well-defined circuit model (discussed further below).

EIS data can also be interpreted in terms of frequency dependent and potential dependent capacitance. Just like impedance, capacitance can be defined as a complex number and determined from  $Z(\omega)$  based on eq 7. Plotting  $C_{\rm Re}$  vs frequency reveals direct information about capacitance at the electrode surface. This method of analysis has become particularly useful in the area of PSCs where accumulation of mobile ions (e.g., iodide, methylammonium) in the perovskite material at the interface with metal oxide electrodes results in large capacitances at low-frequencies. <sup>23–27</sup> Figure 3 shows an

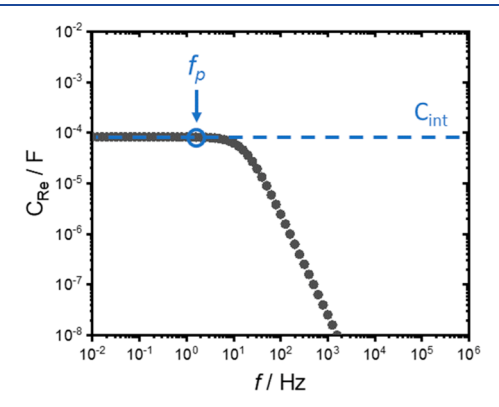


**Figure 3.** Capacitance vs frequency plot showing a plateau at  $C_{\rm int} = 100~\mu{\rm F}$ .  $C_{\rm Re}$  was calculated from eq 7 based on the same data simulated in Figure 2. The peak frequency observed in the Nyquist plot is shown here for reference at  $f_{\rm p}$ .

example plot of  $C_{\text{Re}}$  vs frequency for the same data shown in Figure 2. Note that the plateau in capacitance occurs at  $C_{\text{Re}}$  =  $100 \, \mu\text{F} = C_{\text{int}}$ , thus allowing for the interfacial capacitance to be obtained directly from the plot.

$$C(\omega) = 1/j\omega Z(\omega) = C_{Re} - jC_{Im}$$
 (7)

**2a. EIS Modeling.** In order to understand and extract meaningful information from EIS data, it must be fit to an equivalent circuit model which combines fundamental elements such as resistors, capacitors, inductors, constant phase elements, and diffusion elements. The impedance of each element is discussed below, and these are summarized in Table 1.

Resistors. Resistors are important elements which describe Faradaic charge transfer reactions across interfacial layers. The prime example is electron transfer from the electrode surface into an electrolyte solution or vice versa. The term resistance may also be used to describe movement of mobile charges through solid and liquid phases; however, these features are best modeled using diffusive elements described below. The impedance of a resistor  $(Z_{\rm R})$  is simply equal to its resistance in units of  $\Omega$ ,  $Z_{\rm R}=R$ .

Capacitors. The non-Faradaic charge which accumulates at solid/solid and solid/liquid interfaces is modeled as a capacitance. Important interfaces include contacts between

ACS Applied Energy Materials Forum Article

Table 1. Summary of Circuit Elements Used to Model EIS

| Resistor (R)                       |                             | $Z_R = R$                                            |
|------------------------------------|-----------------------------|------------------------------------------------------|
| Capacitor (C)                      |                             | $Z_{\rm C} = 1/j\omega{\rm C} = -j/\omega{\rm C}$    |
| Inductor (L)                       |                             | $Z_L = j\omega L$                                    |
| Constant Phase Element (CPE)       | $\rightarrow$ $\rightarrow$ | $Z_{\text{CPE}} = 1/(j\omega)^{\beta}Q$              |
| Warburg Diffusion (W) <sup>a</sup> | $ Z_W$                      | $Z_{\rm W} = \frac{\sigma\sqrt{2}}{(j\omega)^{1/2}}$ |

"Only the equation for infinite diffusion is shown. See eqs 8 and 9 for finite diffusion.

adjacent metal oxide particles or nanocrystals, contacts between a metal oxide and a conductive substrate, and the double-layer which forms at the solid/solution interface. In the latter case, measured capacitance is often correlated with the density of electronic states at the metal oxide surface. The impedance of a capacitor  $(Z_{\rm C})$  varies inversely with  $\omega$  via the relation  $Z_{\rm C}=1/j\omega C=-j/\omega C$ , and therefore,  $Z_{\rm C}$  is largest at low frequencies and smallest at high frequencies.

Inductors. Inductors often need to be included in EIS models due to metallic contacts or leads being too close to one another. This is sometimes the case in small devices where anodes and cathodes are in close proximity as is the case in heterojunction solar cells where both electrodes are sandwiched together and only separated by a small distance. The impedance of an inductor  $(Z_L)$  is equal to  $j\omega L$ . Thus, the impedance of an inductor is exactly opposite that of a capacitor. It is for this reason that the signature feature of an inductive circuit element is EIS data which crosses into the lower quadrant of the Nyquist plot as  $Z_{Im}$  becomes positive.

Constant Phase Elements (CPEs). Inhomogeneities in the surface of metal oxide electrodes result in nonideal capacitance in the double-layer at the solid/electrolyte interface. For this reason, CPEs are routinely used in place of pure capacitors to model this interfacial layer. The impedance of a CPE is defined by the relation  $Z_{\text{CPE}} = 1/(j\omega)^{\beta}Q$  where Q is a nonideal capacitance and has units of F s<sup> $\beta$ -1</sup> and  $\beta$  is an ideality factor which ranges from 0 to 1. When  $\beta$  = 1,  $Z_{\text{CPE}} = Z_{\text{C}}$ , and the interface is said to behave as an ideal capacitor (Q = C). Normally,  $\beta$  is found to be in the range 0.8–1, indicating nonideal behavior that is attributed to surface roughness and irregularities in surface termination, porosity, and complexity in the double-layer structure.

Warburg Diffusion. Diffusion of mobile charges within metal oxide electrodes and in solution is an important factor in EIS data analysis. The impedance of diffusion  $(Z_W)$  is called Warburg diffusion and can be described by finite and infinite diffusion models. Choosing the right form can be important for accurately describing the data. Equations 8 and 9 show two equations which describe Warburg diffusion in a finite thickness layer (i.e., a metal oxide electrode or a solution phase pore) for the case of open and shorted contacts at the solid/electrolyte interface, respectively. Sometimes these contacts are referred to as reflecting (open) and absorbing (shorted) boundaries and are discussed in more detail below. 1,28,29 The two equations are similar and only differ in the use of either coth(x) and tanh(x) functions to describe the impedance. The  $\omega^{1/2}$  dependence gives rise to a characteristic linear relationship between  $-Z_{Im}$  and  $Z_{Re}$  for the Nyquist plot with slope = 1 and  $\varphi = 45^{\circ}$ . The  $\sigma$  term describes the resistance associated with diffusion as a function of

concentration of charge carriers and their diffusion coefficients. Equation 10 provides an expression for  $\sigma$  in terms of solution phase electrolyte species. The term  $L/D^{1/2}$  describes the lifetime for diffusion  $(\tau_{\rm d}^{-1/2}=L/D^{1/2})$  where L is the finite thickness of the diffusion layer and D is the diffusion coefficient of the mobile charge carrier. The diffusion lifetime is often called a carrier lifetime when the mobile species is e or h<sup>+</sup> charges. If L is known, then a diffusion coefficient for charge diffusion can be obtained. These parameters become important for describing diffusion through semiconductor metal oxides. In the case of electroactive or electro-inactive ions in fluid solution, the diffusion layer is often very large, and eqs 8 and 9 are condensed to a common limiting form shown in eq 11. This form of Warburg diffusion is most often observed with metallic electrodes where the applied potential is sufficient such that electron transfer at the metal oxide interface is not rate limiting, and therefore, current becomes dependent on diffusion of electroactive species to the surface. In this case, a diffusion coefficient of the mobile ion can be measured from the  $\sigma$  term.

$$Z_{WO} = \frac{\sigma\sqrt{2}}{(j\omega)^{1/2}} \coth\left[\frac{L}{D^{1/2}}(j\omega)^{1/2}\right]$$
(8)

$$Z_{\text{WS}} = \frac{\sigma\sqrt{2}}{(j\omega)^{1/2}} \tanh\left[\frac{L}{D^{1/2}}(j\omega)^{1/2}\right]$$
(9)

$$\sigma = \frac{RT}{n^2 F^2 A \sqrt{2}} \left( \frac{1}{C_{\text{ox}} D_{\text{ox}}^{1/2}} + \frac{1}{C_{\text{red}} D_{\text{red}}^{1/2}} \right)$$
(10)

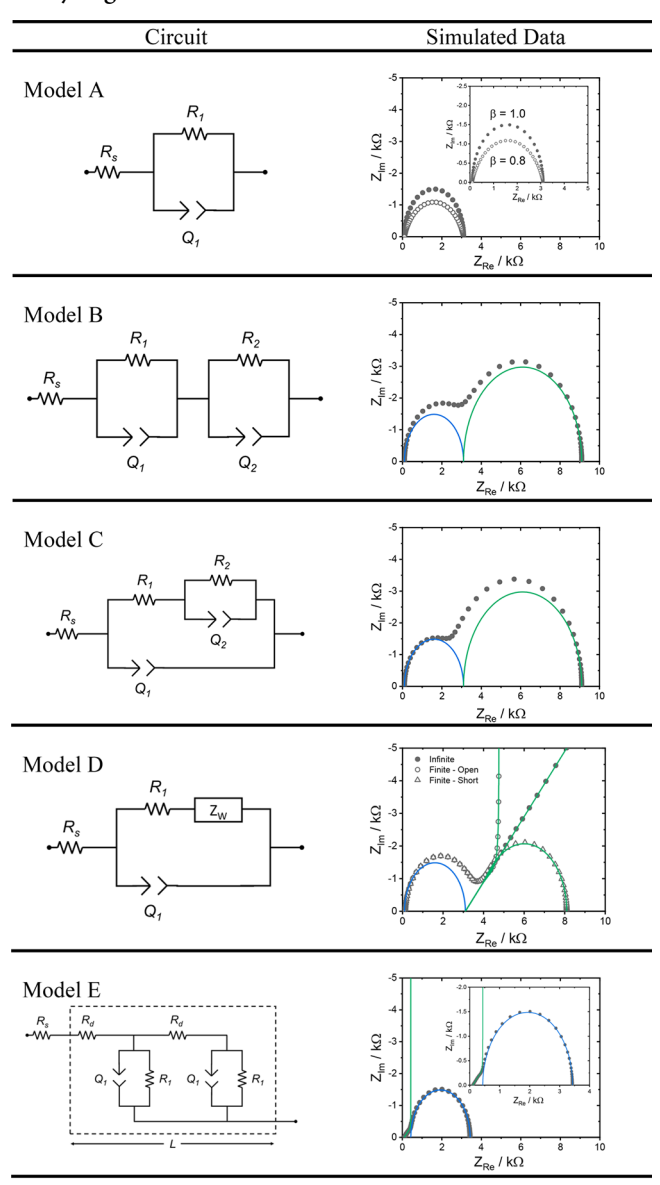
$$Z_{\rm W} = \frac{\sigma\sqrt{2}}{(j\omega)^{1/2}} \tag{11}$$

Equivalent Circuits. Assembling fundamental circuit elements together into a logical and physically relevant circuit which describes the flow of charge across metal oxide interfaces is often the most challenging and debatable topic within the field of EIS. The challenge comes from the fact that many different equivalent circuits will often provide equally good fits to EIS data. Therefore, physical relevancy of the model and supporting characterization of the electrode material are strong requirements for the chosen model to be accurate.

A wide range of equivalent circuits have been used to model EIS data for metal oxide electrodes with many of the models depending on the application. Table 2 shows a collection of common equivalent circuits along with simulated Nyquist plots for reference. In each case, CPEs are used in place of ideal capacitors as is often the case for metal oxide electrodes. For simplicity,  $\beta=1.0$  was used for all simulations except for model A which provides a comparison between  $\beta=1.0$  and 0.8. Each model is briefly discussed below.

*Model A.* The simplest circuit, and often the most employed, is called a Randles circuit. The Randles circuit captures the most fundamental description of an electrode surface where both Faradaic (charge transfer resistance,  $R_1$ ) and non-Faradaic (double-layer capacitance,  $Q_1$ ) currents flow through the solid/electrolyte interface. These two elements are represented in parallel to reflect the fact that total current is the sum of Faradaic and non-Faradaic pathways. The  $R_{\rm s}$  term is included in series to account for any and all resistances associated with solution resistance, wires, clips, or other

Table 2. Summary of Common Equivalent Circuits for Analyzing EIS Data of Metal Oxide Electrodes<sup>a</sup>



"Values used to generate simulations:  $R_1=3$  k $\Omega$ ,  $R_2=6$  k $\Omega$ ,  $Q_1=1$   $\mu$ F s $^{\beta-1}$ ,  $Q_2=10$   $\mu$ F s $^{\beta-1}$ ,  $R_d=1$  k $\Omega$ ,  $\sigma=5$  k $\Omega$  s $^{-1/2}$ ,  $L/D^{1/2}=1$  s $^{1/2}$ ,  $\beta=1.0$  unless otherwise indicated. Blue lines show specifically where  $R_1$  and  $Q_1$  terms appear in the overall data. Green lines show how  $R_2$ ,  $Q_2$ ,  $R_d$ , or  $Z_W$  terms appear in the data.

contacts. The total impedance of an equivalent circuit is calculated by Kirchhoff's laws where Z is treated as a resistance. Therefore, the total impedance  $Z(\omega)$  of a Randles circuit is shown in eq 12. The real and imaginary components of  $Z(\omega)$  are then solved algebraically. Even for the simple Randles circuit,  $Z_{\rm Re}$  and  $Z_{\rm Im}$  are quite complicated functions. Therefore, computer software is routinely used to calculate  $Z_{\rm Re}$  and  $Z_{\rm Im}$  on the basis of the given equivalent circuit model.

$$Z(\omega) = R_s + \frac{R_1}{1 + R_1 Q_1 (j\omega)^{\beta}} = Z_{Re} - jZ_{Im}$$
 (12)

Given the frequency dependence of capacitive impedance ( $Z_{\rm C}$  or  $Z_{\rm CPE}$ ), the semicircle arc of the Nyquist plot shown in Figure 2a can be readily explained. At high frequency,  $Z_{\rm C} \to 0$ 

and all current is non-Faradaic with  $Z(\omega)=R_{\rm s}=100~\Omega$  as is shown in the Bode-Z plot of Figure 2b. However, as frequency is decreased,  $Z_{\rm C}$  becomes larger and forces current toward the Faradaic channel; thus,  $Z(\omega)$  increases and forms the characteristic arc shape in the Nyquist plot. At the other extreme of infinitely small frequency,  $Z_{\rm C}\to\infty$ ; therefore,  $Z(\omega)=R_{\rm s}+R_{\rm ct}=1100~\Omega$ , and  $R_{\rm ct}$  is defined by the width of the arc along the  $Z_{\rm Re}$ -axis. The plateau in |Z| at low frequency in Figure 2b is also diagnostic of this condition. At low frequency, all current passing through the solid/electrolyte interface is Faradaic. This situation is similar to holding an applied potential for an extended period of time in a chronoamperometry experiment where the non-Faradaic current has decayed to zero at very early times.

Table 2 provides a comparison of simulated data for the Randles circuit with an ideal ( $\beta=1$ ) and nonideal ( $\beta=0.8$ ) capacitor using a CPE in place of the capacitance. For an ideal capacitor, the capacitance can be calculated directly from the frequency associated with the peak in the Nyquist plot  $\omega_p$ . This point is indicated in Figure 2a. The frequency  $\omega_p$  is directly related to  $R_1$  and  $C_1$  (=  $Q_1$ ) through the relation  $\omega_p=(R_1C_1)^{-1}=1/\tau$  where  $\tau$  is the characteristic RC time constant for the parallel circuit. Often, the EIS literature will discuss Nyquist data in terms of time constants for each observed semicircle. For a nonideal capacitor, a depressed semicircle is observed in the Nyquist plot, and the peak observed in the Bode-phase plot is spread over a wider range of frequencies. This is called frequency dispersion and requires fitting EIS data to an equivalent circuit to accurately measure values such as  $\beta$  and

Model B. The simple Randles circuit can be extended to include multiple parallel RIIC circuits in series to account for multiple semicircle arcs observed in the Nyquist plot. Model B considers only the inclusion of two parallel RIIC circuits, but higher numbers have been used to describe experimental data. This model is often invoked to account for the presence of surface passivation layers on metal oxide electrodes where current must first pass through the outside layer before reaching the underlying electrode. Such features are commonly encountered in the area of Li-ion batteries. 14,15,30

Model C. Another commonly used equivalent circuit is that of model C where one parallel RIIC circuit is embedded within a second parallel RIIC circuit. This model is one of the most useful at fitting a wide range of EIS features; however, this also means it is one of the most debated in terms of physical relevance to the metal oxide electrode. Derivatives of model C have been used to explain surface layer formation much like model B,<sup>3</sup> the presence of defect states within semiconductor metal oxides,<sup>2,5,31-33</sup> and resistance to charge transfer between metal oxides and conductive substrates, often called contact resistance. The physical relevance of each explanation hinges on the magnitudes of the resistor and capacitor elements. In the limit where  $Q_1 > Q_2$ , model C resembles a Randles circuit (model A) and exhibits a single arc in the Nyquist plot defined by the total resistance  $R_1 + R_2$ . This is the situation often invoked to characterize surface layers and defects states as  $Q_2$  is defined as the capacitance of these layers/states and Q1 is defined as the bulk capacitance of the metal oxide electrode. If  $Q_1$  and  $Q_2$  are similar in magnitude (within 1 order), the shape of the arc can appear warped or misshapen due to overlapping frequency responses from each capacitor. If  $Q_1 \gg Q_2$ , then model C is indistinguishable from model A and the single arc is defined only by  $Q_1$  and  $R_{ct} = R_1 +$ 

 $R_2$ . In the opposite limit of  $Q_1 < Q_2$ , model C resembles model B with two distinct arcs. This limit has been used to describe porous electrodes with a contact resistance  $(R_1)$  between the metal oxide and the conductive substrate. 34-36 The porosity of the electrode is accounted for by assigning Q2 to the metal oxide capacitance and  $Q_1$  to the capacitance of the conductive substrate exposed to the electrolyte due to incomplete coverage by the porous metal oxide. The condition of  $Q_1$  < Q2 has also been used to describe large concentrations of surface defect states in the case of  $Fe_2O_3$  photoanodes used for water oxidation. <sup>2,5,12,31,32,37</sup> Here,  $Q_1$  is the capacitance of the bulk metal oxide, and  $Q_2$  is the capacitance of surface defects.

Figure 4 shows a comparison of simulated data for model C and model B with ideal capacitors to highlight their similarities

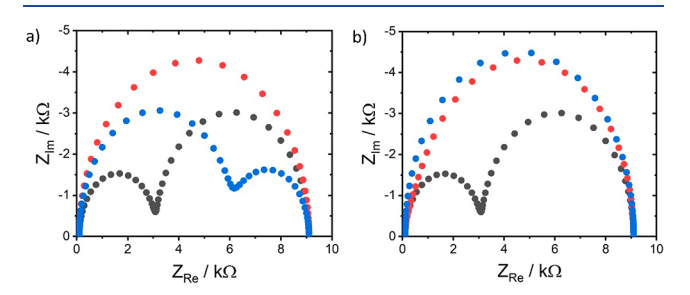


Figure 4. Simulated Nyquist plots comparing equivalent circuits with model B (a) and model C (b). Different colors represent different magnitudes for the capacitor  $C_2$  in each model with  $C_2 = 100 \ \mu F$ (black), 1  $\mu$ F (red), and 0.01  $\mu$ F (blue). In all cases,  $R_s = 0.1 \text{ k}\Omega$ ,  $R_1 =$ 3 k $\Omega$ ,  $C_1 = 1 \mu F$ , and  $R_2 = 6 k\Omega$ .

and differences. In both cases,  $R_1 = 3 \text{ k}\Omega$ ,  $R_2 = 6 \text{ k}\Omega$ , and  $C_1 =$ 1  $\mu$ F while  $C_2$  was varied from 100 to 0.01  $\mu$ F. The two models are identical for the case of  $C_2$  = 100  $\mu F$  ( $C_2 \gg C_1$ ) but are distinct for the other two conditions. When  $C_2 = C_1$ , both models display a single arc with  $R_{ct} = R_1 + R_2$ ; however, the arc for model C is slightly warped. As C2 becomes smaller, model B again shows two semicircles arcs in the Nyquist plot with distinct  $C_1$  and  $C_2$  capacitances. At the same condition, model C displays only a single arc defined by  $C_1$ .

Model D. The diffusion of mobile charges in the electrolyte is often described using the equivalent circuit shown in model D. This circuit is a modification to the Randles circuit where a Warburg diffusion (Z<sub>W</sub>) term has been included in series with the charge transfer resistance. This arrangement is meant to describe the physical reality of diffusion of electroactive species to the surface of the electrode where they undergo oxidation or reduction via charge transfer. Such diffusion limitations form the bedrock of many electrochemical techniques where a diffusion layer builds up over time as the concentrations of electroactive species are depleted at the electrode surface.<sup>22</sup> The diffusion of redox-inert species such as counterions can also be described by model D if the charge transfer event is within the metal oxide electrode and the counterions are necessary to balance charge. This is the case of ion intercalation batteries where the redox event is centered on a transition metal within the metal oxide electrode, but the diffusing ions are necessary for the event to occur.

The equation used to describe Warburg diffusion in model D could be eqs 8 and 9 or eq 11. The most common form is to use the infinite form of Warburg diffusion (eq 11). The more general forms of eqs 8 and 9 are encountered when mobile charges exist within the metal oxide electrode structure. This

may be due to mobile carriers (i.e., electrons or holes) diffusing through conduction and valence bands, as is the case for many semiconductor metal oxides, or due to diffusion of small ions within porous channels, as in the case of Li-ion batteries. In these examples, the finite thickness of the metal oxide electrode defines L at a relatively small value. Choosing between egs 8 and 9 depends on the magnitude of charge transfer resistance with the electrolyte solution. The terms reflecting and absorbing boundaries refer to the ability of the solid/ electrolyte interface to reflect charges back into the metal oxide solid (infinite charge transfer resistance) vs absorbing charges into the electrolyte (zero charge transfer resistance). 28,29

Model E. A special case of thin layer diffusion for mobile carriers within porous metal oxide semiconductors is commonly evaluated using the equivalent circuit shown in model E. This circuit describes the diffusion of mobile carriers by the resistance  $R_d$  in series with a parallel  $R_1||Q_1|$  circuit meant to represent the solid/electrolyte interface. The inclusion of distributed  $r_{\rm d}$  and  $r_{\rm l} \| q_{\rm l}$  elements along a chain indicates the porosity of the electrode where there are multiple interfaces between the metal oxide and electrolyte where Faradaic or non-Faradaic current may pass. The distributed elements are defined with respect to the overall terms as follows:  $r_d = R_d/L$ ,  $r_1 = R_1L$ , and  $q_1 = Q_1/L$ . An important feature of this model which cannot be described graphically is that the diffusion of carriers and charge transfer reactions at the solid/electrolyte interface are linked by assuming a steady-state concentration of mobile carriers. This model is called the diffusion-recombination model and was derived and popularized by Bisquert for the study of mesoporous TiO2 electrodes used in dye-sensitized solar cells.<sup>28</sup> The expression for the total impedance is shown in eq 13. The effect of linking  $R_d$  and  $R_1$ mathematically is to essentially allow for a variable degree of charge transfer through the solid/electrolyte interface, as opposed to completely reflecting  $(R_{ct} = \infty)$  or absorbing  $(R_{ct} =$ 0) conditions. Therefore, the semicircle arc associated with  $R_1$  $C_1$  appears at lower frequency than charge diffusion. The simulated Nyquist plot in Table 2 clearly shows the linear Warburg behavior at high frequency. This is notably different than combining a finite Warburg diffusion term (eqs 8 and 9) in series with a parallel  $R_1 || C_1$  where the linear Warburg behavior would appear at low frequency following the  $R_1 \parallel C_1$ arc at high frequency.

$$Z(\omega) = \left(\frac{R_{\rm d}R_{\rm l}}{1 + R_{\rm l}C_{\rm l}j\omega}\right)^{1/2} \coth\left[\left(\frac{R_{\rm d}}{R_{\rm l}}\right)^{1/2} (1 + R_{\rm l}C_{\rm l}j\omega)^{1/2}\right]$$
(13)

## 3. HETEROJUNCTION SOLAR CELLS

3a. Overview. Nanocrystalline, polycrystalline, and single crystalline metal oxide materials have been of great importance for their utilization in devices for solar-to-electric energy conversion.<sup>38</sup> Specifically, n-type and p-type wide band gap oxides are used as selective contacts for electron and hole transport, respectively, between a light absorber and the external circuit. Oxides that have been utilized in heterojunction devices as charge transport layers include  $TiO_2$ ,  $^{39-41}$  ZnO,  $^{42,43}$  SnO<sub>2</sub>,  $^{44-46}$  Nb<sub>2</sub>O<sub>5</sub>,  $^{47-49}$  SrTiO<sub>3</sub>,  $^{49-51}$  ZnSn<sub>2</sub>O<sub>4</sub>,  $^{52-54}$  CeO<sub>2</sub>,  $^{55,56}$  NiO,  $^{57,58}$  and CuGaO<sub>2</sub>.  $^{59,60}$  This list gives a small taste of the variety found in metal oxides: from

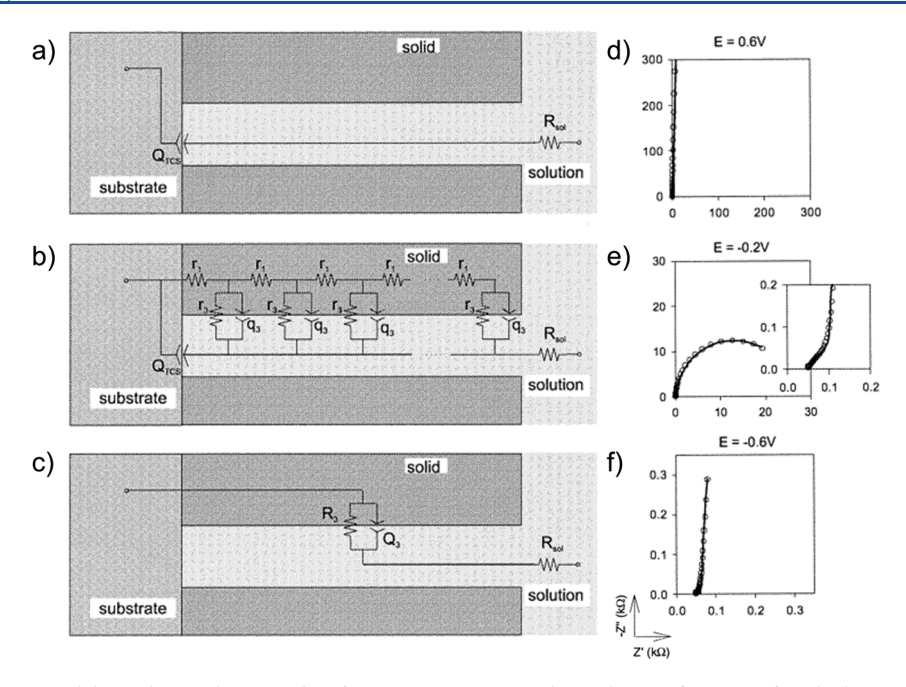


Figure 5. Equivalent circuit models used to analyze EIS data for mesoporous  $TiO_2$  electrodes as a function of applied potential. Going from positive to negative potentials,  $TiO_2$  is modeled as an (a) insulator, (b) semiconductor, and (c) metal. Nyquist plots (d-f) obtained at different applied potentials to show the behavior of each equivalent circuit. Reproduced with permission from ref 36. Copyright 2002 American Chemical Society.

using transition metals to lanthanides, from binary to ternary, and from n-type to p-type.

In some cases, the metal oxide facilitates charge separation from the light absorber at the metal oxide interface such as in dye-sensitized solar cells where a molecular chromophore is bound directly to the metal oxide surface. 7,61 However, for heterojunction solar cells in which the light absorber is a semiconductor material of considerable thickness (e.g., quantum dot solar cells, <sup>8,9</sup> organic photovoltaics, <sup>10,62</sup> and perovskite solar cells <sup>11,23–27</sup>), charge separation of e<sup>-</sup> and h<sup>+</sup> may occur within the semiconductor and the metal oxide serves only as an electrode selective for e or h. In the former case, the EIS data can be readily interpreted in terms of the electronic properties of the metal oxide because an electrolyte with a large Helmholtz capacitance is present at the interface. In the latter case, the significantly lower capacitance of the semiconductor makes interpretation of EIS data more challenging because the measured interfacial capacitance is a series combination of the semiconductor and metal oxide. This is perhaps why EIS studies focusing on metal oxides in the latter devices are not found often in the literature. Notable exceptions include studies on QDSCs which compare SnO<sub>2</sub> and TiO2 where electron diffusion in the metal oxide can be observed  $\tilde{63,64}$  and PSCs where the nature of the metal oxide makes a significant difference in the magnitude of the interfacial capacitance observed at low frequencies. 23-27

EIS is a powerful tool to characterize metal oxide electrodes, either in simple electrochemical cells, or in the context of complete solar cells. While CV on heterogeneous systems is useful, EIS can provide a distinction between specific interfaces such as the metal oxide/electrolyte and metal oxide/substrate interfaces as well as significant information on the band structure, density of states, number and type of charge carrier, and conductivity of the metal oxide electrode. In this section we describe metal oxides used for solar-to-electric energy conversion, the results of their EIS data, and the models that have been used to understand their properties. The under-

standing of heterogeneous electrochemistry using EIS is significant in the literature for TiO2, ZnO, and SnO2 for electron transport (n-type), and NiO and CuGaO<sub>2</sub> for hole transport (p-type). In most cases, a metal oxide/electrolyte interface is specifically studied; however, a discussion of metal oxide/semiconductor interfaces is also included in the section on TiO2 as it relates to recent work in the area of PSCs. The specific resistors and capacitors discussed in this section are related to the resistance to charge diffusion/transport ( $R_d$ ,  $R_t$ , or  $Z_w$ ) through the metal oxide, resistance to charge transfer  $(R_{ct})$  or charge recombination  $(R_{rec})$  at the metal oxide interface, and the chemical capacitance  $(C_{\mu})$  of the metal oxide. Importantly, Cu can also be represented as a density of states (DOS) of the metal oxide, which gives insight into the distribution of defect/trap states at the metal oxide interface. Metal oxide morphology and doping are also shown to influence  $C_u$  due to surface area changes, exposure of surface states, and changes in conductivity/introduction of defects.

**3b.** n-Type Metal Oxides. *TiO*<sub>2</sub>. The most significant use of EIS to study a metal oxide in the context of heterojunction solar cells has been done on TiO<sub>2</sub> because of its use in the original Grätzel cell. Bisquert and co-workers, in particular, have published a significant body of work on mesoporous films of TiO<sub>2</sub> nanocrystals, as they are the most relevant in the context of dye-sensitized solar cells for their high surface area. <sup>19,36,65-67</sup>

Bisquert has shown that, depending on the applied potential to a bare  ${\rm TiO_2}$  electrode in a three-electrode setup, different models can be used to understand the electronic properties of the metal oxide. <sup>36</sup> Specifically, the electrode can behave as an insulator at potentials very positive of the conduction band edge, and as a metal at potentials very negative of the conduction band edge. In these regimes, the equivalent circuits are simplified as shown in Figure 5. The corresponding Nyquist plots next to each circuit demonstrate that the impedance at positive potentials resembled a Randles circuit with an infinitely large  $R_{\rm ct}$  due to the low level of electronic

states in the band gap. As the potentials became more negative and conduction band states began to be populated by electrons, R<sub>ct</sub> decreased, and a semicircle arc was observed at low frequencies. At these conditions, the resistance for electron diffusion through the film could be observed, shown by the linear behavior at high frequencies, and the capacitance associated with conduction band states could be estimated. The transmission line equivalent circuit shown as model E was developed to model EIS data such as this for TiO<sub>2</sub> mesoporous films. As the applied potential was pushed further negative, the diffusional resistance decreased such that the linear feature was no longer observed. The capacitance of the metal oxide also increased such that the full semicircle arc was not fully resolved over the frequency range. These changes were explained by an exponential increase in the density of conduction band states in TiO2. As these states were populated at more negative potentials, the diffusional resistance decreased on the basis of its inverse relationship with conductivity and the capacitance increased as the concentration of charges went up. Overall, this work demonstrated the ability of impedance to differentiate insulator, semiconductor, and metallic behavior in metal oxide films, while considering the unique contributions of the mesoporous structure.

Bisquert and co-workers have also modified the transmission line model from above to include interfaces specific to DSSCs. Features were added that take into account the unique properties of electrolyte diffusion, charge recombination at the metal oxide/electrolyte interface, and the electrolyte/counter electrode interface.<sup>67</sup> Other models have been proposed that are specific to DSSCs in other operating conditions. 68,69 Prior to Bisquert, Kern et al. derived a model that allowed for elucidation of EIS behavior for DSSCs at open circuit conditions under illumination where the modeling of electron diffusion and recombination was done with differential equations, as opposed to RC circuit elements.<sup>70</sup> It was later elucidated by Adachi et al. that, despite the different physical assumptions made by Kern and Bisquert for their models, they are each mathematically the same.7

One aspect of TiO2 that researchers have sought to understand is the presence and distribution of trap/surface states present at potentials below the conduction band edge. The presence of these states influences the measured chemical capacitance and the charge transfer/recombination events that take place at the metal oxide surface. A study by Mora-Sero and Bisquert showed that the Fermi-level of electrons in surface states was distinct from the Fermi-level of free electrons in the conduction band of TiO<sub>2</sub>.<sup>72</sup> Due to recombination of the electrons in the surface state with the electrolyte, the Fermi-level of the surface states is always below that of the bulk Fermi-level. The charge transfer resistance was measured by EIS and plotted vs the Fermi-level energy of the surface states and the bulk. It was revealed that surface state recombination is dominant due to the low concentration of conduction band electrons when the Fermi-level of the surface state is below that of the surface state energy and conduction band energy. As the Fermi-level of the surface state surpasses the energy level of the surface state, and the bulk Fermi-level approaches the conduction band, conduction band recombination becomes the dominant pathway.

Results of EIS investigations of nanoparticle TiO2 mesoporous films in many studies have indicated the presence of such surface/trap states. 73-79 Gimenez et al. studied surface states for a bare TiO<sub>2</sub> electrode in aqueous electrolyte by

modeling the charge transfer resistance and chemical capacitance using the transmission line model (model E). A monoenergetic trapping model was developed in the paper and was validated by simulations and experimental data. EIS data showed an exponential increase in  $C_u$  as the monoenergetic trap state was approached (around -0.85 V vs Ag/AgCl) followed by a decrease at more negative potentials, then an exponential increase at the trap state tail. The opposite trend was observed for  $R_{ct}$  where recombination resistance decreased as the trap states were populated with electrons. Illumination of the electrode resulted in similar behavior for  $C_w$  but  $R_{ct}$  was constant over the applied potential range. This was explained by a saturation of recombination events from photogenerated charges. EIS has also been used to differentiate between monoenergetic trap states and exponential trap states. Bertoluzzi et al. elucidated the contribution of exponential and monoenergetic trap states to the total chemical capacitance by comparing nanoparticle TiO2 with submicron TiO2, which had more defined crystal facets to expose the surface states (Figure 6).<sup>78</sup>

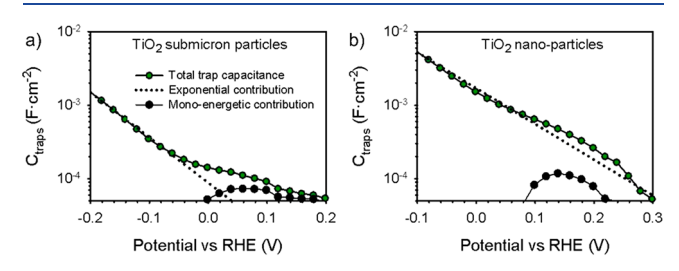


Figure 6. Total capacitance of trap states measured via EIS for (a) submicron TiO<sub>2</sub> and (b) nanoparticle TiO<sub>2</sub>. The contribution of monoenergetic traps was confirmed by the peak feature in the capacitance as a function of potential. The contribution of exponential trap states is shown by the dashed line. Reproduced with permission from ref 78. Copyright 2014 American Chemical Society.

Other studies have shown that passivation of trap/surface states can be achieved by adding blocking layers. 77,80-83 Blocking layers are a standard component of heterojunction solar cells because of their ability to limit charge recombination. Pascoe et al. showed with EIS that atomic layer deposition of Al<sub>2</sub>O<sub>3</sub> improved recombination by increasing  $R_{\rm ct}$  while  $C_{\mu}$  stayed consistent.<sup>77</sup> However, it was also shown that the conduction band states were being suppressed by the blocking layer treatment. Góse et al. used EIS to understand the improvements and limitations of blocking layers in DSSCs.8

The desire to change the charge transport properties and surface area of TiO2 electrodes has led to an exploration of different nanocrystalline morphologies. There are two notable aspects to the areas which have been investigated. The first is exploration of different crystal phases of TiO2, such as anatase, rutile, and brookite, to understand the relationship between crystal structure and charge transport. The most studied of these phases is anatase TiO2 because of its larger band gap and higher conductivity,<sup>84</sup> but interest in rutile and brookite has been reported in the literature.<sup>84–93</sup> EIS has been used to understand the fundamental charge transport properties of rutile and anatase crystal phases directly, 94,95 as well as in solar cells. 96-99 Growth of the rutile phase thermodynamically favors nanorods and can be seen in a study by Kim et al. to function well as a scaffold for perovskite nanocrystals in solid-

state PSCs. 98 Using EIS the authors determined the effect of rutile nanorod length on device performance. Under both an applied potential and illumination, it was determined that the impedance fitting could be simplified from the transmission line model (model E) to a simple two-arc model (model B), because the midfrequency Nyquist arc did not have a linear feature indicating diffusion limited charge transport, believed to be due to the large applied potential. The midfrequency arc was the result of the recombination resistance and the chemical capacitance. The authors showed that nanorod length had little effect on the chemical capacitance or recombination resistance in these devices, as neither of these parameters were changing significantly with applied potential, which was consistent with previously reported rutile PSC measurements. However, the photocurrent and photovoltage decreased in devices with increasing nanorod length.

Brookite solar cells have typically shown lower efficiencies than anatase  ${\rm TiO_2}$  but have had large open circuit potential  $(V_{\rm oc})^{.92,93,96,97,100}$  Pourjafari et al. used EIS to study anatase TiO<sub>2</sub> and brookite samples synthesized under acidic and basic conditions to compare how morphology and surface structure affected electron injection into TiO<sub>2</sub>. 66 EIS was measured at the open circuit potential under illumination, and Nyquist plots were fit to the transmission line model (model E). Synthesis and nanoparticle treatment both showed an effect on the measured chemical capacitance, recombination resistance, and electron lifetime in the  $TiO_2$  electrodes.  $C_u$  showed exponential dependence on  $V_{\rm oc}$  for each sample, consistent with surface states, but base-synthesized brookite  $C_u$  was considerably lower than anatase TiO<sub>2</sub>. R<sub>rec</sub> for brookite DSSCs was lower than anatase, but acid treatment increased  $R_{rec}$  in brookite DSSCs. Base-treated brookite also had the shortest electron lifetime, consistent with a small  $R_{rec}$ .

Kusamawait et al. had previously done a similar study on brookite  $TiO_2$  photoelectrodes and showed high  $V_{oc}$  for brookite devices. 97 They also showed a higher recombination resistance and slower charge transport. The same EIS model was used in both studies (model E). Hsiao et al. also explored the effect of brookite and rutile defects in anatase TiO2 with EIS in a DSSC. 99 The authors emphasize that the presence of trap states in TiO2 has been tied to crystal defects, and intentionally adding those defects helps study the influence of trap states on charge transport. Measured EIS of pure and defect-rich anatase reveals an increased  $C_{\mu}$  for defect-rich anatase, which is consistent with the surface traps acting as electron sinks.

The second aspect of morphological studies of TiO2 using EIS has focused on changing the shape of the nanocrystal. 101,102 With exploration of different particle shapes, control over electron transport and surface area can be shapes.<sup>79,123</sup> Several of these morphologies have been studied in conjunction with synthetic, photochemical, and electrochemical doping. The most popular structure, besides nanoparticles, in the literature is the nanowire/nanotube/ nanorod structure. To briefly differentiate these structures, nanorods are solid particles oriented specifically on the substrate, nanotubes are also oriented specifically but are hollow, and nanowires are solid but do not have a specific orientation. Their popularity is due to the idea that electron flow in a metal oxide could potentially be directed vectorially

toward the conductive substrate for improved charge transport and extraction from the solar cell. 114 For this reason, onedimensional  ${\rm TiO_2}$  nanostructures have been investigated in solar cell devices.  $^{102,111,117,118}$  Wu et al. used EIS to measure and deconvolute all aspects of a nanotube DSSC, including resistances associated with diffusion, electron, and charge transfer, as well as capacitances associated with the doublelayer, contact, and chemical capacitances in the device. 118

One of the first studies of TiO2 nanotubes by Fabregat-Santiago et al. used EIS to compare the charge transport properties and chemical capacitance to those of TiO2 nanoparticles. 112 Whereas TiO<sub>2</sub> nanoparticles typically show low charge carrier densities with a Fermi-level that is well below the conduction band edge, different morphologies of TiO<sub>2</sub> can display more metallic behavior (i.e., high carrier density). To explore if this phenomenon is observed in TiO<sub>2</sub>, nanotubes were synthesized with widths of 20 nm, reflective of the size of TiO2 nanoparticles synthesized for films, but had variable lengths from 200 to 1000 nm. The Nyquist plots display a single arc at low frequency with a high-frequency linear feature, indicative of electron diffusion through the TiO<sub>2</sub> nanotube. The widths of these TiO2 nanotubes did not show a depletion capacitance consistent with band bending, which is the same behavior observed in nanoparticles.

Furthermore, it was demonstrated in the study by Fabregat-Santiago et al. that the nanotubes were susceptible to electrochemical doping, when exposed to an extremely negative potential for an extended time in basic media. This caused a significant change in the chemical capacitance and transport resistance. Figure 7 shows that, in the "fresh"

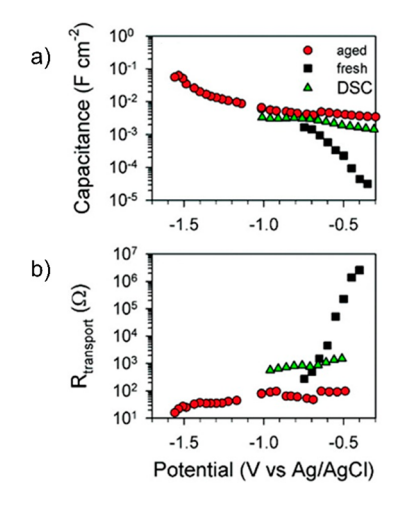


Figure 7. Potential dependence of (a) capacitance and (b) transport resistance for TiO2 nanotubes measured by EIS as a function of applied potential. The "aged" nanotube electrode showed a large, uniform  $C_u$  and low  $R_t$  indicating that  $H^+$  intercalation into the  $TiO_2$ electrode had occurred. Reproduced with permission from ref 112. Copyright 2008 American Chemical Society.

nanotubes, the transport resistance measured by EIS exhibited an exponential dependence on applied potential, indicative of a low number of charge carriers when the applied potential is far from the conduction band edge. A similar trend was observed for the chemical capacitance, consistent with an increase in electronic states as the conduction band edge was approached (Figure 7). TiO<sub>2</sub> nanotubes that were "aged" by long exposure to an applied negative potential showed a significant decrease

I

in transport resistance and increase in capacitance that varied less with applied potential. This indicated an increase in charge carriers in the nanotubes resulting in Fermi-level pinning near the conduction band edge. The increased carrier concentration was attributed to reduction of Ti4+ sites coupled to intercalation of H+ into the TiO2 lattice. It was also demonstrated that the capacitance measured was variable with the length of the TiO<sub>2</sub> nanotube, indicating the role of surface area in proton intercalation. Comparative studies of nanotubes in acidic media showed  $R_{\rm t}$  and  $C_{\mu}$  values similar to "aged" samples in basic solution. Thus, a high concentration of protons immediately induced the reduction of TiO2 and increased carrier density. Interestingly, studies of TiO2 nanoparticles in acidic media did not demonstrate this intercalation behavior, which demonstrated that nanotube morphology was an important factor for proton intercalation.

Doping is a very common way to control defects and electronic properties of metal oxide electrodes. <sup>124</sup> EIS studies on TiO<sub>2</sub> electrodes have revealed a wide range of changes in charge transport resistance and chemical capacitance based on the chemical nature of the dopant and the method with which the dopant is introduced (e.g., photoinduced <sup>115,116</sup> or electrochemically <sup>112</sup> induced). Niobium, tantalum, cerium, and tin have each been doped into TiO<sub>2</sub> and the resulting effects studied with EIS. <sup>125–128</sup> Collectively, these studies point to the same result where increased concentration of dopant atoms led to decreased charge transport resistances due to the higher concentration of free carriers in the TiO<sub>2</sub> conduction band.

Discussion up to this point has focused on TiO<sub>2</sub>/electrolyte interfaces where the interfacial capacitance is directly related to the chemical capacitance of the TiO2 electrode. However, when these electrodes are used as electron transport layers in lead halide perovskite solar cells, the capacitance at the metal oxide/semiconductor interface is more closely related to that of the perovskite material due to the formation of a depletion layer.<sup>23-27</sup> Nonetheless, the nature of the metal oxide in contact with the perovskite has been shown to influence the presence of an ionic capacitance at the metal oxide/perovskite interface. 129,130 This "extra" capacitance is due to mobile ions within the perovskite such as iodide and methylammonium which accumulate at the interface. This ionic capacitance is also problematic in PSCs as it leads to a hysteresis in photoinduced current-voltage measurements which are used to determine solar-to-electrical conversion efficiency, leading to uncertainty in these measurements.<sup>25</sup> Kim et al. has provided direct evidence for this assignment by examining the capacitance vs frequency data collected by EIS for PSCs with a TiO<sub>2</sub> electron transport layer in the "normal" configuration (electrons directed toward the transparent conductive oxide (TCO)) and with an organic electron transport layer in the "inverted" configuration (electrons directed away from the TCO).  $^{130}$  Figure 8 shows that the  ${\rm TiO_2/perovskite}$  interface results in significant capacitance in the low-frequency region due to the accumulation of ions at the interface. The use of the organic electron transport layer removes much of this capacitance and yields a more reproducible current voltage curve. Studies have shown the use of SnO<sub>2</sub> as an n-type selective contact and/or NiO as a p-type selective contact can also decrease this low-frequency ionic capacitance, although the physical origin of the metal oxide dependence is not yet fully understood. 129,130

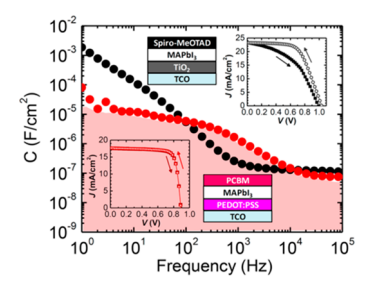


**Figure 8.** Capacitance vs frequency measured for PSCs with (black) and without (red) a  $TiO_2$  electron transport layer. The inclusion of the  $TiO_2$  layer results in ionic capacitance at low frequencies which results in hysteresis in the illuminated J-V curve (inset). The use of an organic electron transport layer, PCBM, does not show this ionic capacitance, and therefore, there is no hysteresis in the J-V curve. Reprinted with permission from ref 130. Copyright 2015 American Chemical Society.

Figure 8 also highlights an important aspect of understanding capacitance at metal oxide interfaces. The frequency dependence shows that the ionic capacitance occurs in the low-frequency region while the bulk capacitance of the perovskite occurs at high frequency. Therefore, in order to obtain meaningful information about the depletion layer capacitance of the perovskite, a high frequency can be used to isolate this feature from the ionic capacitance. Almora et al. have highlighted this technique in distinguishing true depletion layer capacitance using Mott–Schottky analysis from erroneous assignments due to the influence of the ionic term. <sup>27</sup>

ZnO. Zinc oxide was one of the first metal oxides employed in heterojunction solar cells,  $^{131,132}$  but these never surpassed the efficiencies of  $TiO_2$  solar cells. In comparison studies of  $TiO_2$  and ZnO solar cells, the  $TiO_2$  devices typically have better performance.  $^{133-135}$  Interest in ZnO has been maintained because of the ease with which different morphologies of ZnO can be synthesized.  $^{136,137}$  While different morphologies have been explored in  $TiO_2$ , the crystal structure of ZnO gives rise to synthetic simplicity and a large level of variability to explore many unique structures. EIS has been used to study ZnO nanoparticles, but nanorods/nanotubes are the main ZnO structures studied with EIS, for the same reasons stated above for  $TiO_2$ .

Before different ZnO morphologies are discussed, it is useful to compare ZnO systems that are similar to TiO<sub>2</sub> to understand if they can, electrochemically, be treated the same. A study by Guillén et al. addressed the issue of transport resistance measurement in ZnO nanoparticulate DSSCs that did not show the diffusion feature in their Nyquist data. By combining time constants measured with IMPS and capacitance values measured from EIS, the authors used the relationship  $\tau_{\rm rt}\gamma=R_{\rm t}C_{\mu}$ , where  $\gamma$  is an illumination factor, to calculate  $R_{\rm t}$ . EIS measurements were performed at short-circuit conditions, so as to be comparable to the IMPS data, and these were then converted to  $R_{\rm t}$  from the given relationship. To check their method, the  $R_{\rm t}$  values obtained from EIS + IMPS were compared to data collected using EIS only, and the values are comparable until high-Fermi-level conditions are reached, as expected.

An early EIS study on a ZnO nanowire array demonstrated that EIS could characterize the film by mathematically modeling the nanowire. First, via Mott–Schottky measurements, Mora-Sero et al. demonstrated that by appropriately defining the particle geometry of the ZnO nanowires, band

bending was demonstrated at their surface (Figure 9). This has not been observed in anatase TiO<sub>2</sub> nanoparticles or nanotubes.

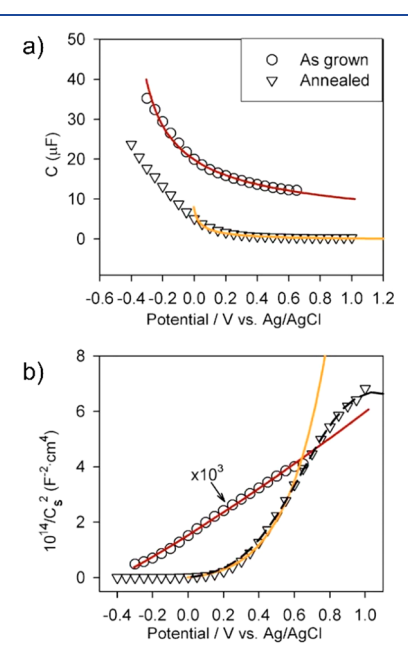


**Figure 9.** (a) Capacitance measured by EIS for a ZnO nanowire array before and after annealing at 450 °C in air. (b) Mott–Schottky representation of capacitance showing linear behavior for the as grown ZnO nanowire electrode. Reproduced with permission from ref 139. Copyright 2006 AIP Publishing.

The Mott-Schottky equation predicts a linear trend between  $C^{-2}$  and the applied potential  $(E_{app})$  when band bending at the semiconductor/solution interface is present, eq 14. Here,  $\varepsilon$  is the relative dielectric constant of the semiconductor,  $\varepsilon_{\rm o}$  is vacuum permittivity, A is surface area of the interface, e is the fundamental charge, N is the doping density,  $k_{\rm B}$  is Boltzmann's constant, and T is temperature. If a linear trend is observed, then the measured capacitance is that of the depletion layer formed at the metal oxide interface, and the flat band  $(E_{fb})$  and doping density of the semiconductor may be determined. The small linear slope observed in the Mott-Schottky data indicated a high density of charges (N) in the nanowires, behavior that was attributed to the synthetic method. A decrease in charge density and capacitance was observed when nanowires were annealed under air at 450 °C, which indicated a remediation of defects that resulted in surface states. The change in capacitance with annealing was also seen in a study by Tena-Zaera et al. where ZnO nanowires were synthesized via electrodeposition and the same EIS model (model A) was used.140

$$C^{-2} = (2/\varepsilon \varepsilon_{o} A^{2} e N)(E_{app} - E_{fb} - k_{B} T/e)$$
(14)

Characterization of ZnO nanorod DSSCs using EIS has also been reported. Martinson et al. used the transmission line model (model E) to measure the chemical capacitance and charge transfer resistance, as well as charge lifetimes and charge extraction time. Briefly, charge lifetime is defined as the amount of time the photogenerated charge survives before recombination with the electrolyte and is calculated from the relationship  $\tau_n = R_{\rm rec}C_\mu$ . Charge extraction time is the amount of time it takes for the photogenerated charge to be collected in the external circuit and is calculated from the relationship  $\tau_{\rm d}$ 

=  $R_{\rm t}C_{\mu}$ . EIS of the film was measured in the dark, with a bias such that the charge transport resistance feature is visible in the Nyquist plot. Conductivity is elucidated from the charge transport resistance and shows significantly lower conductivity compared to that of nanoparticle  ${\rm TiO}_2$ . The ZnO nanorod film also shows lower capacitance and charge transfer resistance (Figure 10). However, the charge extraction time for the ZnO

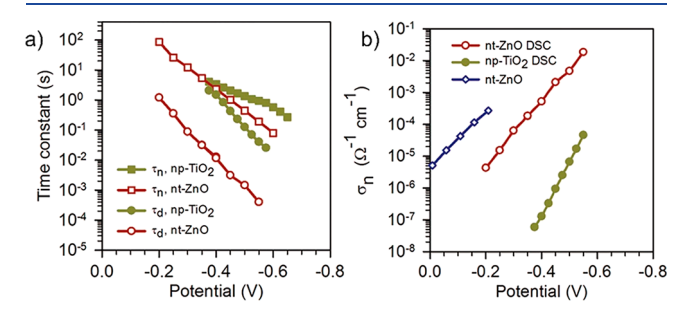


Figure 10. (a) Electron recombination lifetimes  $(\tau_n)$  and extraction lifetimes  $(\tau_d)$  calculated from resistance and capacitance values measured by EIS for DSSCs assembled from a nanoparticle  $TiO_2$  electrode and a nanotube ZnO electrode. (b) Conductivity of a nanoparticle  $TiO_2$  DSSC, a nanotube ZnO DSSC, and the bare ZnO nanotube array electrode as a function of applied potential. Reproduced with permission from ref 141. Copyright 2009 American Chemical Society.

nanotube DSSC is 2 orders of magnitude shorter than for nanoparticle TiO2, displaying the influence of morphology on charge transport. EIS of a ZnO nanorod DSSC has also been studied under illumination and elucidates the contribution of trap states to the device performance. 142 Fit to model E, the chemical capacitance under illumination showed exponential dependence at low bias potentials, consistent with a tail of surface trap states. At high bias potentials, the capacitance shows no dependence on illumination, which the authors attribute to a depletion layer capacitance related to the geometry of the electrode. R<sub>ct</sub> also loses its linearity upon the bias potential reaching the onset of a trap state tail, indicating a contribution of the surface states to recombination. R, remained consistent, regardless of whether the EIS was measured in the dark or under illumination. The authors state this is consistent with electron transport occurring within the nanorod core.

EIS has been used to compare the size and morphological aspects with regard to the electronic behavior of other ZnO structures. <sup>143–154</sup> To briefly highlight some unusual structures, ZnO aggregates made from sintered nanowires showed a relationship between sintering temperature and charge transport resistance, elucidated from EIS. 153 Parthasarathay et al. used EIS to show surface-state-mediated electron transfer in ZnO multipods.<sup>144</sup> Hosni et al. investigated the electrochemical properties of ZnO electron transport layers when made of nanospheres or nanorods. 154 Three different nanosphere sizes and one size of nanorod were studied with EIS. The smallest ZnO nanospheres had the highest capacitance and the largest density of trap states. The other nanospheres and the nanorods had a similar  $C_{\mu}$  and trap state density. The capacitance measurements correlated with the measured  $R_{ct}$ , as the smallest nanospheres had the lowest charge transfer resistance, consistent with having the highest trap state density. The other nanoparticle morphologies had very similar  $R_{ct}$ values.

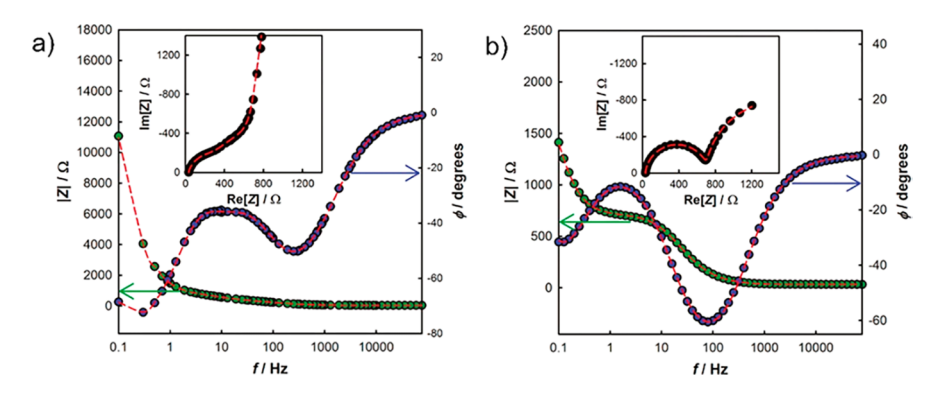


Figure 11. Nyquist and Bode plots for (a)  $TiO_2$  and (b)  $SnO_2$  QDSCs measured at their respective  $V_{oc}$  and 1 sun illumination.  $SnO_2$  does not display the Warburg diffusion feature seen in the midfrequency range for  $TiO_2$  indicating rapid transport of electrons in the  $SnO_2$  electrode. Reproduced with permission from ref 64. Copyright 2011 American Chemical Society.

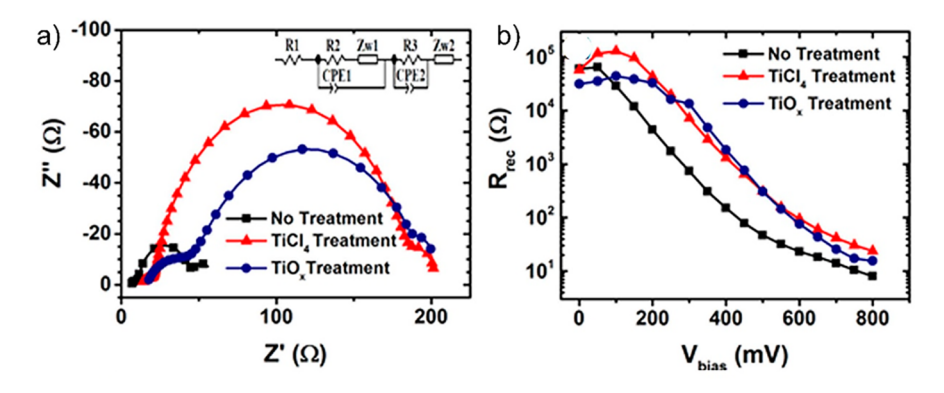


Figure 12. (a) Nyquist plots obtained at the open circuit condition for DSSCs assembled with  $SnO_2$  electrodes which were untreated, treated with  $TiCl_4$ , and treated with  $TiO_x$  to determine the impact of blocking layers on  $R_{rec}$ . The equivalent circuit used to fit the data is shown as an inset. (b) An increase in the midfrequency arc was consistent with an increase in  $R_{rec}$  following  $TiCl_4$  and  $TiO_x$  treatment. Reproduced with permission from ref 63. Copyright 2016 Springer Nature.

Like  $TiO_2$ , the effects of defects and doping have been studied in ZnO using EIS. <sup>155–163</sup> The contribution of native defects in ZnO on its electrochemical performance was assessed by Das et al., where they showed remediation of defects after postsynthetic annealing. 161 Cations doped into ZnO vary from alkali and alkaline earth metals to transition metals. Co-doped ZnO has been studied using EIS to assess the change in the dielectric of the material 158 and has also been shown to change the morphology of ZnO depending on doping level, which lowered recombination resistance and increased the charge lifetime. 164 EIS was used to explore the effect of tin doping on ZnO particle grain boundaries and the resulting electronic properties. Li is one of the most wellstudied metal oxide dopants. In a study by Cheng et al., ZnO doped at 5% and 20% was used as an electron transport layer in an inverted OPV. 162 Data was fit with model C, and 5% Li-ZnO showed the largest recombination resistance and an electron lifetime that was over 2 times longer than that for 20% Li-ZnO. Li-doped ZnO has also been used as an electron transport layer in perovskite solar cells. 163 The authors acknowledge that Li<sup>+</sup> is more likely to interstitially dope in the ZnO structure as opposed to substituting into Zn sites in the structure. Mott-Schottky measurements show a positive shift in the conduction band edge compared to the undoped device. Nyquist plots fit with model B showed that recombination resistance is higher and charge transport resistance is lower for the doped solar cell.

*SnO*<sub>2</sub>. Along with TiO<sub>2</sub> and ZnO, SnO<sub>2</sub> is a heavily investigated metal oxide for heterojunction solar cells. However, its device efficiencies are consistently lower than those measured for devices utilizing TiO<sub>2</sub>. <sup>165</sup> Relative to TiO<sub>2</sub>, it has been shown that SnO<sub>2</sub> has faster electron transport, which is good for charge transport to the external circuit, but it suffers from fast recombination with the oxidized chromophores and redox mediators. <sup>166</sup> EIS has been used to explore these challenges to further improve devices using SnO<sub>2</sub>.

Hossain et al. studied QDSCs with SnO2 and compared them directly to the same device architecture using TiO2.60 Figure 11 shows a comparison of Bode and Nyquist plots for these devices. An important feature of these data was the lack of Warburg diffusion in the SnO<sub>2</sub> electrodes, as seen by the inset Nyquist plots where a linear increase in impedance is observed in the midfrequency range for TiO2, and no such feature is observed for SnO<sub>2</sub>. Analysis of the TiO<sub>2</sub> data required a transmission line model (model E) whereas SnO2 data was analyzed using a series of two parallel RIIC elements (model B). This behavior is consistent with other literature on SnO<sub>2</sub> where rapid charge transport properties have been observed; thus,  $R_d$  is small and not a major factor in the EIS data. 167,168 The chemical capacitance and charge transfer resistance were also shown to be higher for SnO<sub>2</sub> than TiO<sub>2</sub> over the same potential range. Efforts to visualize  $R_t$  for SnO<sub>2</sub> were unsuccessful, but the authors used the transport time of the device cathode to make a rough estimate of the diffusion length of the device. In a similar study of QDSCs with SnO2,

EIS was used to determine the contribution of the nanoparticle film structure to recombination and capacitance by changing the porosity of the electrode. As expected, the more porous structure had a higher capacitance and a lower recombination resistance, explained by increased recombination via surface trap sites.

As with every metal oxide discussed thus far, the role of surface states has also been investigated for SnO2. Huang et al. investigated the effect of surface states on the function of QDSCs employing SnO<sub>2</sub> and compared with TiO<sub>2</sub>. <sup>170</sup> As with the study discussed above, Warburg diffusion was found to be present for TiO<sub>2</sub> whereas it was absent in the case of SnO<sub>2</sub>. Treatment of SnO<sub>2</sub> with TiCl<sub>4</sub> was shown to decrease the contribution of surface states to the  $C_u$  of the electrode, which in turn led to an increase in  $R_{\rm rec}$ . This was attributed to formation of a passivation layer, thus blocking surface states from participating in recombination reactions. EIS has also been used to explore blocking layer treatment of SnO2 in DSSCs with similar results. 63 SnO<sub>2</sub> electrodes were treated with either TiO<sub>x</sub> or TiCl<sub>4</sub> and the EIS data compared with an untreated electrode. All treated solar cells showed a larger midfrequency arc in the Nyquist plots than the untreated cell (Figure 12), indicative of increased recombination resistance at the SnO<sub>2</sub>/chromophore/electrolyte interface. The smaller arc at low frequency was assigned to the cathode/electrolyte interface. When  $R_{rec}$  is plotted over the entire applied potential range, it was shown that the treatment increased  $R_{\rm rec}$ universally for both treatment methods.

Morphological changes of  $\rm SnO_2$  electrodes have been investigated in similar ways to  $\rm TiO_2$  and  $\rm ZnO$ . Along with one-dimensional nanostructures (e.g., nanorods), hierarchical structures (e.g., nanoflowers) and nanofibers have been investigated in  $\rm SnO_2$ -containing solar cells using EIS.  $^{171-175}$  Elumalai et al. and Kumar et al. investigated the charge transport properties of  $\rm SnO_2$  nanoflowers and nanofibers in DSSCs.  $^{171,172}$  In both studies,  $R_{\rm rec}$  was larger for the nanoflowers compared to the nanofiber DSSCs. Interestingly, a higher capacitance was also seen for the nanoflowers, which usually leads to a lower  $R_{\rm rec}$ . This indicates a larger surface area for the nanoflowers but a lower contribution of trap states to the recombination process.

Regardless of the inherent high conductivity of SnO<sub>2</sub>, doping has still shown interesting effects on its electrochemical properties. 176-181 A study by Dou et al. studied SnO<sub>2</sub> nanoflowers doped with Zn in DSSCs. 176 They also studied the effect of a blocking layer on their devices, and all of their data was compared to TiO2 nanoparticles. The chemical capacitance is lower for Zn-SnO<sub>2</sub> compared to TiO<sub>2</sub>, but upon TiCl<sub>4</sub> treatment the Zn-SnO<sub>2</sub> nanoflowers and TiO<sub>2</sub> have a similar capacitance, due to the increase in surface states from the treatment. Charge recombination is also increased upon TiCl<sub>4</sub> treatment for the SnO<sub>2</sub> films and surpasses the recombination resistance for TiO<sub>2</sub>. Bisquert has pointed out that charge recombination can be affected by variations in the conduction band at different carrier concentrations, 182 so to compensate the authors also plotted  $R_{rec}$  vs  $C_u$ , which has been shown to allow for comparison of  $R_{rec}$  at the same density of states. The plot revealed significant inhibition of recombination events upon TiCl<sub>4</sub> treatment in the Zn-SnO<sub>2</sub> nanoflowers. An increase in electron lifetime was also observed in the treated nanoflowers. It should also be noted that charge transport resistance was very similar in each film, which

revealed that doping had a larger impact on transport than morphology.

**3c.** p-Type Metal Oxides. Metal oxides discussed up to this point behave as n-type semiconductors; however, in order to expand the range of heterojunction solar cell devices, p-type metal oxides have also been explored. The challenge of p-type oxides is the movement of charge (i.e., holes) through the valence band, which consists mainly of oxygen p-orbitals that are not highly delocalized, resulting in a large effective mass for holes. Therefore, the best p-type metal oxides consist of metals that have 3d-orbitals that can energetically overlap with the oxygen 2p-orbitals, helping with delocalization and charge transport.

NiO. Nickel oxide is the most heavily explored p-type metal oxide used as a hole transport material in heterojunction solar cells.<sup>57</sup> A great deal of electrochemical properties of NiO have been elucidated from EIS, including charge transport, interfacial recombination, and density of states. Huang et al. measured the impedance of a NiO based DSSC and compared those results to those of a TiO2 electrode to demonstrate the differences between p-type and n-type devices. 185 Nyquist data for the p-type device showed only two semicircles arcs, assigned to the NiO/electrolyte interface at low frequency and counter electrode/electrolyte interface, with no signs of Warburg diffusion. This was attributed to the low thickness of the NiO electrode. Comparing the two solar cells at the same potential showed a smaller recombination resistance for NiO than TiO2. This result indicated that recombination events are more significant at the NiO/ electrolyte interface.

In order to study the charge transport through the NiO electrode, Huang et al. did a follow-up study with a thicker NiO nanocrystalline film. The net result was that a Warburg diffusion feature could now reasonably be observed in the midfrequency range, although it was somewhat masked by the semicircle arc assigned to the counter electrode/electrolyte interface at high frequency (Figure 13). 189 This required fitting of their data using the transmission line model (model E). When EIS was measured under illumination of the solar cell,  $R_t$ and  $C_u$  showed a mild exponential dependence on the measured open circuit potential. The authors tied this behavior to a hopping mechanism for the charge transport, where the holes are localized between Ni<sup>2+</sup> and Ni<sup>3+</sup> atoms. Consistent with their previous study, the authors also showed that illumination greatly affected  $R_{\rm rec}$ , decreasing with higher light intensity and higher open circuit potential. Figure 13b shows a comparison of these data with data collected from intensity modulated photocurrent spectroscopy (IMPS) and intensity modulated photovoltage spectroscopy (IMVS) to show similar lifetimes for hole recombination ( $\tau_h = R_{rec}C_u$ ) and hole transport  $(\tau_{tr} = R_t C_u)$ .

There have been quite a few studies done on NiO doping, but only a few have used EIS to study the results. 194–197 One in-depth study of a Li-doped NiO electrode using EIS was performed by D'Amario et al. 196 Their exploration was inspired by the fast charge recombination lifetimes measured in previous studies, which indicated a high conductivity for NiO and/or a high density of surface states that contribute to this recombination. The goal of this study was to shift the position of the valence band edge using Li<sup>+</sup> doping, thereby achieving a higher open circuit potential for the p-type solar cell. EIS results indicated a strong dependence of charge diffusion and chemical capacitance on the percent Li<sup>+</sup>

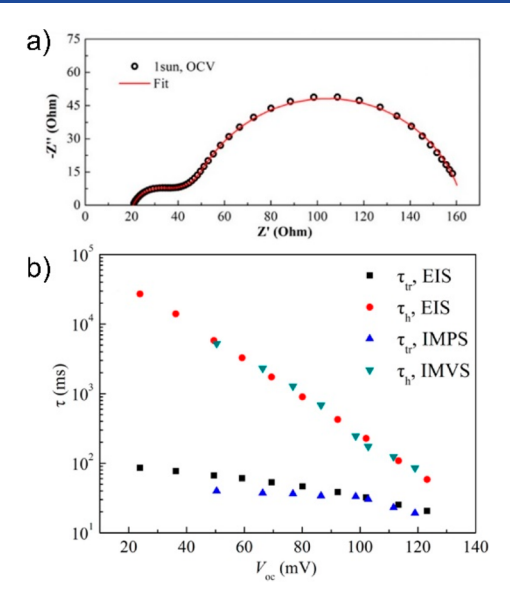
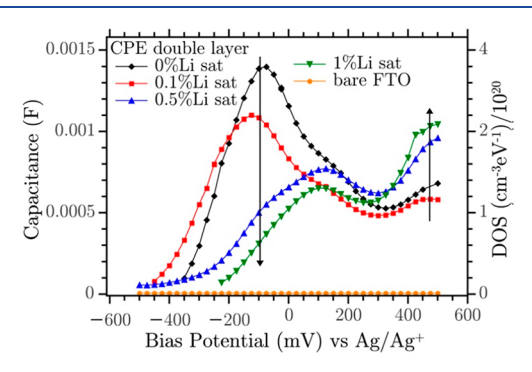


Figure 13. (a) Nyquist plot of a p-type NiO DSSC measured at open circuit potential under 1 sun illumination. (b) Hole lifetimes  $(\tau_h)$  and hole extraction times  $(\tau_{tr})$  calculated from resistance and capacitance data measured from EIS compared to lifetimes measured from IMPS and IMVS. Reproduced with permission from ref 189. Copyright 2012 American Chemical Society.

concentration present during synthesis of NiO nanoparticles. In terms of capacitance, NiO synthesized with 0% Li<sup>+</sup> displayed a prominent peak at potentials near the valence band edge assigned to defect states in the NiO lattice. However, when NiO was synthesized with 1% Li<sup>+</sup>, this peak was dramatically smaller, and the overall capacitance was shifted to more positive potentials (Figure 14). The authors



Double layer capacitance vs V

**Figure 14.** Capacitance and density of states (DOS) of NiO electrodes measured by EIS over a range of applied potentials. The effect of Li-doping NiO is readily seen by the decrease in defect states near -100 mV vs Ag/Ag $^+$ . Reproduced with permission from ref 196. Copyright 2014 American Chemical Society.

proposed that the inclusion of Li<sup>+</sup> results in passivation of defect states, and thus, a lower contribution to the overall chemical capacitance is observed. p-type DSSC measurements supported these results by showing an increase in the open circuit potential from 60 mV (0% Li<sup>+</sup>) to 115 mV (1% Li<sup>+</sup>).

CuGaO<sub>2</sub>. Delafossite copper metal oxides (Cu<sup>I</sup>M<sup>III</sup>O<sub>2</sub>) have also been investigated as hole transport layers in p-type heterojunction solar cells due to their wide band gaps and large hole mobilities. <sup>198,199</sup> The first EIS study on CuGaO<sub>2</sub>

nanoparticles was used to show that these mesoporous electrodes could behave in a semiconductor or metallic manner. Data was analyzed using a modified transmission line model (model E) with the addition of a contact resistance between the  $CuGaO_2$  electrode and the conductive substrate. This feature was important due to the plate-like morphology of the nanoparticles. The nanoparticles showed low conductivities  $(\sigma)$ , calculated from charge transport resistance, that increased moderately as the applied potential was stepped positive toward the valence band edge (Figure 15).  $CuGaO_2$ 

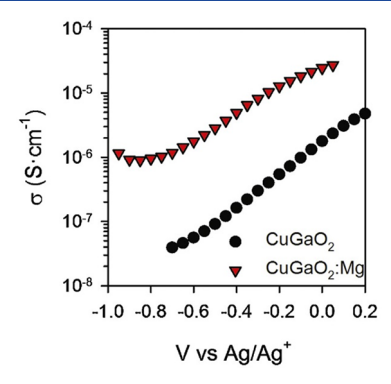


**Figure 15.** Conductivity ( $\sigma$ ) of undoped and Mg-doped CuGaO<sub>2</sub> electrodes plotted vs applied potential showing the increase in conductivity with doping. Conductivity was calculated from the equation  $\sigma = L(R_tA(1-p))^{-1}$ , where L is the film thickness, A is geometric area of the film, and p is porosity (assumed to be 50% for a mesoporous film). Reproduced with permission from ref 35. Copyright 2013 Elsevier.

nanoparticles were then doped with  ${\rm Mg}^{2+}$ , which resulted in an order of magnitude increase in conductivity. Mott—Schottky analysis of the measured chemical capacitance allowed for the hole carrier density of the Mg-doped  ${\rm CuGaO}_2$  to be measured at  $10^{19}~{\rm cm}^{-3}$  compared with  $10^{17}~{\rm cm}^{-3}$  for undoped nanoparticles.

Another study by Bredar et al. also showed EIS of CuGaO2 nanoparticles which displayed high conductivities without the need for dopant atoms. 34 Figure 16 shows Bode and Nyquist plots for CuGaO2 mesoporous electrodes where solid lines represent fits to the same modified transmission line circuit described above. Hole diffusion can be clearly observed in the -0.8 V trace by the linear feature in the midfrequency range. As the potential is stepped to 0.8 V, this feature is diminished as  $R_d$  decreased. The overall change in  $R_d$  (and  $\sigma$ ) over the applied potential range was small in comparison to the undoped CuGaO<sub>2</sub> example above and more in line with the Mg-doped example. These changes were also found to be independent of annealing conditions, thus ruling out interstitial oxygens as the source of charge carriers. Through elemental analysis and XPS measurements, the source of doping was determined to be copper vacancies in the crystal lattice. Elemental analysis revealed a 4% deficiency in Cu atoms, which equated to an acceptor density of 10<sup>21</sup> cm<sup>-3</sup>. A notable difference in the two EIS studies was the synthetic conditions for preparation of the CuGaO2 electrode, suggesting that electrochemical properties of these metal oxides are highly sensitive to their growth environment.

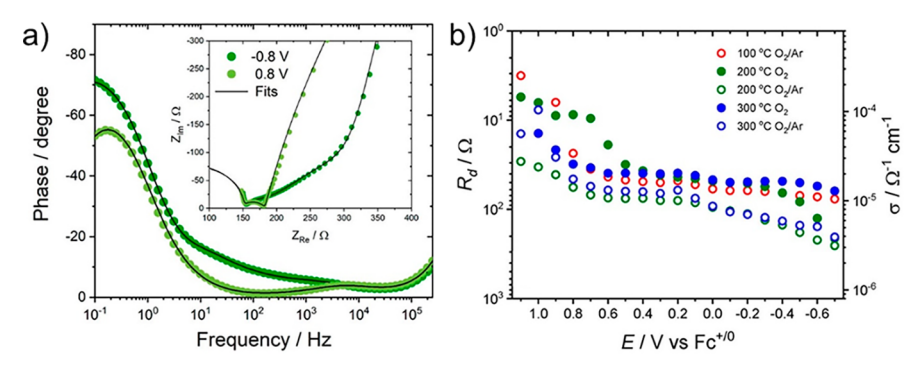


Figure 16. (a) Bode-phase and Nyquist (inset) plots shown for a  $CuGaO_2$  mesoporous electrode highlighting the decrease in the linear diffusion feature observed at -0.8 V as potential is stepped to 0.8 V. (b) Hole diffusion resistance and conductivity plotted vs applied potential (referenced to ferrocene,  $Fc^{+/0}$ ) showing that annealing conditions of the electrode have little effect on  $R_d$ . Reproduced with permission from ref 34. Copyright 2019 American Chemical Society.

#### 4. ION BATTERIES

4a. Overview. A variety of metal oxides have been studied as cathodes and anodes in rechargeable ion batteries used for electrochemical energy storage. 3,14,15,30,200-245 EIS can be a useful technique for researching these materials by providing insight into the corrosion rate of the metal oxide electrode during multiple charge and discharge cycles (i.e., long-term cycling efficiency) and ion diffusion into the metal oxide. The most well-studied type of ion battery using EIS is the Li-ion battery <sup>15,30,219–224,246–252</sup> due to its commercialization in many portable electronics; however, other Na-ion<sup>200</sup>,205,214,225,229,253 and divalent ion batteries, particularly Zn-ion batteries,<sup>244</sup>,245,254–256 have also been investigated using this technique. Lithium-ion batteries primarily consist of a cathode, anode, and lithium-containing electrolyte present in the form of a solution, solid, or gel electrolyte. 16 The cathode material consists of a lithiated transition metal oxide, and the anode is typically graphite; however, researchers have also explored anodic metal oxides. <sup>257</sup> Upon charging the battery, oxidation of the transition metal oxide cathode is coupled with deintercalation of Li<sup>+</sup> ions. Concomitantly, reduction of the anode results in Li<sup>+</sup> intercalation between graphite layers. Redox half reactions for each of these processes are shown in eqs 15 and 16 for the case of a LiCoO2 cathode and graphite (C) anode. As lithium ions are transferred between electrodes, electrochemical energy is stored as the potential difference between the electrodes is increased. During discharge, intercalation of Li<sup>+</sup> occurs at the cathode upon reduction, and deintercalation occurs at the anode upon oxidation.

$$\text{Li}_{1-x}\text{CoO}_2 + x\text{Li}^+ + x\text{e}^- \rightarrow \text{LiCoO}_2$$
 cathode (15)

$$C + xLi^{+} + xe^{-} \rightarrow Li_{x}C$$
 anode (16)

The reversibility of this process depends greatly on the structure and electrochemical properties of the metal oxide cathode. Oxides such as  $\text{LiCoO}_2$ ,  $\text{LiNiO}_2$ , and  $\text{LiMnO}_2$  possess layered structures where  $\text{Li}^+$  ions are able to diffuse in and out of the host oxide.  $^{3,14,201,236,238,253}$  Other important oxides such as spinel  $\text{LiMn}_2\text{O}_4$  and its substituted derivatives (e.g.,  $\text{LiNi}_{0.5}\text{Mn}_{1.5}\text{O}_4$ ) possess interstitial sites where the occupancy by  $\text{Li}^+$  is variable.  $^{30,220,258-261}$  Importantly, the charge storage capacity of a metal oxide host is limited by the reversible solid-solution range of  $\text{Li}^+$  intercalation in the cathode host structure for a given redox potential of the transition metal cation.  $^{16}$ 

Important features of ion battery electrodes which have been studied by EIS include formation of passivation layers at the surface of cathodes and anodes, charge transfer to the metal oxide electrode, and Li<sup>+</sup> diffusion in the solid state. Passivation layers, also known as solid electrolyte interface (SEI) layers in the Li-ion battery literature, are routinely observed on the cathode and anode surface due to chemical reactivity between the electrodes and electrolyte. The SEI layer can have both detrimental and beneficial effects, including loss in battery capacity over time but enhancement of the cycling efficiency. The formation of passivation layers is modeled using additional parallel RIC circuits such as models B and C discussed above.<sup>3</sup> Importantly, the resistance of the SEI layer is believed to be the result of Li-ion migration through the layer; the growth of such layers over extended cycles leads to higher resistance. One cycles leads to higher resistance. The impedance of solid-state ion diffusion, on the other hand, is described by a Warburg element at low frequency. 4,215,228,236,239 Figure 17 shows a

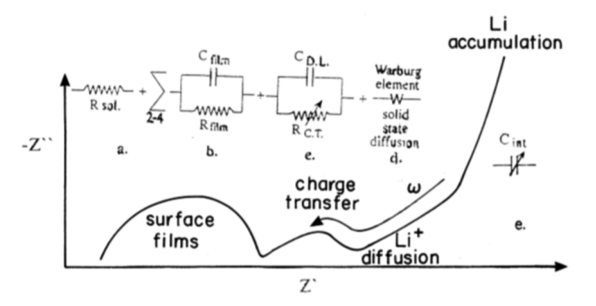


**Figure 17.** General impedance spectra illustration for lithiated electrode and the equivalent circuit analogue. Reproduced with permission from ref 4. Copyright 2000 Elsevier.

description of this behavior provided by Aurbach et al. where the additional arc assigned to formation of a passivation layer (i.e., surface film) occurs at high frequency while the charge transfer resistance associated with energy storage appears in the midfrequency range. Note that the linear portion at low frequency reveals information about Li<sup>+</sup> diffusion as described by Warburg impedance.

In the following sections we discuss specific examples of EIS studies on metal oxides used as cathode and anode materials. We do not cover every example available in the literature and instead give a brief discussion of examples which use EIS to

elucidate particularly important features of metal oxide electrodes in the context of ion batteries.

**4b. Li-Ion Cathode Materials.** Lithium cobalt oxide is the archetype cathode material for Li-ion batteries. <sup>16,17,262</sup> This layered oxide allows for a variable number of Li<sup>+</sup> ions to intercalate between layers of edge-shared cobalt oxide octahedra upon local redox changes in the cobalt oxidation state. <sup>14,263–265</sup> Early studies by Goodenough revealed the presence of passivating surface layers that form by adsorption/decomposition of the electrolyte on the surface of LiCoO<sub>2</sub>. The observed EIS data revealed two semicircles (Figure 18), a

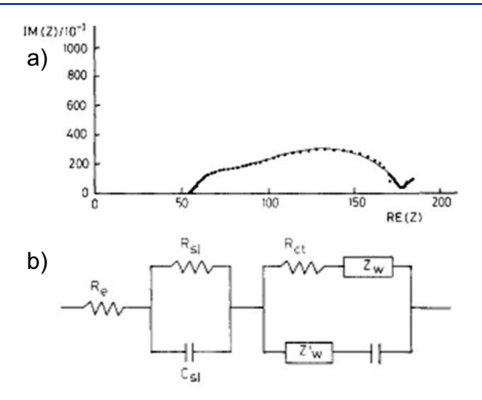


Figure 18. (a) Nyquist plot showing ESI data for a  $\text{Li}_{0.65}\text{CoO}_2$  cathode at potentials up to 4.5 V vs lithium and (b) the equivalent circuit used for fitting. The parallel  $R_{\rm sl} \parallel C_{\rm sl}$  circuit describes the presence of a surface layer on the electrode with a high-frequency response. Reproduced with permission from ref 3. Copyright 1985 Electrochemical Society.

deviation from the expected response of one semicircle representing charge transfer to the transition metal and a high-frequency linear region describing diffusion of Li<sup>+</sup>. The new semicircle appeared at high frequency and increased in size over time. A thorough comparison of equivalent circuit models to account for the second arc resulted in the proposed equivalent circuit shown in Figure 18. Here, a second RllC circuit is included to account for surface layer formation ( $R_{\rm sl}$ ), and a second Warburg diffusion element is included to account for diffusion of Li<sup>+</sup> within the porous electrode structure ( $Z_{\rm W}'$ ). The surface layer formation was attributed to polymerization of propylene carbonate at the electrode surface with  $R_{\rm sl}$  increasing over a 22 h period as the layer grew in thickness.

Another common observation of Li-ion battery cathodes is an increase in  $R_{ct}$  associated with oxidation/reduction of the transition metal over an extended number of charge-discharge cycles. 14,15,221 This observation has been attributed to decomposition of the cathode material, which leads to losses in energy storage. Zhang et al. studied LiCoO2 with a Li<sub>10</sub>GeP<sub>2</sub>S<sub>12</sub> solid-state electrolyte where EIS was used to analyze capacitance fade and increased impedance at the cathode/solid electrolyte interface after being subjected to long-term cycling.<sup>15</sup> Overall, batteries experienced a loss of ~10% storage capacity over the first 100 cycles. Figure 19 shows Nyquist plots collected at the beginning and end of this cycling range where all three semicircle arcs are observed to increase in size after 100 cycles. The midfrequency arc was assigned to charge transfer with the LiCoO<sub>2</sub> cathode which increased from 9 to 118  $\Omega$  cm<sup>2</sup> along with a decreased capacitance. Scanning electron microscopy found that LiCoO<sub>2</sub>

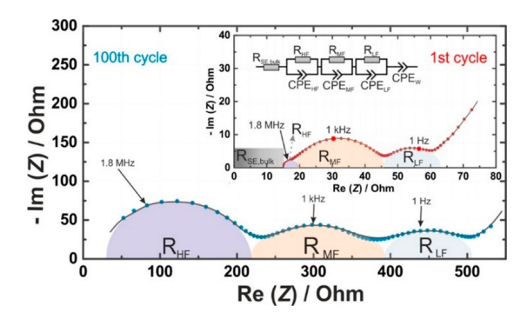


Figure 19. Nyquist plots after 1 charge cycle (inset) vs 100 charge cycles at 3.6 V vs In/InLi. After 100 cycles, decomposition of the  $LiCoO_2$  cathode during cycling was observed as an increase in resistance for the semicircle arc in the midfrequency region, while formation of a surface layer at the  $LiCoO_2$ /electrolyte interface was observed as an increase in resistance for the arc at high frequency. Reproduced with permission from ref 15. Copyright 2018 American Chemical Society.

particles were fractured following extended cycling, hypothesized to result in a loss of contact with the solid-state electrolyte. Electron energy loss spectroscopy also showed migration of cobalt ions from LiCoO<sub>2</sub> into the SEI layer which grew in size over the cycling range. This growth can be observed by a large increase in resistance for the high-frequency arc in the Nyquist plot. The low-frequency arc was assigned to the anode/electrolyte interface.

Lou et al. has followed the decomposition of LiCoO2 and formation of surface layers using energy dispersive spectroscopy (EDS) and EIS as a function of cycle number.<sup>221</sup> Batteries were charged and discharged at 0.6 C (C = charge rate) with a 30% depth of discharge for 100, 400, 800, 1600, 2000, and 2400 cycles. The O:Co ratio rose from 2.34 to 2.96 as the cycling proceeded which suggested slow SEI growth as the cycle number increased. The SEI layer was hypothesized to consist of Li<sub>2</sub>CO<sub>3</sub> on the basis of FTIR data in conjunction with the increase in oxygen content. We note that the ratio may also be explained by a loss of cobalt from the metal oxide. Consistent with results discussed in other studies, the Nyquist plots for EIS data showed a steady increase in both the highfrequency arc assigned to resistance  $(R_p)$  of the SEI layer and the midfrequency arc assigned to charge transfer with LiCoO<sub>2</sub>  $(R_{ct})$ . The linear feature at low frequency was assigned to Warburg diffusion of Li<sup>+</sup> ions; however, this feature was not modeled in this study.

Efforts to stabilize cathodes from decomposition and formation of passivating surface layers have focused on the use of additives to the battery electrolyte.  $^{14,30,221,227,228,234}$  As a recent example, Wu et al. compared EIS data of LiCoO $_2$  cathodes and graphite anodes with and without the additive 4-propyl-[1,3,2]dioxathiolane-2,2-dioxide (PDTD) over multiple charge—discharge cycles. As seen in Figure 20, there was a significant increase in surface layer resistance ( $R_{\rm f}$ ) and  $R_{\rm ct}$  over 150 cycles for both LiCoO $_2$  and graphite. However, the presence of PDTD as an additive stabilized both electrodes, exhibiting smaller increases in  $R_{\rm f}$  and  $R_{\rm ct}$  over the same cycling period. The influence of PDTD is thought to help stabilize the LiCoO $_2$  surface from leaching cobalt ions and forming surface layers.  $^{14}$ 

In other studies of LiCoO<sub>2</sub>, controlling the porosity and grain size of the electrode has been found to influence the EIS results.  $^{201,212,222}$  Annealing Co<sub>3</sub>O<sub>4</sub> and CoO at 350  $^{\circ}$ C resulted in optimal Li storage performance with high discharge

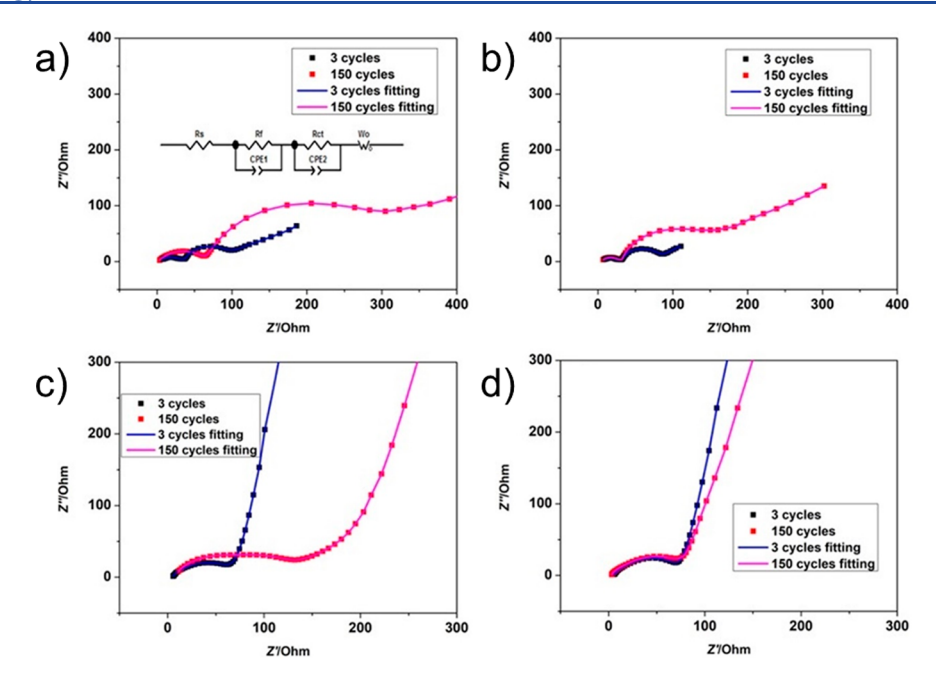


Figure 20. Nyquist plots showing discharge of LiCoO<sub>2</sub> cathodes (a, b) and graphite anodes (c, d) collected in electrolytes without (a, c) and with (b, d) the additive PDTD at the discharge state ( $\sim$ 3.0 V). Large increases in  $R_{\rm f}$  and  $R_{\rm ct}$  without PDTD indicated decomposition of the electrodes over extended cycles. Inclusion of PDTD limited these increases over the same cycling period. Reproduced with permission from ref 14. Copyright 2019 American Chemical Society.

capacities and good long-term cycling stability; at higher annealing temperatures, a larger grain size was attainable which led to a smaller semicircle in the EIS data indicating low resistance from surface film formation.<sup>201</sup>

Electron transport through the metal oxide may also be observed by EIS; however, most electrodes are designed to be highly conductive by mixing the metal oxide with carbon black as a composite. Zhuang et al. was able to observe electron transport for LiMn<sub>2</sub>O<sub>4</sub> as a function of both charging voltage (3.5–4.3 V) and temperature using EIS.<sup>30</sup> As with other Li-ion battery studies, three features were generally observed in the Nyquist plot: two semicircle arcs at high and middle frequencies and a linear Warburg feature at low frequency. These features were assigned to Li-ion migration through the SEI film, charge transfer through the electrode/electrolyte interface, and solid-state diffusion of Li+ ions in the electrode matrix, respectively. However, over the potential range 3.5–3.7 V, an additional semicircle arc in the middle-to-high-frequency region was observed. To investigate the origins of this feature, EIS experiments were performed as a function of temperature. Below 20 °C, the middle-to-high arc frequency could be wellresolved; however, above 20 °C, the semicircles in the highand middle-to-high-frequency ranges began to overlap. This suggested that the semicircle observed in the high-frequency region at room temperature may actually be composed of two distinct features, as seen in Figure 21. These two features were proposed to be due to Li-ion migration through the SEI film at high frequency, as is typically discussed, and electronic transport through the cathode at middle-to-high frequency. Also notable in this study is the predictable dependence of charge transfer resistance and Warburg diffusion as a function of temperature. For low temperatures,  $R_{ct}$  is quite large, and therefore, Warburg diffusion cannot be observed over the finite frequency range. However, as temperature is increased, R<sub>ct</sub> drops precipitously, and the Warburg feature can be clearly observed.

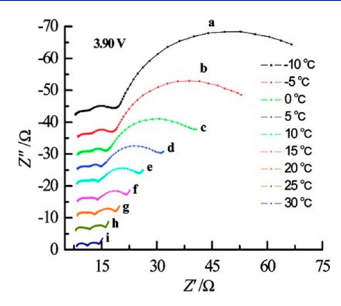
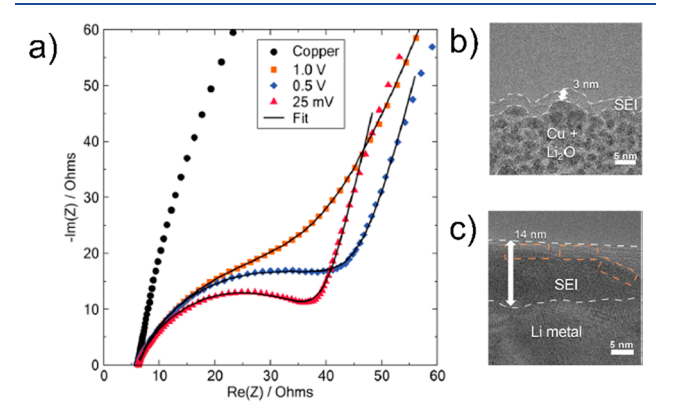


Figure 21. Nyquist plots at various temperatures for a spinel  $LiMn_2O_4$  cathode at 3.90 V. At low temperatures, a third semicircle arc was observed in the middle-to-high-frequency range assigned to electron transport inside the cathode. Reproduced with permission from ref 30. Copyright 2010 American Chemical Society.

4c. Li-lon Anode Materials. Copper(II) oxide has been studied as an anode material for Li-ion batteries where the reduction of copper(II) to copper metal results in reversible formation of Li<sub>2</sub>O according to the reaction CuO + 2Li<sup>+</sup> + 2e<sup>-</sup> → Cu + Li<sub>2</sub>O. The morphological dependence of the CuO electrode has been a particular area of focus in terms of EIS studies. 228,229,232,249,266 Wang et al. have investigated the difference in electrochemical behavior of leaf-like, oatmeal-like, and hollow-spherical CuO structures. 232 Charge storage capacity and long-term cycling efficiency were found to be weakest for the oatmeal-like structure, which showed the lowest porosity based on scanning electron microscopy. EIS was able to provide justification for these results where a noticeably larger  $R_f$  resistance was observed for the oatmeal structure ( $R_f = 321.1 \Omega$ ) than for the leaf ( $R_f = 45.7 \Omega$ ) and hollow-sphere ( $R_f = 43.8 \Omega$ ) structures. Similar to the discussion above for cathode materials, the R<sub>f</sub> resistance is attributed to the formation of a passivation layer at the solid/ electrolyte interface, which is attributed to decreased charge storage capacity. The lower porosity of the oatmeal structure

was proposed to be the main culprit in the higher surface film resistance.

While the morphology of the anode can impact the charge storage capacity and cycling efficiency, the nanostructure of the SEI layer on the anode also affects the electrochemical behavior of the battery during cycling and can be analyzed using EIS. Huang et al. studied the formation of the SEI layer on CuO nanowires following the conversion of CuO to Cu and  $\text{Li}_2\text{O}$ . A Nyquist plot is shown in Figure 22 where the



**Figure 22.** (a) Nyquist plots before the growth of SEI (copper) in addition to SEI formation at 1.0, 0.5, and 0.025 V vs Li/Li $^+$ . Transmission electron micrographs of electrode surfaces following an applied potential of (b) 1.0 V and (c) <0.0 V showing the formation of the SEI layer. Reproduced with permission from ref 235. Copyright 2019 American Chemical Society.

formation of the SEI layer can be observed as a function of the applied potential vs Li<sup>+</sup>/Li. At potentials greater than 1.0 V, the impedance response was capacitive from charge accumulation on the CuO electrode. However, once a potential of 1.0 V was applied, CuO was reduced to Cu and Li2O and a depressed semicircle was observed, characteristic for the formation of an SEI layer. As the potential was lowered from 1.0 to 0.025 V, the semicircle became more well-defined. It was determined that, as the potential begins to approach 0 V, the ionic resistance for Li<sup>+</sup> migration through the SEI layer decreased; however, the thickness of the layer increased. This was determined by transmission electron microscopy collected for samples after each applied potential. The thickness of the SEI layer grew from 3 nm at 1.0 V vs Li<sup>+</sup>/Li to 14 nm upon deposition of Li metal. The decrease in ionic resistance was proposed to be the result of a dense, ionically conductive amorphous layer at lower potentials and highlighted the importance of the structure of the SEI layer and not just its thickness.

 ${\rm TiO_2}$  has also been an interesting material studied for anode applications in Li-ion batteries, but as the direct anode and as a coating material for the anode to enhance overall stability and performance.  $^{267-270}$  Qiu et al. used EIS to study  ${\rm TiO_2}$  reduced graphite nanocomposites as the active anode material in Li-ion batteries. The conductivity of the reduced graphene oxide nanosheets was found to facilitate the charge transfer process in Li-ion batteries.  $^{270}$  As an anode material, the structural and morphological characteristics of oxygen-deficient anatase  ${\rm TiO_2}$  using EIS has been reported.  $^{271-276}$  Liu et al. studied  ${\rm TiO_2}$  electrodes in an aqueous Li-ion battery and the decomposition of inorganic compounds (LiF, Li<sub>2</sub>CO<sub>3</sub>, and Li<sub>2</sub>O) on the surface of  ${\rm TiO_2}$  using EIS in conjunction with scanning

electron microscopy. <sup>276</sup> Balogun et al. studied the capacity and long-term cycling capabilities of oxygen-deficient  ${\rm TiO_2/Li_4Ti_5O_{12}}$  ( ${\rm TiO_2/LTO}$ ) where  ${\rm Li_4Ti_5O_{12}}$  is a chemically lithiated phase grown from  ${\rm TiO_2.}^{274}$   ${\rm Li_4Ti_5O_{12}}$  is of interest because of its well-defined potential for  ${\rm Li^+}$  intercalation at 1.55 V vs  ${\rm Li^+/Li.}$  A comparison of  ${\rm TiO_2}$  nanosheets and  ${\rm TiO_2/LTO}$  nanosheet electrodes with and without annealing under a  ${\rm H_2}$  environment (H-TiO\_2/LTO) revealed the lowest charge transfer resistance for H-TiO\_2/LTO electrodes and the highest  $R_{\rm ct}$  for  ${\rm TiO_2}$  electrodes. This was attributed to a higher concentration of oxygen vacancies in the H-TiO\_2/LTO electrode, as measured by XPS and TGA experiments.

**4d. Na-lon and Zn-lon Batteries.** Various monovalent and divalent ions in addition to Li<sup>+</sup> have been explored in metal oxide ion battery research. In particular, Na<sup>+</sup> has been frequently used as a monovalent ion in studying electrochemical performance of battery materials via EIS. Huang et al. explored silver-containing  $\alpha$ -MnO<sub>2</sub> cathode derivatives, Ag<sub>x</sub>Mn<sub>8</sub>O<sub>16</sub>, where x = 1.22 or 1.66, as a host material for intercalation of Li<sup>+</sup> and Na<sup>+.253</sup>. These oxides possess a 2 × 2 tunnel structure where cations can intercalate. The use of Ag<sup>+</sup> further controls tunnel size and helps stabilize the structure. EIS studies showed that a significant decrease was observed in  $R_{ct}$  associated with charge transfer to the oxide when Na<sup>+</sup> intercalated in and out of the structure (Figure 23).  $R_{ct}$ 

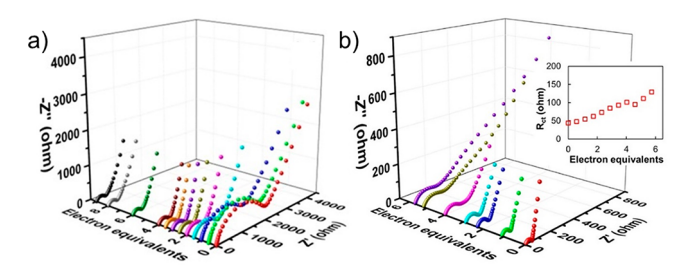


**Figure 23.** Comparison of Nyquist plots obtained from (a)  $Na^+$  intercalation and (b)  $Li^+$  intercalation into  $Ag_{1.22}Mn_8O_{16}$  cathodes. Intercalation of  $Na^+$  resulted in decreased charge transfer resistance, and intercalation of  $Li^+$  resulted in increased charge transfer resistance. Reproduced with permission from ref 253. Copyright 2017 American Chemical Society.

stabilized at a consistent value once 4 electron equivalents of  $\mathrm{Na^+}$  were intercalated into the structure of  $\mathrm{Ag_{1.22}Mn_8O_{16}}$  and 1 electron equivalent for  $\mathrm{Ag_{1.66}Mn_8O_{16}}$ , showing that stable structures were obtained at these conditions. This data was contrasted with results for  $\mathrm{Li^+}$  intercalation where a gradual increase in  $R_{\mathrm{ct}}$  was observed as more  $\mathrm{Li^+}$  ions were incorporated. This result was explained on the basis of the similar ionic radii of  $\mathrm{Na^+}$  and  $\mathrm{Ag^+}$ , which led to very little structure displacement upon intercalation.

Wang et al. have used EIS to compare NaCrO<sub>2</sub> (NCO) powders synthesized via a decomposition reaction, followed by calcination (Ig-NCO) and a solid-state reaction (s-NCO), as cathode materials for Na-ion batteries.<sup>225</sup> These synthetic conditions produce different morphologies which impact the capacity and long-term cycling capabilities of the materials. Studies using TEM and HRTEM reveal that Ig-NCO is made of large particles layered in multiple stacking sheets, whereas the s-NCO product is within the submicron range and has a flakelike particle morphology with distinct edges and an affinity to aggregate. Figure 24 shows EIS curves of Ig-NCO and s-NCO cathodes in the charged state of 3.6 V after different

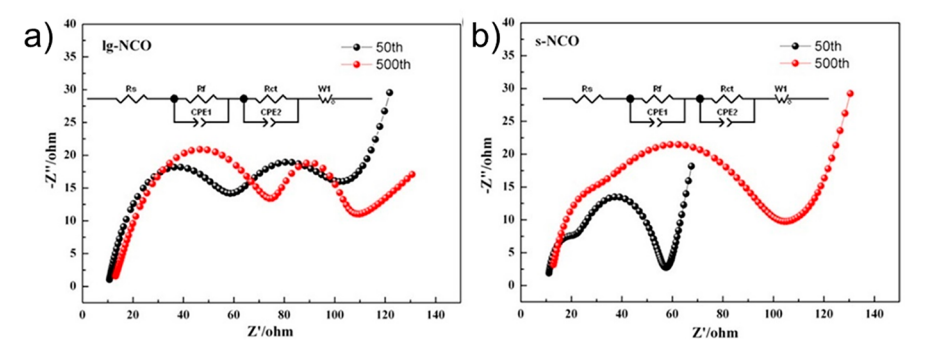
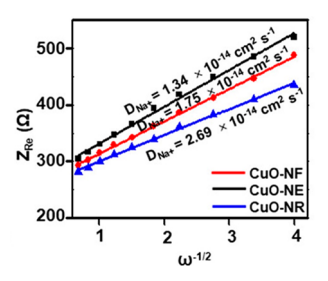


Figure 24. Nyquist plots and their respective equivalent circuits for (a) Ig-NCO electrodes and (b) s-NCO electrodes measured in the charged state of 3.6 V after a different number of cycles. Reproduced with permission from ref 225. Copyright 2019 American Chemical Society.

cycles at 0.1 C (charge rate). The Nyquist plots reveal two semicircles and a linear feature which represent the resistance of the surface film  $R_{\rm ft}$  the charge transfer resistance  $R_{\rm ct}$  and the Warburg impedance  $Z_{\rm w}$ , respectively, as discussed previously for Li-ion battery EIS studies. As the cycling number increased from 50 to 500,  $R_{\rm f}$  for both oxides increased as the surface layer grew; however,  $R_{\rm ct}$  decreased for Ig-NCO and increased for s-NCO. The smaller charge transfer resistance observed in Ig-NCO was attributed to suppression of side reactions due to its small specific surface area and highly (110)-oriented morphology, allowing improved intercalation and deintercalation of Na<sup>+</sup> during cycling.  $^{22.5}$ 

Metal oxide anodes such as CuO have also been studied as anode materials for Na-ion batteries with a reactivity similar to that described for lithium (i.e., CuO + 2Na<sup>+</sup> + 2e<sup>-</sup>  $\rightarrow$  Cu + Na<sub>2</sub>O). Nanoflake, nanoellipsoid, and nanorod structures were compared by Rath et al. using EIS to determine the diffusion coefficients of Na<sup>+</sup> for each structure. <sup>229</sup>  $R_{\rm ct}$  at the electrode/electrolyte interface of the nanorods was significantly lower than what was observed in the other nanostructures; therefore, the Warburg diffusion feature could be clearly resolved. In this case,  $Z_{\rm Re}$  can be plotted directly versus  $\omega^{-1/2}$  and the diffusion coefficient obtained from the slope based on eqs 17 and 18. Figure 25 shows  $Z_{\rm Re}$  vs  $\omega^{-1/2}$  along with determined diffusion



**Figure 25.**  $Z_{\rm Re}$  vs  $\omega^{-1/2}$  plot in the low-frequency region for CuO nanorod, nanoellipsoid, and nanoflake electrodes used as anodes in Na-ion batteries. Reproduced with permission from ref 229. Copyright 2018 American Chemical Society.

coefficients for each nanostructure. The larger diffusion coefficient determined for the nanorod morphology was attributed to a more favorable diffusion path along the length of the rod compared with the other nanostructures.

$$Z_{\rm Re} = R_{\rm e} + R_{\rm ct} + \sigma \omega^{-1/2}$$
 (17)

$$D_{\mathrm{Na}^{+}} = \frac{R^{2}T^{2}}{2A^{2}n^{4}F^{4}C_{0}^{2}\sigma^{2}}$$
 (18)

Exploration of divalent ion batteries using EIS have mostly focused on  $\mathrm{Zn^{2+}};^{244,254,256,278}$  however, some studies have appeared for  $\mathrm{Mg^{2+}}.^{279-281}$  In the case of  $\mathrm{ZnMnO_2}$  batteries, correlations have been deduced using EIS between applied strain and the ionic conductivities of polyacrylamide hydrogel electrolytes.<sup>255</sup> When compressional strain was increased to 22.2%, a dramatic decrease in resistance was observed, which was attributed to a shortened ionic transport distance as the compressional strain increases, thereby improving the efficiency of ionic migration. Zn/δ-MnO<sub>2</sub> cells have also been studied using EIS to compare different cycling points, with equivalent circuit models provided for fitting as seen in Figure 26 to ultimately analyze the voltage and capacity of the material after long-term cycling. 245 The additional circuit component seen in equivalent circuit 2 represents the growth of an additional passivation layer which is likely due to electrolyte decomposition. During cycling, small changes were seen in the resistance due to the electrolyte and the capacitance for the passivation layer. R<sub>ct</sub> decreased and CPE<sub>ct</sub>

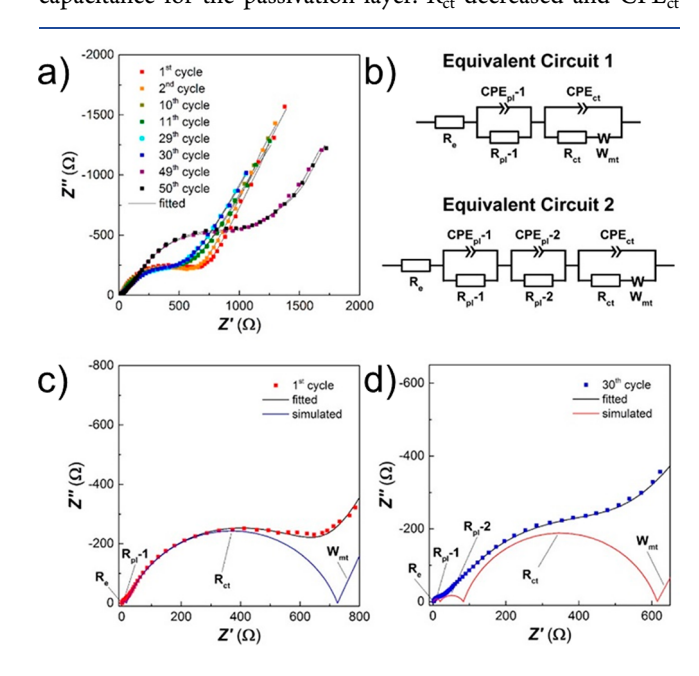


**Figure 26.** (a) Nyquist plots of  $Zn/\delta$ -MnO<sub>2</sub> cells at different cycle numbers. (b) Equivalent circuits. (c) Nyquist plots zoomed in for the first cycle showing minimal contribution for surface layers. (d) Nyquist plots zoomed in for the 30th cycle showing larger contributions from surface layers. Reproduced with permission from ref 245. Copyright 2017 American Chemical Society.

increased up to 30 cycles which could be explained by an increase in the surface area of the active materials.

#### 5. CATALYSIS

**5a.** Overview. Electrocatalysis and photocatalysis of energy relevant chemical reactions using metal oxide electrodes has been investigated by a wide range of electrochemical techniques. In most cases, cyclic or linear sweep voltammetry in combination with chronoamperometry is used for catalysis studies; however, EIS has also been used to study the specific impact of the metal oxide interface on reactivity. Reactions which have been investigated using EIS include the oxygen evolution reaction (OER;  $2H_2O \rightarrow 4e^- + 4H^+ + O_2$ ),  $^{282-313,2,314,315,33,316,5,317-319,37,320-328,31,32,329}$  the oxygen reduction reaction (ORR;  $4e^- + 4H^+ + O_2 \rightarrow 2H_2O$ ),  $^{291,330-338}$  the hydrogen evolution reaction (HER;  $2H^{+} + 2 e^{-} \rightarrow H_{2}$ ), <sup>339–345</sup> as well as various forms of carbon dioxide reduction. These reactions are important for energy applications as they represent the conversion between electrical/solar energy into chemical energy and vice versa. For example, overall water splitting combines OER and HER catalysis to store 4.36 eV of energy per H<sub>2</sub> molecule generated. This reaction is important for the development of efficient electrochemical fuel cells as well as photoelectrochemical cells which convert solar energy directly to chemical energy. 323,333,346,347 In the context of fuel cells and metal—air batteries, ORR is equally important as it represents the thermodynamic reversal of OER and allows for electrical energy to be extracted from O<sub>2</sub>. 334,338,348,349 Development of metal oxide catalysts which can do both OER and ORR has indeed been an active area of research. 336,33

Electro/photocatalytic studies with metal oxides have focused on understanding the impact of morphology, surface defects states, and the purposeful addition of surface layers to enhance reactivity. Morphological changes have largely been modeled using simple Randle circuits (model A in Table 2) where decreased charge transfer resistance is attributed to better catalytic activity. Importantly,  $R_{\rm ct}$  is inversely proportional to the exchange current at each applied potential. Therefore, Tafel plots may be constructed by plotting  $\log(1/R_{\rm ct})$  vs  $E_{\rm app}$  and examining the slope. This method is particularly useful because it is automatically corrected for any series resistance in the electrical circuit. This resistance is known to greatly affect Tafel measurements from other techniques such as linear sweep voltammetry.

Defect states and surface layers have been studied using derivatives of models B and C (Table 2), where surface dependent features are modeled with a second R||C circuit either positioned in series with or imbedded within a primary R||C circuit intended to model the bulk properties of the metal oxide electrode. Particular attention has been paid to the capacitance of defects and surface layers to understand their energy level distribution.  $^{2,31-33,37,319}$  Diffusional resistance of electroactive reactants in solution (H<sub>2</sub>O, H<sup>+</sup>, OH<sup>-</sup>, O<sub>2</sub>, etc.) is not typically observed in these studies due to the inherently complex, multielectron reactions which must occur during charge transfer with the metal oxide.

In the following sections we discuss specific examples of EIS studies used to understand electrocatalysis and photocatalysis with metal oxide electrodes. We focus this discussion on examples related to OER and ORR catalysis given that these reactions are the most studied in the field of metal oxide electrodes across all electrochemical methods. It should be

noted, however, that a small number of HER and CO<sub>2</sub> reduction studies with EIS have been reported. 341–345,349,352

5b. OER/ORR Electrocatalysis. The goal of many electrocatalysis studies with metal oxides is to understand the specific role of surface termination on catalysis. Morphological changes inherently result in different exposed crystal faces and therefore different activation energies for catalysis at each distinct metal oxide surface. EIS has been an effective tool to study the influence of morphology and surface termination on ORR<sup>291,296</sup>,330-332 and OER electrocataly-sis.<sup>282</sup>–284,287,288,290–301,303 Morphologies such as core—shell nanoparticles, 353 nanosheets, 354 nanowires/nanorods, 336 and nanocubes 555 for various metal oxides have been studied by EIS. In these examples, clear changes in the charge transfer resistance of the metal oxide/electrolyte interface were assigned to differences in surface termination based on morphology. For example, Co<sub>3</sub>O<sub>4</sub> nanorods terminated in (110) surfaces along their length were found to exhibit better OER electrocatalysis (i.e., lower  $R_{ct}$ ) than  $Co_3O_4$  nanocubes terminated in (100) facets.<sup>355</sup> However, in many of these examples, metal oxide catalysts were synthesized using solution methods and then deposited onto conductive substrates for EIS measurements. Therefore, knowledge of the specific orientation of the metal oxide surface once deposited is often difficult to have or predict. Precise preparation of metal oxides grown on a single crystalline surface is required to ensure surface termination of a particular facet.

Poulain et al. synthesized electrocatalytic NiO thin films with (100)-, (110)-, and (111)-oriented facets grown on single crystalline MgO substrates.<sup>356</sup> EIS experiments were performed over a range of applied potentials for the three NiO faceted samples where it was observed that the order of  $R_{ct}$ measured for OER was NiO(100) < NiO(111) < NiO(110). This ordering indicated that the (110) surface was the most catalytically active, on the basis of the idea that  $\beta$ -NiOOH formation on the surface resulted in improved catalysis. The authors noted that NiO(111) surfaces observed similarly low  $R_{ct}$  values with NiO(110); however, these surfaces prefer to form a γ-NiOOH phase which is less stable. The much larger  $R_{ct}$  values observed for NiO(100) surfaces were attributed to its lower concentration of hydroxide sites and therefore lower catalytic activity. Cyclic voltammetry and chronoamperometry measurements observed the same ordering in terms of catalytic current.

Other studies of precise metal oxide termination have been reported for LaSrCoO $_3$ . These oxides have been shown to be great catalysts for ORR in the context of solid oxide fuel cells. In these devices, catalysis occurs at the interface between the metal oxide and a gas phase environment, as opposed to a liquid phase electrolyte which has been discussed throughout this review. Reduction of  $O_2$  at these metal oxide catalysts results in an uptake of oxygen atoms into the lattice, which diffuse through a solid-state electrolyte such as yttria stabilized zirconia (YSZ) to the anode catalyst where they form  $H_2O$  upon oxidation of  $H_2$ .

Lee et al. studied  $\text{La}_2\text{NiO}_{4+\delta}$  thin films oriented on the (100) facet grown via pulsed layer deposition on YSZ substrates for ORR. Sas EIS measurements were used to show a dramatic dependence of electrocatalysis on film thickness and the partial pressure of oxygen. Figure 27 shows Nyquist plots obtained at 550 °C for both variables where  $R_{\rm ct}$  decreased for thinner films and higher partial pressures. These results suggested that thinner films were able to incorporate oxygen into their lattice

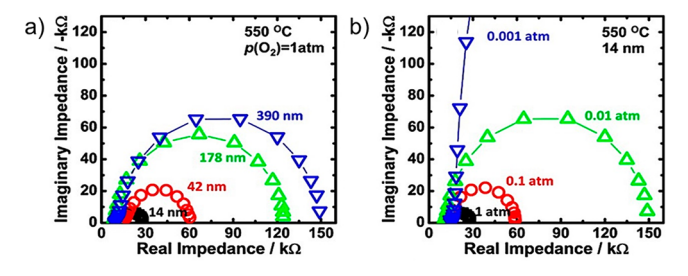


**Figure 27.** EIS results of microelectrodes for (100)-oriented epitaxial  $\text{La}_2\text{NiO}_{4+\delta}$  thin films with varied (a) thickness and (b) oxygen partial pressure. The oxygen dependent data is shown for a 14 nm thick film. Reproduced with permission from ref 338. Copyright 2013 the American Chemical Society.

via surface oxygen exchange with a larger rate constant. High-resolution X-ray diffraction showed that thinner films were highly strained along the c-axis due to lattice mismatch with the substrate. The strained lattice was therefore believed to be responsible for the larger rate constant of surface oxygen exchange. Similar results have been observed by Lee et al. for (001)-oriented La<sub>0.6</sub>Sr<sub>0.4</sub>CoO<sub>3- $\delta$ </sub> where larger in-plane tensile strain observed for thinner metal oxide films resulted in smaller charge transfer resistance due to oxygen exchange. <sup>334</sup> Additionally, these studies showed improved ORR kinetics due to a Sr-rich layer near the film surface.

**5c. OER Photocatalysis.** EIS studies coupled with steady-state photoexcitation of semiconductor metal oxides have been reported for investigating OER photocatalysis. M u c h of this work has focused on α-Fe<sub>2</sub>O<sub>3</sub><sup>2,5,31,32,37,314,315,317,318,320,321,324,325,328</sup> and BiVO<sub>4</sub><sup>33,285,286,297,302,316,319,326,357</sup> due to their narrow band gaps and visible light absorption; however, UV photocatalysis with TiO<sub>2</sub>,  $^{358-361}$  ZnO,  $^{339,362}$  IrO<sub>2</sub>,  $^{340,353,363}$  and copper delafossites  $^{323,327}$  have also been reported. Here we focus on EIS studies that have been particularly important in understanding the role of surface defect states and cocatalysts in α-Fe<sub>2</sub>O<sub>3</sub> and BiVO<sub>4</sub> photoelectrodes.

The role of surface defect states in  $\alpha$ -Fe<sub>2</sub>O<sub>3</sub> for photocatalytic OER has recently been reviewed by Tang and Arbiol. 364 These states naturally occur due to the contact of the metal oxide with the oxygen-rich aqueous solution. Klahr et al. reported a detailed EIS study that showed the significance of these states in the OER mechanism.<sup>2</sup> Figure 28 shows a Nyquist plot of EIS data collected at 0.65 and 0.70 V vs Ag/ AgCl under 1 sun illumination by a white light source. The equivalent circuit used to model these data is shown in Figure 28 where  $R_{\text{ct,trap}}$  and  $C_{\text{trap}}$  refer to the charge transfer and capacitance associated with defect (trap) states at the metal oxide/electrolyte interface. The terms  $R_{ct,bulk}$  and  $C_{bulk}$  refer to the charge transfer and capacitance of bulk valence band states, and  $R_{\text{trapping}}$  describes the impedance associated with transferring holes between the bulk and surface defects. Theoretical justification for this model has been provided by Bisquert,<sup>365</sup> and this model is commonly used to describe surface defects in metal oxide semiconductors. 20,366-368 Modeling of the data revealed that  $R_{ct,bulk} = 0$  under illumination, and all charge transfer through the metal oxide/electrolyte interface occurred through defect states described by the larger, low-frequency semicircle arc. The smaller, high-frequency arc was assigned to the parallel combination of  $R_{\text{trapping}} \| C_{\text{bulk}}$ . In the absence of illumination, only a single semicircle arc was observed, and therefore,  $R_{\text{ct,trap}} = 0$ . This was an important result because it

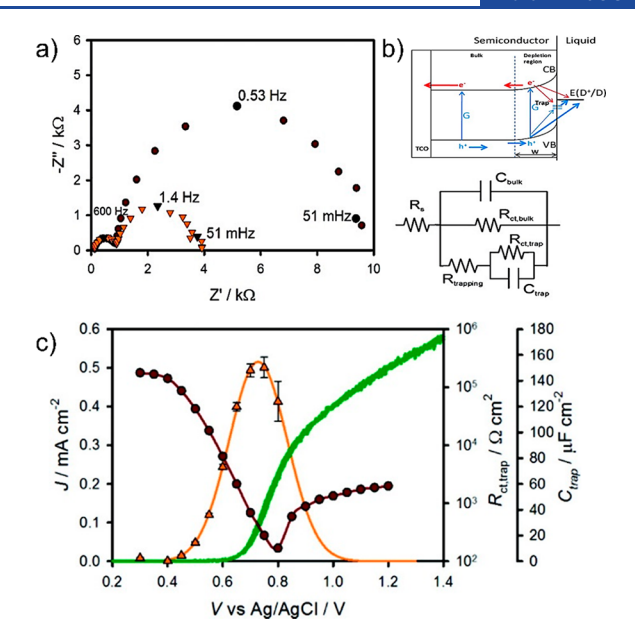


**Figure 28.** (a) Nyquist plots measured at pH 6.9 with applied potentials of 0.65 V (red circles) and 0.70 V vs Ag/AgCl (orange triangles) under 1 sun illumination. (b) Band diagram showing trap states relative to the conduction and valence bands of α-Fe<sub>2</sub>O<sub>3</sub> along with the equivalent circuit used to model EIS data. (c) Gaussian distribution of  $C_{\text{trap}}$  (orange triangles) and  $R_{\text{ct,trap}}$  (red circles) measured by EIS overlaid with photocurrent measured by linear sweep voltammetry (green line). Reproduced with permission from ref 2. Copyright 2012 American Chemical Society.

indicated that defect states were only able to participate in OER if they were populated by holes under illumination. The capacitance associated with these defect states could be measured as a function of applied potential where a Gaussian distribution of states was observed just above the valence band edge. Other characteristic results such as a 59 mV shift in their energy levels with pH and an increase in their capacitance with illumination intensity further corroborated their existence. Importantly, the energetic distribution of these states was shown to occur directly at the onset of photocurrent measured by linear sweep voltammetry, indicating their importance in OER photocatalysis (Figure 28).

In a series of follow-up studies, Klahr et al. used similar EIS methods to study  $\alpha$ -Fe<sub>2</sub>O<sub>3</sub> photocatalysis of  $[Fe^{II}(CN)_6]^{4-}$  on bare electrodes<sup>2</sup> and of H<sub>2</sub>O with the addition of a Co-Pi (cobalt phosphate) cocatalysts.<sup>5</sup> The [Fe<sup>II</sup>(CN)<sub>6</sub>]<sup>4-</sup> allowed them to observe the maximum photocatalytic properties of the metal oxide including contributions for surface defect states. The addition of Co-Pi to the surface of a-Fe<sub>2</sub>O<sub>3</sub> resulted in larger photocurrent and a lower onset potential for OER. Similar studies had previously been reported, 5,37 but Klahr et al. were able show the dependence of OER photocatalysis on the density and distribution of Co-Pi electronic states using EIS. Figure 29 shows the capacitance of these states measured under illumination as a function of Co-Pi thickness deposited via photoelectrodeposition and expressed as the quantity of charge passed in mC cm<sup>-2</sup>. Data were obtained on the basis of an equivalent circuit similar to that shown in Figure 28 above. The capacitance data clearly showed an increase in the density of Co-Pi states above those for the surface defect states (SS) of the underlying  $\alpha$ -Fe<sub>2</sub>O<sub>3</sub>. As the thickness of Co-Pi grew, the entire \alpha-Fe2O3 surface became coated and the surface capacitance was only reflective of Co-Pi. Concomitant with

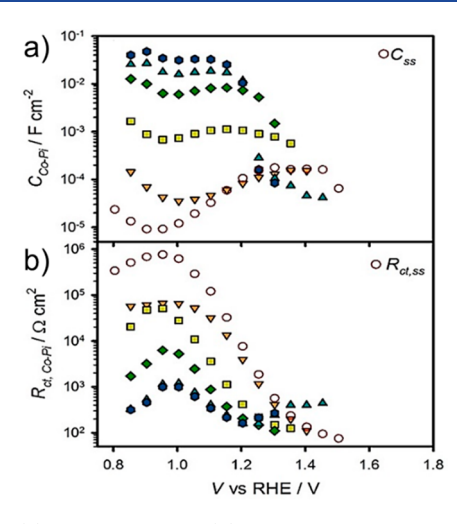


Figure 29. (a) Capacitance and (b) resistance values measured for the Co-Pi catalyst deposited on the surface of  $\alpha$ -Fe<sub>2</sub>O<sub>3</sub> photoelectrodes. Colored symbols represent different amounts of deposited catalyst: 0 (red open circles), 1 (orange triangles), 2 (yellow squares), 15 (green diamonds), 45 (teal triangles), and 90 mC cm<sup>-2</sup> (blue hexagons). Reproduced with permission from ref 5. Copyright 2012 American Chemical Society.

the growth of Co-Pi capacitance was a decrease in R<sub>ct.Co-Pi</sub> as these states became the active sites for OER catalysis. A more recent study by Carroll and Gamelin deposited Co-Pi onto a mesoporous  $\alpha$ -Fe<sub>2</sub>O<sub>3</sub> photoelectrode and observed similar EIS behavior in terms of capacitance and resistance associated with OER catalysis by Co-Pi surface states.<sup>37</sup> The mesoporous structure of  $\alpha$ -Fe<sub>2</sub>O<sub>3</sub>, however, resulted in a  $\sim$ 1.5× increase in photocurrent at 1.6 V vs RHE due to the higher surface area of the photoelectrode.

In addition to  $\alpha$ -Fe<sub>2</sub>O<sub>3</sub>, BiVO<sub>4</sub> has also been extensively studied for OER photocatalysis. <sup>33,285,286,297,302,316,319,357</sup> Jeong et al. studied BiVO<sub>4</sub> photoelectrodes modified by hexavelent dopants (Cr<sup>6+</sup>, W<sup>6+</sup>, and Mo<sup>6+</sup>), heterojunction formation with WO<sub>3</sub>, and deposition of Co-Pi as a cocatalyst. <sup>286</sup> EIS data revealed lower charge transfer resistances for OER for WO<sub>3</sub>/ BiVO<sub>4</sub> heterojuctions due to an increase in light absorption and the incorporation of the Co-Pi cocatalyst. Doping with  $W^{6+}$  and  $Mo^{6+}$  was also found to slightly decrease  $R_{ct}$ ; however,  $Cr^{6+}$  resulted in a larger  $R_{ct}$ . In-depth analysis of surface state contributions was not performed in this particular study. However, Shi et al. recently presented a detailed EIS study on W-doped BiVO<sub>4</sub> photoelectrodes where the %W was varied from 0 to 5%. 33 Photocurrent as a result of OER was found to increase dramatically from 0 to 2% doping and then decrease for 5%. EIS data collected under illumination and fit to an equivalent circuit similar to that shown in Figure 30 revealed that surface states were induced by W-dopants and maximized in their capacitance at the 2% level. A decrease in surface state capacitance for 5% W<sup>6+</sup> was consistent with photocurrent data. The maximized benefit of W-doping was reasoned on the basis of a balance in the density of surface states which controlled catalysis at the metal oxide surface and the density of dopant donors in the bulk which contributed to conductivity and extraction of electrons.

Further studies of BiVO<sub>4</sub> photoelectrodes with EIS have shown that continuous illumination under basic pH conditions can also result in a high concentration of surface states without the need for dopants. Trześniewski et al. synthesized BiVO<sub>4</sub>

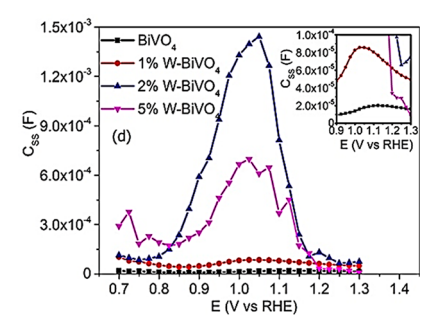


Figure 30. Surface state capacitance obtained from fitting photoinduced EIS data for BiVO<sub>4</sub> and 1%, 2%, and 5% doped W-BiVO<sub>4</sub> photoelectrodes. Reproduced with permission from ref 33. Copyright 2018 American Chemical Society.

thin films of 50, 100, 200, and 300 nm thicknesses by spray pyrolysis and exposed them to 10 h of continuous solar simulated illumination. The EIS measurements and subsequent modeling with the same equivalent circuit shown in Figure 30 showed the existence of a broad distribution of surface states as opposed to the monoenergetic distribution observed for W-doped BiVO<sub>4</sub> and  $\alpha$ -Fe<sub>2</sub>O<sub>3</sub> discussed above. The mechanism of formation of these states was proposed to be due to trapping of photoexcited electrons via reduction of  $V^{5+} \rightarrow V^{4+}$  in the bulk and subsequent migration of holes to the surface to form an adsorbed layer of oxyl/hydroxyl species. Importantly, the phototreatment of BiVO<sub>4</sub> electrodes resulted in greatly improved photocatalysis for OER where the internal quantum efficiency increased from ~20% for untreated electrodes to ~100% following phototreatment at pH 10.

#### 6. CONCLUSIONS AND OUTLOOK

In conclusion, EIS is a highly versatile technique that can be used to study metal oxide electrodes in a wide variety of energy applications. The key feature of this electrochemical method is the frequency dependence exhibited by fundamental circuit elements used to describe the flow of current through the metal oxide interface. Modeling EIS data to well-supported equivalent circuits is a critical aspect toward gaining physically relevant information. Detailed studies as a function of modulation frequency and applied potential can reveal significant information about the capacitance of electronic states and their resistance for electron transfer.

Data such as this is important to wide band gap metal oxide semiconductors used in heterojunction solar cells. Understanding the energy distribution of electronic defects states within the band gap can lead to improvements in performance by controlling the prevalence for these states. By far, the largest amount of work has been focused on n-type metal oxide semiconductors such as TiO2, ZnO, and SnO2. A similar level of detailed studies on p-type metal oxides such as NiO and CuGaO<sub>2</sub> is warranted. In particular, charge transport through these metal oxides is uniquely complex given the mixed metal/ oxygen valence band. Fundamental EIS studies could lead to great improvement in our understanding of these materials.

In terms of ion batteries, understanding the role of surface passivation layers that occurs at anodes and cathodes is of great importance for energy storage. Extended battery cycling has shown a continuous increase in these layers which contributes to higher overall resistance for electrical energy storage and thus degraded battery performance. EIS has proven to be important in this regard and will continue to be used to analyze

new metal oxide electrodes as they are discovered. While metal oxides are commercially used for Li-ion batteries, a push to develop metal oxide battery electrodes for application in alternative ion batteries is of great interest. Low-toxicity battery components that are environmentally friendly and composed of earth abundant metals are ideal for future advancements in energy storage devices. Candidates include both alternative monovalent ion batteries such as Na<sup>+</sup> and K<sup>+</sup> as well as multivalent ion batteries such as Zn<sup>2+</sup> and Ca<sup>2+</sup>. As metal oxides are investigated to be implemented in alternative ion batteries, EIS will prove to be a useful analytical technique to measure their performance capabilities for these relatively new and scarcely studied applications.

The use of metal oxide electrodes as electrocatalysts and photocatalysts for energy relevant chemical reactions such as oxygen evolution/reduction and proton reduction will continue to be an important area of research due to the need to convert renewable forms of energy into chemical fuels. EIS has been applied rather sparingly in this area, likely due to the fact that other techniques such as linear sweep voltammetry are more easily applied, yet the opportunity for further studies is enormous. Studies highlighted here show the impact EIS can have on developing an intimate understanding of defect states at the metal oxide interface and the influence of these states on catalysis. Further EIS studies in the areas of metal oxide degradation in aqueous media and the use of metal oxide surface layers to protect crystalline semiconductor surfaces could provide useful knowledge about long-term stability of metal oxide interfaces.

#### AUTHOR INFORMATION

#### **Corresponding Author**

\*E-mail: farnum@auburn.edu.

ORCID

Byron H. Farnum: 0000-0001-9152-1909

**Author Contributions** 

<sup>†</sup>A.R.C.B., A.L.C., and A.R.B. contributed equally.

Notes

The authors declare no competing financial interest.

#### ACKNOWLEDGMENTS

The authors acknowledge support from the National Science Foundation, Division of Materials Research and EPSCoR through Grant 1809847. A.R.C.B. acknowledges financial support from the Alabama Graduate Research Scholars Program (GRSP) funded through the Alabama Commission for Higher Education and administered by the Alabama EPSCoR. We also acknowledge support from the Department of Chemistry and Biochemistry at Auburn University.

#### REFERENCES

- (1) Bisquert, J.; Fabregat-Santiago, F. Impedance Spectroscopy: A General Introduction and Application to Dye-Sensitized Solar Cells. In *Dye-Sensitized Solar Cells*; EPFL Press, 2010.
- (2) Klahr, B.; Gimenez, S.; Fabregat-Santiago, F.; Hamann, T.; Bisquert, J. Water Oxidation at Hematite Photoelectrodes: The Role of Surface States. *J. Am. Chem. Soc.* **2012**, *134* (9), 4294–4302.
- (3) Thomas, M. G. S. R.; Bruce, P. G.; Goodenough, J. B. AC Impedance Analysis of Polycrystalline Insertion Electrodes: Application to Li1 x CoO2. *J. Electrochem. Soc.* **1985**, 132 (7), 1521–1528.
- (4) Aurbach, D. Review of Selected Electrode–Solution Interactions Which Determine the Performance of Li and Li Ion Batteries. *J. Power Sources* **2000**, *89* (2), 206–218.

- (5) Klahr, B.; Gimenez, S.; Fabregat-Santiago, F.; Bisquert, J.; Hamann, T. W. Photoelectrochemical and Impedance Spectroscopic Investigation of Water Oxidation with "Co-Pi"-Coated Hematite Electrodes. J. Am. Chem. Soc. 2012, 134 (40), 16693–16700.
- (6) von Hauff, E. Impedance Spectroscopy for Emerging Photovoltaics. J. Phys. Chem. C 2019, 123 (18), 11329-11346.
- (7) Hagfeldt, A.; Boschloo, G.; Sun, L.; Kloo, L.; Pettersson, H. Dye-Sensitized Solar Cells. *Chem. Rev.* **2010**, *110* (11), 6595–6663.
- (8) Carey, G. H.; Abdelhady, A. L.; Ning, Z.; Thon, S. M.; Bakr, O. M.; Sargent, E. H. Colloidal Quantum Dot Solar Cells. *Chem. Rev.* **2015**, *115* (23), 12732–12763.
- (9) Kim, M. R.; Ma, D. Quantum-Dot-Based Solar Cells: Recent Advances, Strategies, and Challenges. *J. Phys. Chem. Lett.* **2015**, 6 (1), 85–99.
- (10) Clarke, T. M.; Durrant, J. R. Charge Photogeneration in Organic Solar Cells. Chem. Rev. 2010, 110 (11), 6736–6767.
- (11) Snaith, H. J. Perovskites: The Emergence of a New Era for Low-Cost, High-Efficiency Solar Cells. J. Phys. Chem. Lett. 2013, 4 (21), 3623–3630.
- (12) Hamann, T. W. Splitting Water with Rust: Hematite Photoelectrochemistry. Dalton Trans 2012, 41 (26), 7830-7834.
- (13) Prévot, M. S.; Jeanbourquin, X. A.; Bourée, W. S.; Abdi, F.; Friedrich, D.; van de Krol, R.; Guijarro, N.; Le Formal, F.; Sivula, K. Evaluating Charge Carrier Transport and Surface States in CuFeO2 Photocathodes. *Chem. Mater.* **2017**, 29 (11), 4952–4962.
- (14) Wu, S.; Lin, Y.; Xing, L.; Sun, G.; Zhou, H.; Xu, K.; Fan, W.; Yu, L.; Li, W. Stabilizing LiCoO2/Graphite at High Voltages with an Electrolyte Additive. *ACS Appl. Mater. Interfaces* **2019**, *11* (19), 17940–17951.
- (15) Zhang, W.; Richter, F. H.; Culver, S. P.; Leichtweiss, T.; Lozano, J. G.; Dietrich, C.; Bruce, P. G.; Zeier, W. G.; Janek, J. Degradation Mechanisms at the Li10GeP2S12/LiCoO2 Cathode Interface in an All-Solid-State Lithium-Ion Battery. ACS Appl. Mater. Interfaces 2018, 10 (26), 22226–22236.
- (16) Goodenough, J. B.; Park, K.-S. The Li-Ion Rechargeable Battery: A Perspective. *J. Am. Chem. Soc.* **2013**, *135* (4), 1167–1176. (17) Mizushima, K.; Jones, P. C.; Wiseman, P. J.; Goodenough, J. B. LixCoO2 (0 < x<-1): A New Cathode Material for Batteries of High Energy Density. *Mater. Res. Bull.* **1980**, *15* (6), 783–789.
- (18) Cesiulis, H.; Tsyntsaru, N.; Ramanavicius, A.; Ragoisha, G. The Study of Thin Films by Electrochemical Impedance Spectroscopy. In *Nanostructures and Thin Films for Multifunctional Applications*; Tiginyanu, I., Topala, P., Ursaki, V., Eds.; Springer International Publishing: Cham, 2016; pp 3–42.
- (19) Fabregat-Santiago, F.; Mora-Seró, I.; Garcia-Belmonte, G.; Bisquert, J. Cyclic Voltammetry Studies of Nanoporous Semiconductors. Capacitive and Reactive Properties of Nanocrystalline TiO2 Electrodes in Aqueous Electrolyte. *J. Phys. Chem. B* **2003**, *107* (3), 758–768.
- (20) Ponomarev, E. A.; Peter, L. M. A Comparison of Intensity Modulated Photocurrent Spectroscopy and Photoelectrochemical Impedance Spectroscopy in a Study of Photoelectrochemical Hydrogen Evolution at P-InP. *J. Electroanal. Chem.* **1995**, 397 (1–2), 45–52.
- (21) Schefold, J. Impedance and Intensity Modulated Photocurrent Spectroscopy as Complementary Differential Methods in Photoelectrochemistry. *J. Electroanal. Chem.* **1992**, 341 (1–2), 111–136.
- (22) Bard, A. J.; Faulkner, L. R. Electrochemical Methods: Fundamentals and Applications, 2nd ed.; Wiley, 2001.
- (23) Wang, H.; Guerrero, A.; Bou, A.; Al-Mayouf, A. M.; Bisquert, J. Kinetic and Material Properties of Interfaces Governing Slow Response and Long Timescale Phenomena in Perovskite Solar Cells. *Energy Environ. Sci.* **2019**, *12* (7), 2054–2079.
- (24) Almora, O.; García-Batlle, M.; Garcia-Belmonte, G. Utilization of Temperature-Sweeping Capacitive Techniques to Evaluate Band Gap Defect Densities in Photovoltaic Perovskites. *J. Phys. Chem. Lett.* **2019**, *10* (13), 3661–3669.

- (25) Fischer, M.; Tvingstedt, K.; Baumann, A.; Dyakonov, V. Doping Profile in Planar Hybrid Perovskite Solar Cells Identifying Mobile Ions. ACS Appl. Energy Mater. 2018, 1 (10), 5129–5134.
- (26) Garcia-Belmonte, G.; Bisquert, J. Distinction between Capacitive and Noncapacitive Hysteretic Currents in Operation and Degradation of Perovskite Solar Cells. ACS Energy Lett. 2016, 1 (4), 683–688.
- (27) Almora, O.; Aranda, C.; Mas-Marzá, E.; Garcia-Belmonte, G. On Mott-Schottky Analysis Interpretation of Capacitance Measurements in Organometal Perovskite Solar Cells. *Appl. Phys. Lett.* **2016**, 109 (17), 173903.
- (28) Bisquert, J. Theory of the Impedance of Electron Diffusion and Recombination in a Thin Layer. *J. Phys. Chem. B* **2002**, *106* (2), 325–333.
- (29) Bisquert, J. Influence of the Boundaries in the Impedance of Porous Film Electrodes. *Phys. Chem. Chem. Phys.* **2000**, 2 (18), 4185–4192.
- (30) Zhuang, Q.-C.; Wei, T.; Du, L.-L.; Cui, Y.-L.; Fang, L.; Sun, S.-G. An Electrochemical Impedance Spectroscopic Study of the Electronic and Ionic Transport Properties of Spinel LiMn <sub>2</sub> O <sub>4</sub>. *J. Phys. Chem. C* **2010**, *114* (18), 8614–8621.
- (31) Klahr, B.; Hamann, T. Water Oxidation on Hematite Photoelectrodes: Insight into the Nature of Surface States through In Situ Spectroelectrochemistry. *J. Phys. Chem. C* **2014**, *118* (19), 10393–10399.
- (32) Klahr, B.; Gimenez, S.; Fabregat-Santiago, F.; Bisquert, J.; Hamann, T. W. Electrochemical and Photoelectrochemical Investigation of Water Oxidation with Hematite Electrodes. *Energy Environ. Sci.* **2012**, *5* (6), 7626.
- (33) Shi, Q.; Murcia-López, S.; Tang, P.; Flox, C.; Morante, J. R.; Bian, Z.; Wang, H.; Andreu, T. Role of Tungsten Doping on the Surface States in BiVO 4 Photoanodes for Water Oxidation: Tuning the Electron Trapping Process. ACS Catal. 2018, 8 (4), 3331–3342.
- (34) Bredar, A. R. C.; Blanchet, M. D.; Comes, R. B.; Farnum, B. H. Evidence and Influence of Copper Vacancies in P-Type CuGaO2-Mesoporous Films. ACS Appl. Energy Mater. 2019, 2 (1), 19–28.
- (35) Herraiz-Cardona, I.; Fabregat-Santiago, F.; Renaud, A.; Julián-López, B.; Odobel, F.; Cario, L.; Jobic, S.; Giménez, S. Hole Conductivity and Acceptor Density of P-Type CuGaO2 Nanoparticles Determined by Impedance Spectroscopy: The Effect of Mg Doping. *Electrochim. Acta* 2013, 113, 570–574.
- (36) Fabregat-Santiago, F.; Garcia-Belmonte, G.; Bisquert, J.; Zaban, A.; Salvador, P. Decoupling of Transport, Charge Storage, and Interfacial Charge Transfer in the Nanocrystalline TiO2/Electrolyte System by Impedance Methods. *J. Phys. Chem. B* **2002**, *106* (2), 334–339.
- (37) Carroll, G. M.; Gamelin, D. R. Kinetic Analysis of Photoelectrochemical Water Oxidation by Mesostructured Co-Pi/ $\alpha$ -Fe  $_2$  O  $_3$  Photoanodes. *J. Mater. Chem. A* **2016**, 4 (8), 2986–2994.
- (38) Rühle, S.; Anderson, A. Y.; Barad, H.-N.; Kupfer, B.; Bouhadana, Y.; Rosh-Hodesh, E.; Zaban, A. All-Oxide Photovoltaics. *J. Phys. Chem. Lett.* **2012**, 3 (24), 3755–3764.
- (39) Toyoda, T.; Shen, Q. Quantum-Dot-Sensitized Solar Cells: Effect of Nanostructured TiO2Morphologies on Photovoltaic Properties. *J. Phys. Chem. Lett.* **2012**, *3* (14), 1885–1893.
- (40) Bai, Y.; Mora-Seró, I.; De Angelis, F.; Bisquert, J.; Wang, P. Titanium Dioxide Nanomaterials for Photovoltaic Applications. *Chem. Rev.* **2014**, *114* (19), 10095–10130.
- (41) Zhen, C.; Wu, T.; Chen, R.; Wang, L.; Liu, G.; Cheng, H.-M. Strategies for Modifying TiO2 Based Electron Transport Layers to Boost Perovskite Solar Cells. ACS Sustainable Chem. Eng. 2019, 7 (5), 4586–4618.
- (42) Huang, J.; Yin, Z.; Zheng, Q. Applications of ZnO in Organic and Hybrid Solar Cells. *Energy Environ. Sci.* **2011**, 4 (10), 3861–3877.
- (43) Anta, J. A.; Guillén, E.; Tena-Zaera, R. ZnO-Based Dye-Sensitized Solar Cells. *J. Phys. Chem. C* **2012**, *116* (21), 11413–11425.

- (44) Chappel, S.; Chen, S.-G.; Zaban, A. TiO2-Coated Nanoporous SnO2 Electrodes for Dye-Sensitized Solar Cells. *Langmuir* **2002**, *18* (8), 3336–3342.
- (45) Ramasamy, E.; Lee, J. Ordered Mesoporous SnO2-Based Photoanodes for High-Performance Dye-Sensitized Solar Cells. *J. Phys. Chem. C* **2010**, *114* (50), 22032–22037.
- (46) Tiwana, P.; Docampo, P.; Johnston, M. B.; Snaith, H. J.; Herz, L. M. Electron Mobility and Injection Dynamics in Mesoporous ZnO, SnO2, and TiO2 Films Used in Dye-Sensitized Solar Cells. *ACS Nano* **2011**, *5* (6), 5158–5166.
- (47) Sayama, K.; Sugihara, H.; Arakawa, H. Photoelectrochemical Properties of a Porous Nb2O5 Electrode Sensitized by a Ruthenium Dye. *Chem. Mater.* **1998**, *10* (12), 3825–3832.
- (48) Ling, X.; Yuan, J.; Liu, D.; Wang, Y.; Zhang, Y.; Chen, S.; Wu, H.; Jin, F.; Wu, F.; Shi, G.; Tang, X.; Zheng, J.; Liu, S.; Liu, Z.; Ma, W. Room-Temperature Processed Nb2O5 as the Electron-Transporting Layer for Efficient Planar Perovskite Solar Cells. ACS Appl. Mater. Interfaces 2017, 9 (27), 23181–23188.
- (49) Lenzmann, F.; Krueger, J.; Burnside, S.; Brooks, K.; Grätzel, M.; Gal, D.; Rühle, S.; Cahen, D. Surface Photovoltage Spectroscopy of Dye-Sensitized Solar Cells with TiO2, Nb2O5, and SrTiO3 Nanocrystalline Photoanodes: Indication for Electron Injection from Higher Excited Dye States. *J. Phys. Chem. B* **2001**, *105* (27), 6347–6352.
- (50) Yang, S.; Kou, H.; Wang, J.; Xue, H.; Han, H. Tunability of the Band Energetics of Nanostructured SrTiO3 Electrodes for Dye-Sensitized Solar Cells. *J. Phys. Chem. C* **2010**, *114* (9), 4245–4249.
- (51) Bera, A.; Wu, K.; Sheikh, A.; Alarousu, E.; Mohammed, O. F.; Wu, T. Perovskite Oxide SrTiO3 as an Efficient Electron Transporter for Hybrid Perovskite Solar Cells. *J. Phys. Chem. C* **2014**, *118* (49), 28494–28501.
- (52) Lana-Villarreal, T.; Boschloo, G.; Hagfeldt, A. Nanostructured Zinc Stannate as Semiconductor Working Electrodes for Dye-Sensitized Solar Cells. *J. Phys. Chem. C* **2007**, *111* (14), 5549–5556.
- (53) Tan, B.; Toman, E.; Li, Y.; Wu, Y. Zinc Stannate (Zn2SnO4) Dye-Sensitized Solar Cells. *J. Am. Chem. Soc.* **2007**, *129* (14), 4162–4163.
- (54) Mali, S. S.; Su Shim, C.; Kook Hong, C. Highly Porous Zinc Stannate ( $\rm Zn_2SnO_4$ ) Nanofibers Scaffold Photoelectrodes for Efficient Methyl Ammonium Halide Perovskite Solar Cells. *Sci. Rep.* **2015**, *S*, 11424.
- (55) Corma, A.; Atienzar, P.; García, H.; Chane-Ching, J.-Y. Hierarchically Mesostructured Doped CeO 2 with Potential for Solar-Cell Use. *Nat. Mater.* **2004**, *3* (6), 394–397.
- (56) Song, W.; Gong, Y.; Tian, J.; Cao, G.; Zhao, H.; Sun, C. Novel Photoanode for Dye-Sensitized Solar Cells with Enhanced Light-Harvesting and Electron-Collection Efficiency. *ACS Appl. Mater. Interfaces* **2016**, 8 (21), 13418–13425.
- (57) He, J.; Lindström, H.; Hagfeldt, A.; Lindquist, S.-E. Dye-Sensitized Nanostructured p-Type Nickel Oxide Film as a Photocathode for a Solar Cell. *J. Phys. Chem. B* **1999**, *103* (42), 8940–8943.
- (58) Hu, L.; Peng, J.; Wang, W.; Xia, Z.; Yuan, J.; Lu, J.; Huang, X.; Ma, W.; Song, H.; Chen, W.; Cheng, Y.-B.; Tang, J. Sequential Deposition of CH3NH3PbI3 on Planar NiO Film for Efficient Planar Perovskite Solar Cells. *ACS Photonics* **2014**, *1* (7), 547–553.
- (59) Yu, M.; Natu, G.; Ji, Z.; Wu, Y. P-Type Dye-Sensitized Solar Cells Based on Delafossite CuGaO2 Nanoplates with Saturation Photovoltages Exceeding 460 MV. J. Phys. Chem. Lett. **2012**, 3 (9), 1074–1078.
- (60) Zhang, H.; Wang, H.; Chen, W.; Jen, A. K.-Y. CuGaO2: A Promising Inorganic Hole-Transporting Material for Highly Efficient and Stable Perovskite Solar Cells. *Adv. Mater.* **2017**, 29 (8), 1604984.
- (61) O'Regan, B.; Grätzel, M. A Low-Cost, High-Efficiency Solar Cell Based on Dye-Sensitized Colloidal TiO 2 Films. *Nature* **1991**, 353 (6346), 737–740.
- (62) Lu, L.; Zheng, T.; Wu, Q.; Schneider, A. M.; Zhao, D.; Yu, L. Recent Advances in Bulk Heterojunction Polymer Solar Cells. *Chem. Rev.* **2015**, *115* (23), 12666–12731.

- (63) Basu, K.; Benetti, D.; Zhao, H.; Jin, L.; Vetrone, F.; Vomiero, A.; Rosei, F. Enhanced Photovoltaic Properties in Dye Sensitized Solar Cells by Surface Treatment of SnO<sub>2</sub> Photoanodes. *Sci. Rep.* **2016**, *6*, 23312.
- (64) Hossain, Md. A.; Jennings, J. R.; Koh, Z. Y.; Wang, Q. Carrier Generation and Collection in CdS/CdSe-Sensitized SnO2 Solar Cells Exhibiting Unprecedented Photocurrent Densities. *ACS Nano* **2011**, *5* (4), 3172–3181.
- (65) Bisquert, J.; Garcia-Belmonte, G.; Fabregat-Santiago, F.; Ferriols, N. S.; Bogdanoff, P.; Pereira, E. C. Doubling Exponent Models for the Analysis of Porous Film Electrodes by Impedance. Relaxation of TiO2 Nanoporous in Aqueous Solution. *J. Phys. Chem. B* **2000**, *104* (10), 2287–2298.
- (66) Bisquert, J. Chemical Capacitance of Nanostructured Semi-conductors: Its Origin and Significance for Nanocomposite Solar Cells. *Phys. Chem. Chem. Phys.* **2003**, 5 (24), 5360–5364.
- (67) Fabregat-Santiago, F.; Bisquert, J.; Garcia-Belmonte, G.; Boschloo, G.; Hagfeldt, A. Influence of Electrolyte in Transport and Recombination in Dye-Sensitized Solar Cells Studied by Impedance Spectroscopy. Sol. Energy Mater. Sol. Cells 2005, 87 (1), 117–131.
- (68) Wang, Q.; Moser, J.-E.; Grätzel, M. Electrochemical Impedance Spectroscopic Analysis of Dye-Sensitized Solar Cells. *J. Phys. Chem. B* **2005**, *109* (31), 14945–14953.
- (69) Li, X.; Lin, H.; Li, J.; Li, X.; Cui, B.; Zhang, L. A Numerical Simulation and Impedance Study of the Electron Transport and Recombination in Binder-Free TiO2 Film for Flexible Dye-Sensitized Solar Cells. *J. Phys. Chem. C* **2008**, *112* (35), 13744–13753.
- (70) Kern, R.; Sastrawan, R.; Ferber, J.; Stangl, R.; Luther, J. Modeling and Interpretation of Electrical Impedance Spectra of Dye Solar Cells Operated under Open-Circuit Conditions. *Electrochim. Acta* **2002**, 47 (26), 4213–4225.
- (71) Adachi, M.; Sakamoto, M.; Jiu, J.; Ogata, Y.; Isoda, S. Determination of Parameters of Electron Transport in Dye-Sensitized Solar Cells Using Electrochemical Impedance Spectroscopy. *J. Phys. Chem. B* **2006**, *110* (28), 13872–13880.
- (72) Mora-Seró, I.; Bisquert, J. Fermi Level of Surface States in TiO2 Nanoparticles. *Nano Lett.* **2003**, 3 (7), 945–949.
- (73) He, C.; Zhao, L.; Zheng, Z.; Lu, F. Determination of Electron Diffusion Coefficient and Lifetime in Dye-Sensitized Solar Cells by Electrochemical Impedance Spectroscopy at High Fermi Level Conditions. *J. Phys. Chem. C* 2008, 112 (48), 18730–18733.
- (74) Hsu, C.-P.; Lee, K.-M.; Huang, J. T.-W.; Lin, C.-Y.; Lee, C.-H.; Wang, L.-P.; Tsai, S.-Y.; Ho, K.-C. EIS Analysis on Low Temperature Fabrication of TiO2 Porous Films for Dye-Sensitized Solar Cells. *Electrochim. Acta* **2008**, 53 (25), 7514–7522.
- (75) Gimenez, S.; Dunn, H. K.; Rodenas, P.; Fabregat-Santiago, F.; Miralles, S. G.; Barea, E. M.; Trevisan, R.; Guerrero, A.; Bisquert, J. Carrier Density and Interfacial Kinetics of Mesoporous TiO2 in Aqueous Electrolyte Determined by Impedance Spectroscopy. *J. Electroanal. Chem.* **2012**, *668*, 119–125.
- (76) Park, K.; Zhang, Q.; Myers, D.; Cao, G. Charge Transport Properties in TiO2 Network with Different Particle Sizes for Dye Sensitized Solar Cells. *ACS Appl. Mater. Interfaces* **2013**, *5* (3), 1044–1052.
- (77) Pascoe, A. R.; Bourgeois, L.; Duffy, N. W.; Xiang, W.; Cheng, Y.-B. Surface State Recombination and Passivation in Nanocrystalline TiO2 Dye-Sensitized Solar Cells. *J. Phys. Chem. C* **2013**, *117* (47), 25118–25126.
- (78) Bertoluzzi, L.; Herraiz-Cardona, I.; Gottesman, R.; Zaban, A.; Bisquert, J. Relaxation of Electron Carriers in the Density of States of Nanocrystalline TiO 2. J. Phys. Chem. Lett. 2014, 5 (4), 689–694.
- (79) Park, K.; Zhang, Q.; Xi, J.; Cao, G. Enhanced Charge Transport Properties by Strengthened Necks between TiO2 Aggregates for Dye Sensitized Solar Cells. *Thin Solid Films* **2015**, *588*, 19–25.
- (80) Zhao, K.; Pan, Z.; Zhong, X. Charge Recombination Control for High Efficiency Quantum Dot Sensitized Solar Cells. *J. Phys. Chem. Lett.* **2016**, 7 (3), 406–417.

- (81) Cameron, P. J.; Peter, L. M. Characterization of Titanium Dioxide Blocking Layers in Dye-Sensitized Nanocrystalline Solar Cells. *J. Phys. Chem. B* **2003**, *107* (51), 14394–14400.
- (82) Góes, M. S.; Joanni, E.; Muniz, E. C.; Savu, R.; Habeck, T. R.; Bueno, P. R.; Fabregat-Santiago, F. Impedance Spectroscopy Analysis of the Effect of TiO2 Blocking Layers on the Efficiency of Dye Sensitized Solar Cells. *J. Phys. Chem. C* **2012**, *116* (23), 12415–12421.
- (83) Elbohy, H.; Thapa, A.; Poudel, P.; Adhikary, N.; Venkatesan, S.; Qiao, Q. Vanadium Oxide as New Charge Recombination Blocking Layer for High Efficiency Dye-Sensitized Solar Cells. *Nano Energy* **2015**, *13*, 368–375.
- (84) Park, N.-G.; van de Lagemaat, J.; Frank, A. J. Comparison of Dye-Sensitized Rutile- and Anatase-Based TiO2 Solar Cells. *J. Phys. Chem. B* **2000**, *104* (38), 8989–8994.
- (85) Lancelle-Beltran, E.; Prené, P.; Boscher, C.; Belleville, P.; Buvat, P.; Sanchez, C. All-Solid-State Dye-Sensitized Nanoporous TiO2 Hybrid Solar Cells with High Energy-Conversion Efficiency. *Adv. Mater.* **2006**, *18* (19), 2579–2582.
- (86) Liu, B.; Aydil, E. S. Growth of Oriented Single-Crystalline Rutile TiO2 Nanorods on Transparent Conducting Substrates for Dye-Sensitized Solar Cells. *J. Am. Chem. Soc.* **2009**, *131* (11), 3985–3990
- (87) Kumar, A.; Madaria, A. R.; Zhou, C. Growth of Aligned Single-Crystalline Rutile TiO2 Nanowires on Arbitrary Substrates and Their Application in Dye-Sensitized Solar Cells. *J. Phys. Chem. C* **2010**, *114* (17), 7787–7792.
- (88) Wang, H.; Miyauchi, M.; Ishikawa, Y.; Pyatenko, A.; Koshizaki, N.; Li, Y.; Li, L.; Li, X.; Bando, Y.; Golberg, D. Single-Crystalline Rutile TiO2 Hollow Spheres: Room-Temperature Synthesis, Tailored Visible-Light-Extinction, and Effective Scattering Layer for Quantum Dot-Sensitized Solar Cells. J. Am. Chem. Soc. 2011, 133 (47), 19102—19109.
- (89) Wang, H.; Bai, Y.; Wu, Q.; Zhou, W.; Zhang, H.; Li, J.; Guo, L. Rutile TiO2 Nano-Branched Arrays on FTO for Dye -Sensitized Solar Cells. *Phys. Chem. Chem. Phys.* **2011**, *13* (15), 7008–7013.
- (90) Feng, X.; Zhu, K.; Frank, A. J.; Grimes, C. A.; Mallouk, T. E. Rapid Charge Transport in Dye-Sensitized Solar Cells Made from Vertically Aligned Single-Crystal Rutile TiO2 Nanowires. *Angew. Chem., Int. Ed.* **2012**, *51* (11), 2727–2730.
- (91) Guo, W.; Xu, C.; Wang, X.; Wang, S.; Pan, C.; Lin, C.; Wang, Z. L. Rectangular Bunched Rutile TiO2 Nanorod Arrays Grown on Carbon Fiber for Dye-Sensitized Solar Cells. *J. Am. Chem. Soc.* **2012**, 134 (9), 4437–4441.
- (92) Kogo, A.; Sanehira, Y.; Numata, Y.; Ikegami, M.; Miyasaka, T. Amorphous Metal Oxide Blocking Layers for Highly Efficient Low-Temperature Brookite TiO2-Based Perovskite Solar Cells. ACS Appl. Mater. Interfaces 2018, 10 (3), 2224–2229.
- (93) Shahiduzzaman, Md.; Visal, S.; Kuniyoshi, M.; Kaneko, T.; Umezu, S.; Katsumata, T.; Iwamori, S.; Kakihana, M.; Taima, T.; Isomura, M.; Tomita, K. Low-Temperature-Processed Brookite-Based TiO2 Heterophase Junction Enhances Performance of Planar Perovskite Solar Cells. *Nano Lett.* **2019**, *19* (1), 598–604.
- (94) Dolata, M.; Kedzierzawski, P.; Augustynski, J. Comparative Impedance Spectroscopy Study of Rutile and Anatase Tio2 Film Electrodes. *Electrochim. Acta* **1996**, *41* (7), 1287–1293.
- (95) Weibel, A.; Bouchet, R.; Knauth, P. Electrical Properties and Defect Chemistry of Anatase (TiO2). *Solid State Ionics* **2006**, *177* (3), 229–236.
- (96) Pourjafari, D.; Reyes-Coronado, D.; Vega-Poot, A.; Escalante, R.; Kirkconnell-Reyes, D.; García-Rodríguez, R.; Anta, J. A.; Oskam, G. Brookite-Based Dye-Sensitized Solar Cells: Influence of Morphology and Surface Chemistry on Cell Performance. *J. Phys. Chem. C* **2018**, 122 (26), 14277–14288.
- (97) Kusumawati, Y.; Hosni, M.; Martoprawiro, M. A.; Cassaignon, S.; Pauporté, Th. Charge Transport and Recombination in TiO2 Brookite-Based Photoelectrodes. *J. Phys. Chem. C* **2014**, *118* (41), 23459–23467.

- (98) Kim, H.-S.; Lee, J.-W.; Yantara, N.; Boix, P. P.; Kulkarni, S. A.; Mhaisalkar, S.; Grätzel, M.; Park, N.-G. High Efficiency Solid-State Sensitized Solar Cell-Based on Submicrometer Rutile TiO2 Nanorod and CH3NH3PbI3 Perovskite Sensitizer. *Nano Lett.* **2013**, *13* (6), 2412–2417.
- (99) Hsiao, P.-T.; Tung, Y.-L.; Teng, H. Electron Transport Patterns in TiO2 Nanocrystalline Films of Dye-Sensitized Solar Cells. *J. Phys. Chem. C* **2010**, *114* (14), 6762–6769.
- (100) Magne, C.; Cassaignon, S.; Lancel, G.; Pauporté, T. Brookite TiO2 Nanoparticle Films for Dye-Sensitized Solar Cells. *ChemPhysChem* **2011**, *12* (13), 2461–2467.
- (101) Liao, J.-Y.; He, J.-W.; Xu, H.; Kuang, D.-B.; Su, C.-Y. Effect of TiO2Morphology on Photovoltaic Performance of Dye-Sensitized Solar Cells: Nanoparticles, Nanofibers, Hierarchical Spheres and Ellipsoid Spheres. *J. Mater. Chem.* **2012**, 22 (16), 7910–7918.
- (102) Lee, K.; Mazare, A.; Schmuki, P. One-Dimensional Titanium Dioxide Nanomaterials: Nanotubes. *Chem. Rev.* **2014**, *114* (19), 9385–9454.
- (103) Abayev, I.; Zaban, A.; Fabregat-Santiago, F.; Bisquert, J. Electronic Conductivity in Nanostructured TiO2 Films Permeated with Electrolyte. *Phys. Status Solidi A* **2003**, *196* (1), R4–R6.
- (104) van de Lagemaat, J.; Park, N.-G.; Frank, A. J. Influence of Electrical Potential Distribution, Charge Transport, and Recombination on the Photopotential and Photocurrent Conversion Efficiency of Dye-Sensitized Nanocrystalline TiO2 Solar Cells: A Study by Electrical Impedance and Optical Modulation Techniques. *J. Phys. Chem. B* **2000**, *104* (9), 2044–2052.
- (105) Frank, A. J.; Kopidakis, N.; van de Lagemaat, J. Electrons in Nanostructured TiO2 Solar Cells: Transport, Recombination and Photovoltaic Properties. *Coord. Chem. Rev.* **2004**, 248 (13), 1165–1179.
- (106) Peter, L. M. Characterization and Modeling of Dye-Sensitized Solar Cells. J. Phys. Chem. C 2007, 111 (18), 6601–6612.
- (107) Fabregat-Santiago, F.; Bisquert, J.; Cevey, L.; Chen, P.; Wang, M.; Zakeeruddin, S. M.; Grätzel, M. Electron Transport and Recombination in Solid-State Dye Solar Cell with Spiro-OMeTAD as Hole Conductor. *J. Am. Chem. Soc.* **2009**, *131* (2), 558–562.
- (108) Shin, I.; Seo, H.; Son, M.-K.; Kim, J.-K.; Prabakar, K.; Kim, H.-J. Analysis of TiO2 Thickness Effect on Characteristic of a Dye-Sensitized Solar Cell by Using Electrochemical Impedance Spectroscopy. *Curr. Appl. Phys.* **2010**, *10* (3), S422–S424.
- (109) Muniz, E. C.; Góes, M. S.; Silva, J. J.; Varela, J. A.; Joanni, E.; Parra, R.; Bueno, P. R. Synthesis and Characterization of Mesoporous TiO2 Nanostructured Films Prepared by a Modified Sol—Gel Method for Application in Dye Solar Cells. *Ceram. Int.* **2011**, *37* (3), 1017—1024.
- (110) Boix, P. P.; Lee, Y. H.; Fabregat-Santiago, F.; Im, S. H.; Mora-Sero, I.; Bisquert, J.; Seok, S. I. From Flat to Nanostructured Photovoltaics: Balance between Thickness of the Absorber and Charge Screening in Sensitized Solar Cells. *ACS Nano* **2012**, *6* (1), 873–880.
- (111) Li, X.; Dai, S.-M.; Zhu, P.; Deng, L.-L.; Xie, S.-Y.; Cui, Q.; Chen, H.; Wang, N.; Lin, H. Efficient Perovskite Solar Cells Depending on TiO2 Nanorod Arrays. ACS Appl. Mater. Interfaces 2016, 8 (33), 21358–21365.
- (112) Fabregat-Santiago, F.; Barea, E. M.; Bisquert, J.; Mor, G. K.; Shankar, K.; Grimes, C. A. High Carrier Density and Capacitance in TiO2 Nanotube Arrays Induced by Electrochemical Doping. *J. Am. Chem. Soc.* **2008**, 130 (34), 11312–11316.
- (113) Taveira, L. V.; Sagüés, A. A.; Macak, J. M.; Schmuki, P. Impedance Behavior of TiO2 Nanotubes Formed by Anodization in NaF Electrolytes. *J. Electrochem. Soc.* **2008**, *155* (6), C293–C302.
- (114) Jose, R.; Thavasi, V.; Ramakrishna, S. Metal Oxides for Dye-Sensitized Solar Cells. J. Am. Ceram. Soc. 2009, 92 (2), 289–301.
- (115) Spagnol, V.; Sutter, E.; Debiemme-Chouvy, C.; Cachet, H.; Baroux, B. EIS Study of Photo-Induced Modifications of Nano-Columnar TiO2 Films. *Electrochim. Acta* **2009**, *54* (4), 1228–1232.
- (116) Pu, P.; Cachet, H.; Sutter, E. M. M. Electrochemical Impedance Spectroscopy to Study Photo Induced Effects on Self-

- Organized TiO2 Nanotube Arrays. Electrochim. Acta 2010, 55 (20), 5938-5946.
- (117) Zhong, P.; Que, W.; Zhang, J.; Jia, Q.; Wang, W.; Liao, Y.; Hu, X. Charge Transport and Recombination in Dye-Sensitized Solar Cells Based on Hybrid Films of TiO2 Particles/TiO2 Nanotubes. *J. Alloys Compd.* **2011**, *509* (29), 7808–7813.
- (118) Ping Wu, H.; Lin Li, L.; Chon Chen, C.; Guang Diau, E. W. Anodic TiO2 Nanotube Arrays for Dye-Sensitized Solar Cells Characterized by Electrochemical Impedance Spectroscopy. *Ceram. Int.* **2012**, 38 (8), 6253–6266.
- (119) Kapilashrami, M.; Zhang, Y.; Liu, Y.-S.; Hagfeldt, A.; Guo, J. Probing the Optical Property and Electronic Structure of TiO2 Nanomaterials for Renewable Energy Applications. *Chem. Rev.* **2014**, *114* (19), 9662–9707.
- (120) Zhang, Q.; Celorrio, V.; Bradley, K.; Eisner, F.; Cherns, D.; Yan, W.; Fermín, D. J. Density of Deep Trap States in Oriented TiO2 Nanotube Arrays. *J. Phys. Chem. C* **2014**, *118* (31), 18207–18213.
- (121) Sudhagar, P.; Jung, J. H.; Park, S.; Sathyamoorthy, R.; Ahn, H.; Kang, Y. S. Self-Assembled CdS Quantum Dots-Sensitized TiO2 Nanospheroidal Solar Cells: Structural and Charge Transport Analysis. *Electrochim. Acta* **2009**, *55* (1), 113–117.
- (122) Kim, Y. J.; Lee, M. H.; Kim, H. J.; Lim, G.; Choi, Y. S.; Park, N.-G.; Kim, K.; Lee, W. I. Formation of Highly Efficient Dye-Sensitized Solar Cells by Hierarchical Pore Generation with Nanoporous TiO2 Spheres. *Adv. Mater.* **2009**, *21* (36), 3668–3673. (123) Kim, C. W.; Choi, M. J.; Lee, S.; Park, H.; Moon, B.; Kang, Y. S.; Kang, Y. S. Crystalline Matrix of Mesoporous TiO2 Framework for Dye-Sensitized Solar Cell Application. *J. Phys. Chem. C* **2015**, *119* (44), 24902–24909.
- (124) Berglund, S. P.; Hoang, S.; Minter, R. L.; Fullon, R. R.; Mullins, C. B. Investigation of 35 Elements as Single Metal Oxides, Mixed Metal Oxides, or Dopants for Titanium Dioxide for Dye-Sensitized Solar Cells. *J. Phys. Chem. C* **2013**, 117 (48), 25248–25258
- (125) Archana, P. S.; Jose, R.; Yusoff, M. M.; Ramakrishna, S. Near Band-Edge Electron Diffusion in Electrospun Nb-Doped Anatase TiO2 Nanofibers Probed by Electrochemical Impedance Spectroscopy. *Appl. Phys. Lett.* **2011**, *98* (15), 152106.
- (126) Zhang, J.; Peng, W.; Chen, Z.; Chen, H.; Han, L. Effect of Cerium Doping in the TiO2 Photoanode on the Electron Transport of Dye-Sensitized Solar Cells. *J. Phys. Chem. C* **2012**, *116* (36), 19182–19190.
- (127) Ghosh, R.; Hara, Y.; Alibabaei, L.; Hanson, K.; Rangan, S.; Bartynski, R.; Meyer, T. J.; Lopez, R. Increasing Photocurrents in Dye Sensitized Solar Cells with Tantalum-Doped Titanium Oxide Photoanodes Obtained by Laser Ablation. *ACS Appl. Mater. Interfaces* **2012**, *4* (9), 4566–4570.
- (128) Dorman, J. A.; Weickert, J.; Reindl, J. B.; Putnik, M.; Wisnet, A.; Noebels, M.; Scheu, C.; Schmidt-Mende, L. Control of Recombination Pathways in TiO2 Nanowire Hybrid Solar Cells Using Sn4+ Dopants. *J. Phys. Chem. C* 2014, 118 (30), 16672–16679. (129) Guerrero, A.; Garcia-Belmonte, G.; Mora-Sero, I.; Bisquert, J.;
- Kang, Y. S.; Jacobsson, T. J.; Correa-Baena, J.-P.; Hagfeldt, A. Properties of Contact and Bulk Impedances in Hybrid Lead Halide Perovskite Solar Cells Including Inductive Loop Elements. *J. Phys. Chem. C* **2016**, *120* (15), 8023–8032.
- (130) Kim, H.-S.; Jang, I.-H.; Ahn, N.; Choi, M.; Guerrero, A.; Bisquert, J.; Park, N.-G. Control of I–V Hysteresis in CH3NH3PbI3 Perovskite Solar Cell. *J. Phys. Chem. Lett.* **2015**, *6* (22), 4633–4639.
- (131) Redmond, G.; Fitzmaurice, D.; Graetzel, M. Visible Light Sensitization by Cis-Bis(Thiocyanato)Bis(2,2'-Bipyridyl-4,4'-Dicarboxylato)Ruthenium(II) of a Transparent Nanocrystalline ZnO Film Prepared by Sol-Gel Techniques. *Chem. Mater.* **1994**, 6 (5), 686–691.
- (132) Rensmo, H.; Keis, K.; Lindström, H.; Södergren, S.; Solbrand, A.; Hagfeldt, A.; Lindquist, S.-E.; Wang, L. N.; Muhammed, M. High Light-to-Energy Conversion Efficiencies for Solar Cells Based on Nanostructured ZnO Electrodes. *J. Phys. Chem. B* **1997**, *101* (14), 2598–2601.

- (133) Quintana, M.; Edvinsson, T.; Hagfeldt, A.; Boschloo, G. Comparison of Dye-Sensitized ZnO and TiO2 Solar Cells: Studies of Charge Transport and Carrier Lifetime. *J. Phys. Chem. C* **2007**, *111* (2), 1035–1041.
- (134) Mani, A.; Huisman, C.; Goossens, A.; Schoonman, J. Mott–Schottky Analysis and Impedance Spectroscopy of TiO2/6T and ZnO/6T Devices. J. Phys. Chem. B 2008, 112 (33), 10086–10091.
- (135) Chandiran, A. K.; Abdi-Jalebi, M.; Nazeeruddin, M. K.; Grätzel, M. Analysis of Electron Transfer Properties of ZnO and TiO2 Photoanodes for Dye-Sensitized Solar Cells. *ACS Nano* **2014**, 8 (3), 2261–2268.
- (136) Wang, Z. L. Nanostructures of Zinc Oxide. *Mater. Today* **2004**, 7 (6), 26-33.
- (137) Djurišić, A. B.; Chen, X.; Leung, Y. H.; Ng, A. M. C. ZnO Nanostructures: Growth, Properties and Applications. *J. Mater. Chem.* **2012**. 22 (14), 6526–6535.
- (138) Guillén, E.; Peter, L. M.; Anta, J. A. Electron Transport and Recombination in ZnO-Based Dye-Sensitized Solar Cells. *J. Phys. Chem. C* 2011, 115 (45), 22622–22632.
- (139) Mora-Seró, I.; Fabregat-Santiago, F.; Denier, B.; Bisquert, J.; Tena-Zaera, R.; Elias, J.; Lévy-Clément, C. Determination of Carrier Density of ZnO Nanowires by Electrochemical Techniques. *Appl. Phys. Lett.* **2006**, 89 (20), 203117.
- (140) Tena-Zaera, R.; Elias, J.; Lévy-Clément, C.; Mora-Seró, I.; Luo, Y.; Bisquert, J. Electrodeposition and Impedance Spectroscopy Characterization of ZnO Nanowire Arrays. *Phys. Status Solidi A* **2008**, 205 (10), 2345–2350.
- (141) Martinson, A. B. F.; Góes, M. S.; Fabregat-Santiago, F.; Bisquert, J.; Pellin, M. J.; Hupp, J. T. Electron Transport in Dye-Sensitized Solar Cells Based on ZnO Nanotubes: Evidence for Highly Efficient Charge Collection and Exceptionally Rapid Dynamics. J. Phys. Chem. A 2009, 113 (16), 4015–4021.
- (142) He, C.; Zheng, Z.; Tang, H.; Zhao, L.; Lu, F. Electrochemical Impedance Spectroscopy Characterization of Electron Transport and Recombination in ZnO Nanorod Dye-Sensitized Solar Cells. *J. Phys. Chem. C* 2009, *113* (24), 10322–10325.
- (143) Ku, C.-H.; Wu, J.-J. Electron Transport Properties in ZnO Nanowire Array/Nanoparticle Composite Dye-Sensitized Solar Cells. *Appl. Phys. Lett.* **2007**, *91* (9), 093117.
- (144) Parthasarathy, M.; Ramgir, N. S.; Sathe, B. R.; Mulla, I. S.; Pillai, V. K. Surface-State-Mediated Electron Transfer at Nanostructured ZnO Multipod/Electrolyte Interfaces. *J. Phys. Chem. C* **2007**, *111* (35), 13092–13102.
- (145) Liu, H.; Piret, G.; Sieber, B.; Laureyns, J.; Roussel, P.; Xu, W.; Boukherroub, R.; Szunerits, S. Electrochemical Impedance Spectroscopy of ZnO Nanostructures. *Electrochem. Commun.* **2009**, *11* (5), 945–949.
- (146) Dupuy, L.; Haller, S.; Rousset, J.; Donsanti, F.; Guillemoles, J.-F.; Lincot, D.; Decker, F. Impedance Measurements of Nanoporosity in Electrodeposited ZnO Films for DSSC. *Electrochem. Commun.* **2010**, *12* (5), 697–699.
- (147) Lai, Y.-H.; Lin, C.-Y.; Chen, H.-W.; Chen, J.-G.; Kung, C.-W.; Vittal, R.; Ho, K.-C. Fabrication of a ZnO Film with a Mosaic Structure for a High Efficient Dye -Sensitized Solar Cell. *J. Mater. Chem.* **2010**, 20 (42), 9379–9385.
- (148) Lu, L.; Li, R.; Fan, K.; Peng, T. Effects of Annealing Conditions on the Photoelectrochemical Properties of Dye-Sensitized Solar Cells Made with ZnO Nanoparticles. *Sol. Energy* **2010**, *84* (5), 844–853.
- (149) Sudhagar, P.; Kumar, R. S.; Jung, J. H.; Cho, W.; Sathyamoorthy, R.; Won, J.; Kang, Y. S. Facile Synthesis of Highly Branched Jacks-like ZnO Nanorods and Their Applications in Dye-Sensitized Solar Cells. *Mater. Res. Bull.* **2011**, 46 (9), 1473–1479.
- (150) Puyoo, E.; Rey, G.; Appert, E.; Consonni, V.; Bellet, D. Efficient Dye-Sensitized Solar Cells Made from ZnO Nanostructure Composites. J. Phys. Chem. C 2012, 116 (34), 18117–18123.
- (151) Sacco, A.; Lamberti, A.; Gazia, R.; Bianco, S.; Manfredi, D.; Shahzad, N.; Cappelluti, F.; Ma, S.; Tresso, E. High Efficiency Dye

- -Sensitized Solar Cells Exploiting Sponge-like ZnO Nanostructures. *Phys. Chem. Chem. Phys.* **2012**, *14* (47), 16203–16208.
- (152) Magne, C.; Moehl, T.; Urien, M.; Grätzel, M.; Pauporté, T. Effects of ZnO Film Growth Route and Nanostructure on Electron Transport and Recombination in Dye -Sensitized Solar Cells. *J. Mater. Chem. A* 2013, *1* (6), 2079–2088.
- (153) Park, K.; Xi, J.; Zhang, Q.; Cao, G. Charge Transport Properties of ZnO Nanorod Aggregate Photoelectrodes for DSCs. *J. Phys. Chem. C* **2011**, *115* (43), 20992–20999.
- (154) Hosni, M.; Kusumawati, Y.; Farhat, S.; Jouini, N.; Pauporté, Th. Effects of Oxide Nanoparticle Size and Shape on Electronic Structure, Charge Transport, and Recombination in Dye-Sensitized Solar Cell Photoelectrodes. *J. Phys. Chem. C* **2014**, *118* (30), 16791–16798.
- (155) Wu, J.-J.; Wong, D. K.-P. Fabrication and Impedance Analysis of N-ZnO Nanorod/p-Si Heterojunctions to Investigate Carrier Concentrations in Zn/O Source- Ratio-Tuned ZnO Nanorod Arrays. *Adv. Mater.* **2007**, *19* (15), 2015–2019.
- (156) Lee, S.-H.; Han, S.-H.; Jung, H. S.; Shin, H.; Lee, J.; Noh, J.-H.; Lee, S.; Cho, I.-S.; Lee, J.-K.; Kim, J.; Shin, H. Al-Doped ZnO Thin Film: A New Transparent Conducting Layer for ZnO Nanowire-Based Dye-Sensitized Solar Cells. *J. Phys. Chem. C* **2010**, *114* (15), 7185–7189.
- (157) Wong, K. K.; Ng, A.; Chen, X. Y.; Ng, Y. H.; Leung, Y. H.; Ho, K. H.; Djurišić, A. B.; Ng, A. M. C.; Chan, W. K.; Yu, L.; Phillips, D. L. Effect of ZnO Nanoparticle Properties on Dye-Sensitized Solar Cell Performance. ACS Appl. Mater. Interfaces 2012, 4 (3), 1254–1261.
- (158) Arshad, M.; Ahmed, A. S.; Azam, A.; Naqvi, A. H. Exploring the Dielectric Behavior of Co Doped ZnO Nanoparticles Synthesized by Wet Chemical Route Using Impedance Spectroscopy. *J. Alloys Compd.* **2013**, *577*, 469–474.
- (159) Raj, C. J.; Prabakar, K.; Karthick, S. N.; Hemalatha, K. V.; Son, M.-K.; Kim, H.-J. Banyan Root Structured Mg-Doped ZnO Photoanode Dye-Sensitized Solar Cells. *J. Phys. Chem. C* **2013**, *117* (6), 2600–2607.
- (160) Shinde, S. S.; Korade, A. P.; Bhosale, C. H.; Rajpure, K. Y. Influence of Tin Doping onto Structural, Morphological, Optoelectronic and Impedance Properties of Sprayed ZnO Thin Films. *J. Alloys Compd.* **2013**, *551*, 688–693.
- (161) Das, P. P.; Agarkar, S. A.; Mukhopadhyay, S.; Manju, U.; Ogale, S. B.; Devi, P. S. Defects in Chemically Synthesized and Thermally Processed ZnO Nanorods: Implications for Active Layer Properties in Dye-Sensitized Solar Cells. *Inorg. Chem.* **2014**, 53 (8), 3961–3972.
- (162) Cheng, W.-H.; Chiou, J.-W.; Tsai, M.-Y.; Jeng, J.-S.; Chen, J.-S.; Hsu, S. L.-C.; Chou, W.-Y. Lithium-Induced Defect Levels in ZnO Nanoparticles To Facilitate Electron Transport in Inverted Organic Photovoltaics. *J. Phys. Chem. C* **2016**, *120* (28), 15035–15041.
- (163) Mahmud, M. A.; Elumalai, N. K.; Upama, M. B.; Wang, D.; Soufiani, A. M.; Wright, M.; Xu, C.; Haque, F.; Uddin, A. Solution-Processed Lithium-Doped ZnO Electron Transport Layer for Efficient Triple Cation (Rb, MA, FA) Perovskite Solar Cells. ACS Appl. Mater. Interfaces 2017, 9 (39), 33841–33854.
- (164) Krishnapriya, R.; Praneetha, S.; Kannan, S.; Vadivel Murugan, A. Unveiling the Co2+ Ion Doping-Induced Hierarchical Shape Evolution of ZnO: In Correlation with Magnetic and Photovoltaic Performance. ACS Sustainable Chem. Eng. 2017, 5 (11), 9981–9992.
- (165) Kay, A.; Grätzel, M. Dye-Sensitized Core—Shell Nanocrystals: Improved Efficiency of Mesoporous Tin Oxide Electrodes Coated with a Thin Layer of an Insulating Oxide. *Chem. Mater.* **2002**, *14* (7), 2930–2935.
- (166) Green, A. N. M.; Palomares, E.; Haque, S. A.; Kroon, J. M.; Durrant, J. R. Charge Transport versus Recombination in Dye-Sensitized Solar Cells Employing Nanocrystalline TiO2 and SnO2 Films. J. Phys. Chem. B 2005, 109 (25), 12525–12533.
- (167) Kim, J.-Y.; Kim, J. Y.; Lee, D.-K.; Kim, B.; Kim, H.; Ko, M. J. Importance of 4-Tert-Butylpyridine in Electrolyte for Dye-Sensitized Solar Cells Employing SnO2 Electrode. *J. Phys. Chem. C* **2012**, *116* (43), 22759–22766.

- (168) Ulfa, M.; Wang, P.; Zhang, J.; Liu, J.; de Marcillac, W. D.; Coolen, L.; Peralta, S.; Pauporté, T. Charge Injection and Electrical Response in Low-Temperature SnO2-Based Efficient Perovskite Solar Cells. ACS Appl. Mater. Interfaces 2018, 10 (41), 35118–35128.
- (169) Xiao, J.; Huang, Q.; Xu, J.; Li, C.; Chen, G.; Luo, Y.; Li, D.; Meng, Q. CdS/CdSe Co-Sensitized Solar Cells Based on a New SnO2 Photoanode with a Three-Dimensionally Interconnected Ordered Porous Structure. *J. Phys. Chem. C* **2014**, *118* (8), 4007–4015.
- (170) Huang, Q.; Li, F.; Gong, Y.; Luo, J.; Yang, S.; Luo, Y.; Li, D.; Bai, X.; Meng, Q. Recombination in SnO2-Based Quantum Dots Sensitized Solar Cells: The Role of Surface States. *J. Phys. Chem. C* **2013**, *117* (21), 10965–10973.
- (171) Elumalai, N. K.; Jose, R.; Archana, P. S.; Chellappan, V.; Ramakrishna, S. Charge Transport through Electrospun SnO2 Nanoflowers and Nanofibers: Role of Surface Trap Density on Electron Transport Dynamics. *J. Phys. Chem.* C **2012**, *116* (42), 22112–22120.
- (172) Kumar, E. N.; Jose, R.; Archana, P. S.; Vijila, C.; Yusoff, M. M.; Ramakrishna, S. High Performance Dye -Sensitized Solar Cells with Record Open Circuit Voltage Using Tin Oxide Nanoflowers Developed by Electrospinning. *Energy Environ. Sci.* **2012**, *5* (1), 5401–5407.
- (173) Wijeratne, K.; Akilavasan, J.; Thelakkat, M.; Bandara, J. Enhancing the Solar Cell Efficiency through Pristine 1-Dimentional SnO2 Nanostructures: Comparison of Charge Transport and Carrier Lifetime of SnO2 Particles vs. Nanorods. *Electrochim. Acta* **2012**, 72, 192–198.
- (174) Sigdel, S.; Elbohy, H.; Gong, J.; Adhikari, N.; Sumathy, K.; Qiao, H.; Wei, Q.; Sayyad, M. H.; Zai, J.; Qian, X.; Qiao, Q. Dye-Sensitized Solar Cells Based on Porous Hollow Tin Oxide Nanofibers. *IEEE Trans. Electron Devices* **2015**, *62* (6), 2027–2032.
- (175) Wang, D.; Liu, S.; Shao, M.; Li, Q.; Gu, Y.; Zhao, J.; Zhang, X.; Zhao, J.; Fang, Y. Aqueous Solution-Processed Multifunctional SnO2 Aggregates for Highly Efficient Dye-Sensitized Solar Cells. *Ind. Eng. Chem. Res.* **2018**, *57* (21), 7136–7145.
- (176) Dou, X.; Sabba, D.; Mathews, N.; Wong, L. H.; Lam, Y. M.; Mhaisalkar, S. Hydrothermal Synthesis of High Electron Mobility Zn-Doped SnO2 Nanoflowers as Photoanode Material for Efficient Dye-Sensitized Solar Cells. *Chem. Mater.* **2011**, 23 (17), 3938–3945.
- (177) Azam, A.; Ahmed, A. S.; Chaman, M.; Naqvi, A. H. Investigation of Electrical Properties of Mn Doped Tin Oxide Nanoparticles Using Impedance Spectroscopy. *J. Appl. Phys.* **2010**, 108 (9), 094329.
- (178) Teh, J. J.; Ting, S. L.; Leong, K. C.; Li, J.; Chen, P. Gallium-Doped Tin Oxide Nano-Cuboids for Improved Dye Sensitized Solar Cell. ACS Appl. Mater. Interfaces 2013, 5 (21), 11377–11382.
- (179) Shalan, A. E.; Rasly, M.; Osama, I.; Rashad, M. M.; Ibrahim, I. A. Photocurrent Enhancement by Ni2+ and Zn2+ Ion Doped in SnO2 Nanoparticles in Highly Porous Dye-Sensitized Solar Cells. *Ceram. Int.* **2014**, *40* (8, Part A), 11619–11626.
- (180) Jim, W. Y.; Liu, X.; Yiu, W. K.; Leung, Y. H.; Djurišić, A. B.; Chan, W. K.; Liao, C.; Shih, K.; Surya, C. The Effect of Different Dopants on the Performance of SnO2-Based Dye-Sensitized Solar Cells. *Phys. Status Solidi B* **2015**, 252 (3), 553–557.
- (181) Ben Haj Othmen, W.; Sdiri, N.; Elhouichet, H.; Férid, M. Study of Charge Transport in Fe-Doped SnO2 Nanoparticles Prepared by Hydrothermal Method. *Mater. Sci. Semicond. Process.* **2016**, *52*, 46–54.
- (182) Fabregat-Santiago, F.; Garcia-Belmonte, G.; Mora-Seró, I.; Bisquert, J. Characterization of Nanostructured Hybrid and Organic Solar Cells by Impedance Spectroscopy. *Phys. Chem. Chem. Phys.* **2011**, *13* (20), 9083–9118.
- (183) Hautier, G.; Miglio, A.; Ceder, G.; Rignanese, G.-M.; Gonze, X. Identification and Design Principles of Low Hole Effective Mass *p*-Type Transparent Conducting Oxides. *Nat. Commun.* **2013**, *4*, 2292. (184) Xia, X. H.; Tu, J. P.; Zhang, J.; Wang, X. L.; Zhang, W. K.; Huang, H. Morphology Effect on the Electrochromic and Electrochemical Performances of NiO Thin Films. *Electrochim. Acta* **2008**, *53* (18), 5721–5724.

- (185) Huang, Z.; Natu, G.; Ji, Z.; Hasin, P.; Wu, Y. P-Type Dye-Sensitized NiO Solar Cells: A Study by Electrochemical Impedance Spectroscopy. *J. Phys. Chem. C* **2011**, *115* (50), 25109–25114.
- (186) Yang, H.; Guai, G. H.; Guo, C.; Song, Q.; Jiang, S. P.; Wang, Y.; Zhang, W.; Li, C. M. NiO/Graphene Composite for Enhanced Charge Separation and Collection in p-Type Dye Sensitized Solar Cell. *J. Phys. Chem. C* **2011**, *115* (24), 12209–12215.
- (187) Feihl, S.; Costa, R. D.; Pflock, S.; Schmidt, C.; Schönamsgruber, J.; Backes, S.; Hirsch, A.; Guldi, D. M. Nickel Oxide Nanostructured Electrodes towards Perylenediimide-Based Dye -Sensitized Solar Cells. *RSC Adv.* **2012**, 2 (30), 11495–11503.
- (188) Hsu, C.-Y.; Chen, W.-T.; Chen, Y.-C.; Wei, H.-Y.; Yen, Y.-S.; Huang, K.-C.; Ho, K.-C.; Chu, C.-W.; Lin, J. T. Charge Transporting Enhancement of NiO Photocathodes for P-Type Dye-Sensitized Solar Cells. *Electrochim. Acta* **2012**, *66*, 210–215.
- (189) Huang, Z.; Natu, G.; Ji, Z.; He, M.; Yu, M.; Wu, Y. Probing the Low Fill Factor of NiO P-Type Dye-Sensitized Solar Cells. *J. Phys. Chem. C* **2012**, *116* (50), 26239–26246.
- (190) Barceló, I.; Guillén, E.; Lana-Villarreal, T.; Gómez, R. Preparation and Characterization of Nickel Oxide Photocathodes Sensitized with Colloidal Cadmium Selenide Quantum Dots. *J. Phys. Chem. C* **2013**, *117* (44), 22509–22517.
- (191) Hod, I.; Tachan, Z.; Shalom, M.; Zaban, A. Characterization and Control of the Electronic Properties of a NiO Based Dye Sensitized Photocathode. *Phys. Chem. Chem. Phys.* **2013**, *15* (17), 6339–6343.
- (192) Peiris, T. A. N.; Sagu, J. S.; Wijayantha, K. G. U.; García-Cañadas, J. Electrochemical Determination of the Density of States of Nanostructured NiO Films. *ACS Appl. Mater. Interfaces* **2014**, *6* (17), 14988–14993.
- (193) Kang, J. S.; Kim, J.; Kim, J. S.; Nam, K.; Jo, H.; Son, Y. J.; Kang, J.; Jeong, J.; Choe, H.; Kwon, T.-H.; Sung, Y.-E. Electrochemically Synthesized Mesoscopic Nickel Oxide Films as Photocathodes for Dye-Sensitized Solar Cells. *ACS Appl. Energy Mater.* **2018**, *1* (8), 4178–4185.
- (194) Guai, G. H.; Leiw, M. Y.; Ng, C. M.; Li, C. M. Sulfur-Doped Nickel Oxide Thin Film as an Alternative to Pt for Dye-Sensitized Solar Cell Counter Electrodes. *Adv. Energy Mater.* **2012**, *2* (3), 334–338.
- (195) Natu, G.; Hasin, P.; Huang, Z.; Ji, Z.; He, M.; Wu, Y. Valence Band-Edge Engineering of Nickel Oxide Nanoparticles via Cobalt Doping for Application in p-Type Dye-Sensitized Solar Cells. *ACS Appl. Mater. Interfaces* **2012**, *4* (11), 5922–5929.
- (196) D'Amario, L.; Boschloo, G.; Hagfeldt, A.; Hammarström, L. Tuning of Conductivity and Density of States of NiO Mesoporous Films Used in P-Type DSSCs. J. Phys. Chem. C 2014, 118 (34), 19556—19564.
- (197) Jung, J. W.; Chueh, C.-C.; Jen, A. K.-Y. A Low-Temperature, Solution-Processable, Cu-Doped Nickel Oxide Hole-Transporting Layer via the Combustion Method for High-Performance Thin-Film Perovskite Solar Cells. *Adv. Mater.* **2015**, *27* (47), 7874–7880.
- (198) Kawazoe, H.; Yasukawa, M.; Hyodo, H.; Kurita, M.; Yanagi, H.; Hosono, H. P-Type Electrical Conduction in Transparent Thin Films of CuAlO<sub>2</sub>. *Nature* **1997**, 389 (6654), 939–942.
- (199) Renaud, A.; Chavillon, B.; Le Pleux, L.; Pellegrin, Y.; Blart, E.; Boujtita, M.; Pauporté, T.; Cario, L.; Jobic, S.; Odobel, F. CuGaO2: A Promising Alternative for NiO in p-Type Dye Solar Cells. *J. Mater. Chem.* **2012**, 22 (29), 14353–14356.
- (200) Li, D.; Zhou, J.; Chen, X.; Song, H. Amorphous Fe2O3/Graphene Composite Nanosheets with Enhanced Electrochemical Performance for Sodium-Ion Battery. ACS Appl. Mater. Interfaces 2016, 8 (45), 30899–30907.
- (201) Zhu, J.; Sharma, Y. K.; Zeng, Z.; Zhang, X.; Srinivasan, M.; Mhaisalkar, S.; Zhang, H.; Hng, H. H.; Yan, Q. Cobalt Oxide Nanowall Arrays on Reduced Graphene Oxide Sheets with Controlled Phase, Grain Size, and Porosity for Li-Ion Battery Electrodes. *J. Phys. Chem. C* 2011, 115 (16), 8400–8406.
- (202) Wang, X.; Han, X.; Lim, M.; Singh, N.; Gan, C. L.; Jan, M.; Lee, P. S. Nickel Cobalt Oxide-Single Wall Carbon Nanotube

- Composite Material for Superior Cycling Stability and High-Performance Supercapacitor Application. *J. Phys. Chem. C* **2012**, 116 (23), 12448–12454.
- (203) Kwon, Y. H.; Minnici, K.; Huie, M. M.; Takeuchi, K. J.; Takeuchi, E. S.; Marschilok, A. C.; Reichmanis, E. Electron/Ion Transport Enhancer in High Capacity Li-Ion Battery Anodes. *Chem. Mater.* **2016**, 28 (18), 6689–6697.
- (204) Thangadurai, V.; Pinzaru, D.; Narayanan, S.; Baral, A. K. Fast Solid-State Li Ion Conducting Garnet-Type Structure Metal Oxides for Energy Storage. *J. Phys. Chem. Lett.* **2015**, *6* (2), 292–299.
- (205) Zhu, H.; Lee, K. T.; Hitz, G. T.; Han, X.; Li, Y.; Wan, J.; Lacey, S.; von Wald Cresce, A.; Xu, K.; Wachsman, E.; Hu, L. Free-Standing Na2/3Fe1/2Mn1/2O2@Graphene Film for a Sodium-Ion Battery Cathode. ACS Appl. Mater. Interfaces 2014, 6 (6), 4242–4247.
- (206) Bhaway, S. M.; Chen, Y.-M.; Guo, Y.; Tangvijitsakul, P.; Soucek, M. D.; Cakmak, M.; Zhu, Y.; Vogt, B. D. Hierarchical Electrospun and Cooperatively Assembled Nanoporous Ni/NiO/MnOx/Carbon Nanofiber Composites for Lithium Ion Battery Anodes. ACS Appl. Mater. Interfaces 2016, 8 (30), 19484–19493.
- (207) Jeong, G. H.; Bae, H.-B.; Choi, D.; Kim, Y. H.; Yoon, S.; Kim, S.-W. Highly Stable Metal Mono-Oxide Alloy Nanoparticles and Their Potential as Anode Materials for Li-Ion Battery. *J. Phys. Chem. C* **2012**. *116* (45). 23851–23857.
- (208) Di Lecce, D.; Campanella, D.; Hassoun, J. Insight on the Enhanced Reversibility of a Multimetal Layered Oxide for Sodium-Ion Battery. J. Phys. Chem. C 2018, 122 (42), 23925–23933.
- (209) Kumar Sen, U.; Shaligram, A.; Mitra, S. Intercalation Anode Material for Lithium Ion Battery Based on Molybdenum Dioxide. *ACS Appl. Mater. Interfaces* **2014**, *6* (16), 14311–14319.
- (210) Rock, S. E.; Wu, L.; Crain, D. J.; Krishnan, S.; Roy, D. Interfacial Characteristics of a PEGylated Imidazolium Bistriflamide Ionic Liquid Electrolyte at a Lithium Ion Battery Cathode of LiMn2O4. ACS Appl. Mater. Interfaces 2013, 5 (6), 2075–2084.
- (211) Qian, D.; Xu, B.; Cho, H.-M.; Hatsukade, T.; Carroll, K. J.; Meng, Y. S. Lithium Lanthanum Titanium Oxides: A Fast Ionic Conductive Coating for Lithium-Ion Battery Cathodes. *Chem. Mater.* **2012**, *24* (14), 2744–2751.
- (212) Zhang, L.; Pu, J.; Jiang, Y.; Shen, Z.; Li, J.; Liu, J.; Ma, H.; Niu, J.; Zhang, H. Low Interface Energies Tune the Electrochemical Reversibility of Tin Oxide Composite Nanoframes as Lithium-Ion Battery Anodes. ACS Appl. Mater. Interfaces 2018, 10 (43), 36892—36901.
- (213) Butala, M. M.; Danks, K. R.; Lumley, M. A.; Zhou, S.; Melot, B. C.; Seshadri, R. MnO Conversion in Li-Ion Batteries: In Situ Studies and the Role of Mesostructuring. ACS Appl. Mater. Interfaces **2016**, 8 (10), 6496–6503.
- (214) Bucher, N.; Hartung, S.; Franklin, J. B.; Wise, A. M.; Lim, L. Y.; Chen, H.-Y.; Weker, J. N.; Toney, M. F.; Srinivasan, M. P2—NaxCoyMn1—YO2 (y = 0, 0.1) as Cathode Materials in Sodium-Ion Batteries—Effects of Doping and Morphology To Enhance Cycling Stability. *Chem. Mater.* **2016**, 28 (7), 2041—2051.
- (215) Huang, H.; Feng, T.; Gan, Y.; Fang, M.; Xia, Y.; Liang, C.; Tao, X.; Zhang, W. TiC/NiO Core/Shell Nanoarchitecture with Battery-Capacitive Synchronous Lithium Storage for High-Performance Lithium-Ion Battery. ACS Appl. Mater. Interfaces 2015, 7 (22), 11842–11848.
- (216) Sun, J.; Lv, C.; Lv, F.; Chen, S.; Li, D.; Guo, Z.; Han, W.; Yang, D.; Guo, S. Tuning the Shell Number of Multishelled Metal Oxide Hollow Fibers for Optimized Lithium-Ion Storage. *ACS Nano* **2017**, *11* (6), 6186–6193.
- (217) Smith, P. F.; Brady, A. B.; Lee, S.-Y.; Bruck, A. M.; Dooryhee, E.; Wu, L.; Zhu, Y.; Takeuchi, K. J.; Takeuchi, E. S.; Marschilok, A. C. Deliberately Designed Atomic-Level Silver-Containing Interface Results in Improved Rate Capability and Utilization of Silver Hollandite for Lithium-Ion Storage. *ACS Appl. Mater. Interfaces* **2018**, *10* (1), 400–407.
- (218) Bock, D. C.; Tappero, R. V.; Takeuchi, K. J.; Marschilok, A. C.; Takeuchi, E. S. Mapping the Anode Surface-Electrolyte

- Interphase: Investigating a Life Limiting Process of Lithium Primary Batteries. ACS Appl. Mater. Interfaces 2015, 7 (9), 5429–5437.
- (219) Kim, S.; Cho, W.; Zhang, X.; Oshima, Y.; Choi, J. W. A Stable Lithium-Rich Surface Structure for Lithium-Rich Layered Cathode Materials. *Nat. Commun.* **2016**, 7 (1), 1–8.
- (220) Oh, G.; Hirayama, M.; Kwon, O.; Suzuki, K.; Kanno, R. Bulk-Type All Solid-State Batteries with 5 V Class LiNi  $_{0.5}$  Mn  $_{1.5}$  O  $_4$  Cathode and Li  $_{10}$  GeP  $_2$  S  $_{12}$  Solid Electrolyte. *Chem. Mater.* **2016**, 28 (8), 2634–2640.
- (221) Lou, S.; Shen, B.; Zuo, P.; Yin, G.; Yang, L.; Ma, Y.; Cheng, X.; Du, C.; Gao, Y. Electrochemical Performance Degeneration Mechanism of LiCoO<sub>2</sub> with High State of Charge during Long-Term Charge/Discharge Cycling. *RSC Adv.* **2015**, *5* (99), 81235–81242.
- (222) Osaka, T.; Mukoyama, D.; Nara, H. Review—Development of Diagnostic Process for Commercially Available Batteries, Especially Lithium Ion Battery, by Electrochemical Impedance Spectroscopy. *J. Electrochem. Soc.* **2015**, *162* (14), A2529–A2537.
- (223) Patil, S. B.; Kim, I. Y.; Gunjakar, J. L.; Oh, S. M.; Eom, T.; Kim, H.; Hwang, S.-J. Phase Tuning of Nanostructured Gallium Oxide via Hybridization with Reduced Graphene Oxide for Superior Anode Performance in Li-Ion Battery: An Experimental and Theoretical Study. ACS Appl. Mater. Interfaces 2015, 7 (33), 18679—18688.
- (224) Medvedev, A. G.; Mikhaylov, A. A.; Grishanov, D. A.; Yu, D. Y. W.; Gun, J.; Sladkevich, S.; Lev, O.; Prikhodchenko, P. V. GeO2 Thin Film Deposition on Graphene Oxide by the Hydrogen Peroxide Route: Evaluation for Lithium-Ion Battery Anode. *ACS Appl. Mater. Interfaces* **2017**, *9* (10), 9152–9160.
- (225) Wang, Y.; Li, W.; Hu, G.; Peng, Z.; Cao, Y.; Gao, H.; Du, K.; Goodenough, J. B. Electrochemical Performance of Large-Grained NaCrO2 Cathode Materials for Na-Ion Batteries Synthesized by Decomposition of Na2Cr2O7·2H2O. *Chem. Mater.* **2019**, *31* (14), 5214–5223.
- (226) Zamani, N.; Modarresi-Alam, A. R.; Noroozifar, M. Synthesis and Application of Phosphorus/Co3O4—CuO Hybrid as High-Performance Anode Materials for Lithium-Ion Batteries. *ACS Omega* **2018**, *3* (4), 4620—4630.
- (227) Wang, Y.; Cao, L.; Huang, J.; Kou, L.; Li, J.; Wu, J.; Liu, Y.; Pan, L. Improved Li-Storage Properties of Cu2V2O7Microflower by Constructing an in Situ CuO Coating. ACS Sustainable Chem. Eng. 2019, 7 (6), 6267–6274.
- (228) Xiang, J. Y.; Tu, J. P.; Qiao, Y. Q.; Wang, X. L.; Zhong, J.; Zhang, D.; Gu, C. D. Electrochemical Impedance Analysis of a Hierarchical CuO Electrode Composed of Self-Assembled Nanoplates. J. Phys. Chem. C 2011, 115 (5), 2505–2513.
- (229) Rath, P. C.; Patra, J.; Saikia, D.; Mishra, M.; Tseng, C.-M.; Chang, J.-K.; Kao, H.-M. Comparative Study on the Morphology-Dependent Performance of Various CuO Nanostructures as Anode Materials for Sodium-Ion Batteries. *ACS Sustainable Chem. Eng.* **2018**, 6 (8), 10876–10885.
- (230) Liu, Y.; Wang, W.; Gu, L.; Wang, Y.; Ying, Y.; Mao, Y.; Sun, L.; Peng, X. Flexible CuO Nanosheets/Reduced-Graphene Oxide Composite Paper: Binder-Free Anode for High-Performance Lithium-Ion Batteries. ACS Appl. Mater. Interfaces 2013, 5 (19), 9850–9855.
- (231) Venkatachalam, S.; Zhu, H.; Masarapu, C.; Hung, K.; Liu, Z.; Suenaga, K.; Wei, B. In-Situ Formation of Sandwiched Structures of Nanotube/CuxOy/Cu Composites for Lithium Battery Applications. *ACS Nano* **2009**, *3* (8), 2177–2184.
- (232) Wang, C.; Li, Q.; Wang, F.; Xia, G.; Liu, R.; Li, D.; Li, N.; Spendelow, J. S.; Wu, G. Morphology-Dependent Performance of CuO Anodes via Facile and Controllable Synthesis for Lithium-Ion Batteries. ACS Appl. Mater. Interfaces 2014, 6 (2), 1243–1250.
- (233) Klein, F.; Pinedo, R.; Berkes, B. B.; Janek, J.; Adelhelm, P. Kinetics and Degradation Processes of CuO as Conversion Electrode for Sodium-Ion Batteries: An Electrochemical Study Combined with Pressure Monitoring and DEMS. *J. Phys. Chem. C* **2017**, *121* (16), 8679–8691.
- (234) Lu, P.; Li, C.; Schneider, E. W.; Harris, S. J. Chemistry, Impedance, and Morphology Evolution in Solid Electrolyte

- Interphase Films during Formation in Lithium Ion Batteries. J. Phys. Chem. C 2014, 118 (2), 896–903.
- (235) Huang, W.; Boyle, D. T.; Li, Y.; Li, Y.; Pei, A.; Chen, H.; Cui, Y. Nanostructural and Electrochemical Evolution of the Solid-Electrolyte Interphase on CuO Nanowires Revealed by Cryogenic-Electron Microscopy and Impedance Spectroscopy. *ACS Nano* **2019**, 13 (1), 737–744.
- (236) Ogihara, N.; Itou, Y.; Sasaki, T.; Takeuchi, Y. Impedance Spectroscopy Characterization of Porous Electrodes under Different Electrode Thickness Using a Symmetric Cell for High-Performance Lithium-Ion Batteries. *J. Phys. Chem. C* **2015**, *119* (9), 4612–4619.
- (237) Huang, Y. F.; Ruan, W. H.; Lin, D. L.; Zhang, M. Q. Bridging Redox Species-Coated Graphene Oxide Sheets to Electrode for Extending Battery Life Using Nanocomposite Electrolyte. *ACS Appl. Mater. Interfaces* **2017**, *9* (1), 909–918.
- (238) Bojinov, M.; Geronov, Y.; Pistoia, G.; Pasquali, M. Impedance of the Li Electrode in Li/Li x MnO2 Accumulators at Open-Circuit Voltage. *J. Electrochem. Soc.* **1993**, *140* (2), 294–299.
- (239) Wu, M.-S.; Chang, H.-W. Self-Assembly of NiO-Coated ZnO Nanorod Electrodes with Core-Shell Nanostructures as Anode Materials for Rechargeable Lithium-Ion Batteries. *J. Phys. Chem. C* **2013**, *117* (6), 2590–2599.
- (240) Zhou, G.; Wang, D.-W.; Yin, L.-C.; Li, N.; Li, F.; Cheng, H.-M. Oxygen Bridges between NiO Nanosheets and Graphene for Improvement of Lithium Storage. *ACS Nano* **2012**, *6* (4), 3214–3223.
- (241) Park, J. R.; Macdonald, D. D. Impedance Studies of the Growth of Porous Magnetite Films on Carbon Steel in High Temperature Aqueous Systems. *Corros. Sci.* 1983, 23 (4), 295–315.
- (242) MacDonald, D. D.; Pound, B. G.; Lenhart, S. J. The Application of Electrochemical Impedance Spectroscopy for Characterizing the Degradation of Ni(OH)2/NiOOH Electrodes. *J. Power Sources* **1990**, 29 (3), 477–502.
- (243) Justin, P.; Meher, S. K.; Rao, G. R. Tuning of Capacitance Behavior of NiO Using Anionic, Cationic, and Nonionic Surfactants by Hydrothermal Synthesis. *J. Phys. Chem. C* **2010**, *114* (11), 5203–5210.
- (244) Wang, L.; Cao, X.; Xu, L.; Chen, J.; Zheng, J. Transformed Akhtenskite MnO2 from Mn3O4 as Cathode for a Rechargeable Aqueous Zinc Ion Battery. ACS Sustainable Chem. Eng. 2018, 6 (12), 16055–16063.
- (245) Han, S.-D.; Kim, S.; Li, D.; Petkov, V.; Yoo, H. D.; Phillips, P. J.; Wang, H.; Kim, J. J.; More, K. L.; Key, B.; Klie, R. F.; Cabana, J.; Stamenkovic, V. R.; Fister, T. T.; Markovic, N. M.; Burrell, A. K.; Tepavcevic, S.; Vaughey, J. T. Mechanism of Zn Insertion into Nanostructured δ-MnO2: A Nonaqueous Rechargeable Zn Metal Battery. *Chem. Mater.* **2017**, *29* (11), 4874–4884.
- (246) Wang, H.; Mao, N.; Shi, J.; Wang, Q.; Yu, W.; Wang, X. Cobalt Oxide-Carbon Nanosheet Nanoarchitecture as an Anode for High-Performance Lithium-Ion Battery. ACS Appl. Mater. Interfaces 2015, 7 (4), 2882–2890.
- (247) Laman, F. C. Impedance Studies for Separators in Rechargeable Lithium Batteries. *J. Electrochem. Soc.* **1993**, *140* (4), L51–L53.
- (248) Chen, M.; Chen, D.; Liao, Y.; Zhong, X.; Li, W.; Zhang, Y. Layered Lithium-Rich Oxide Nanoparticles Doped with Spinel Phase: Acidic Sucrose-Assistant Synthesis and Excellent Performance as Cathode of Lithium Ion Battery. ACS Appl. Mater. Interfaces 2016, 8 (7), 4575–4584.
- (249) Chen, K.; Xue, D. Room-Temperature Chemical Transformation Route to CuO Nanowires toward High-Performance Electrode Materials. *J. Phys. Chem. C* 2013, 117 (44), 22576–22583.
- (250) Verrelli, R.; Scrosati, B.; Sun, Y.-K.; Hassoun, J. Stable, High Voltage Li0.85Ni0.46Cu0.1Mn1.49O4 Spinel Cathode in a Lithium-Ion Battery Using a Conversion-Type CuO Anode. *ACS Appl. Mater. Interfaces* **2014**, *6* (7), 5206–5211.
- (251) Zhao, K.; Sun, C.; Yu, Y.; Dong, Y.; Zhang, C.; Wang, C.; Voyles, P. M.; Mai, L.; Wang, X. Surface Gradient Ti-Doped MnO2

- Nanowires for High-Rate and Long-Life Lithium Battery. ACS Appl. Mater. Interfaces 2018, 10 (51), 44376-44384.
- (252) Huang, G.; Yin, D.; Zhang, F.; Li, Q.; Wang, L. Yolk@Shell or Concave Cubic NiO-Co3O4@C Nanocomposites Derived from Metal-Organic Frameworks for Advanced Lithium-Ion Battery Anodes. *Inorg. Chem.* **2017**, *56* (16), 9794–9801.
- (253) Huang, J.; Poyraz, A. S.; Lee, S.-Y.; Wu, L.; Zhu, Y.; Marschilok, A. C.; Takeuchi, K. J.; Takeuchi, E. S. Silver-Containing  $\alpha$ -MnO2 Nanorods: Electrochemistry in Na-Based Battery Systems. *ACS Appl. Mater. Interfaces* **2017**, 9 (5), 4333–4342.
- (254) Wang, K.; Zhang, X.; Han, J.; Zhang, X.; Sun, X.; Li, C.; Liu, W.; Li, Q.; Ma, Y. High-Performance Cable-Type Flexible Rechargeable Zn Battery Based on MnO2@CNT Fiber Microelectrode. ACS Appl. Mater. Interfaces 2018, 10 (29), 24573—24582.
- (255) Wang, Z.; Mo, F.; Ma, L.; Yang, Q.; Liang, G.; Liu, Z.; Li, H.; Li, N.; Zhang, H.; Zhi, C. Highly Compressible Cross-Linked Polyacrylamide Hydrogel-Enabled Compressible Zn—MnO2 Battery and a Flexible Battery—Sensor System. *ACS Appl. Mater. Interfaces* **2018**, *10* (51), 44527—44534.
- (256) Sun, W.; Wang, F.; Hou, S.; Yang, C.; Fan, X.; Ma, Z.; Gao, T.; Han, F.; Hu, R.; Zhu, M.; Wang, C. Zn/MnO2 Battery Chemistry With H+ and Zn2+ Coinsertion. J. Am. Chem. Soc. 2017, 139 (29), 9775–9778.
- (257) Reddy, M. V.; Subba Rao, G. V.; Chowdari, B. V. R. Metal Oxides and Oxysalts as Anode Materials for Li Ion Batteries. *Chem. Rev.* 2013, 113 (7), 5364–5457.
- (258) Nakayama, M.; Taki, H.; Nakamura, T.; Tokuda, S.; Jalem, R.; Kasuga, T. Combined Computational and Experimental Study of Li Exchange Reaction at the Surface of Spinel LiMn2O4 as a Rechargeable Li-Ion Battery Cathode. *J. Phys. Chem. C* **2014**, *118* (47), 27245–27251.
- (259) Dedryvère, R.; Foix, D.; Franger, S.; Patoux, S.; Daniel, L.; Gonbeau, D. Electrode/Electrolyte Interface Reactivity in High-Voltage Spinel LiMn1.6Ni0.4O4/Li4Ti5O12 Lithium-Ion Battery. *J. Phys. Chem. C* **2010**, *114* (24), 10999–11008.
- (260) Jiang, Q.; Liu, D.; Zhang, H.; Wang, S. Plasma-Assisted Sulfur Doping of LiMn2O4 for High-Performance Lithium-Ion Batteries. *J. Phys. Chem. C* 2015, 119 (52), 28776–28782.
- (261) Lu, D.; Li, W.; Zuo, X.; Yuan, Z.; Huang, Q. Study on Electrode Kinetics of Li+ Insertion in LixMn2O4 ( $0 \le x \le 1$ ) by Electrochemical Impedance Spectroscopy. *J. Phys. Chem. C* **2007**, *111* (32), 12067–12074.
- (262) Johnston, W. D.; Heikes, R. R.; Sestrich, D. The Preparation, Crystallography, and Magnetic Properties of the LixCo(1-x)O System. *J. Phys. Chem. Solids* **1958**, 7 (1), 1-13.
- (263) Sauvage, F.; Tarascon, J.-M.; Baudrin, E. In Situ Measurements of Li Ion Battery Electrode Material Conductivity: Application to LixCoO2 and Conversion Reactions. *J. Phys. Chem. C* **2007**, *111* (26), 9624–9630.
- (264) Lu, W.; Zhang, J.; Xu, J.; Wu, X.; Chen, L. In Situ Visualized Cathode Electrolyte Interphase on LiCoO2 in High Voltage Cycling. ACS Appl. Mater. Interfaces 2017, 9 (22), 19313–19318.
- (265) Tan, H.; Takeuchi, S.; Bharathi, K. K.; Takeuchi, I.; Bendersky, L. A. Microscopy Study of Structural Evolution in Epitaxial LiCoO2 Positive Electrode Films during Electrochemical Cycling. ACS Appl. Mater. Interfaces 2016, 8 (10), 6727–6735.
- (266) Harilal, M.; Krishnan, S. G.; Pal, B.; Reddy, M. V.; Ab Rahim, M. H.; Yusoff, M. M.; Jose, R. Environment-Modulated Crystallization of Cu2O and CuO Nanowires by Electrospinning and Their Charge Storage Properties. *Langmuir* **2018**, *34* (5), 1873–1882.
- (267) Liu, H.; Li, W.; Shen, D.; Zhao, D.; Wang, G. Graphitic Carbon Conformal Coating of Mesoporous TiO2 Hollow Spheres for High-Performance Lithium Ion Battery Anodes. *J. Am. Chem. Soc.* **2015**, 137 (40), 13161–13166.
- (268) Zhang, L.; Gu, X.; Yan, C.; Zhang, S.; Li, L.; Jin, Y.; Zhao, S.; Wang, H.; Zhao, X. Titanosilicate Derived SiO2/TiO2@C Nanosheets with Highly Distributed TiO2 Nanoparticles in SiO2Matrix as Robust Lithium Ion Battery Anode. ACS Appl. Mater. Interfaces 2018, 10 (51), 44463–44471.

- (269) Wang, Y.-Q.; Gu, L.; Guo, Y.-G.; Li, H.; He, X.-Q.; Tsukimoto, S.; Ikuhara, Y.; Wan, L.-J. Rutile-TiO2 Nanocoating for a High-Rate Li4Ti5O12 Anode of a Lithium-Ion Battery. *J. Am. Chem. Soc.* **2012**, *134* (18), 7874–7879.
- (270) Qiu, J.; Zhang, P.; Ling, M.; Li, S.; Liu, P.; Zhao, H.; Zhang, S. Photocatalytic Synthesis of TiO2 and Reduced Graphene Oxide Nanocomposite for Lithium Ion Battery. ACS Appl. Mater. Interfaces 2012, 4 (7), 3636–3642.
- (271) Sundaramurthy, J.; Aravindan, V.; Suresh Kumar, P.; Madhavi, S.; Ramakrishna, S. Electrospun TiO2 $-\delta$  Nanofibers as Insertion Anode for Li-Ion Battery Applications. *J. Phys. Chem. C* **2014**, *118* (30), 16776-16781.
- (272) Zheng, J.; Liu, L.; Ji, G.; Yang, Q.; Zheng, L.; Zhang, J. Hydrogenated Anatase TiO2 as Lithium-Ion Battery Anode: Size—Reactivity Correlation. *ACS Appl. Mater. Interfaces* **2016**, 8 (31), 20074–20081.
- (273) Salman, M. S.; Park, A. R.; Cha, M. J.; Choi, Y.; Jang, S. K.; Tan, L.; Yoo, P. J.; Choe, W.-S. Lysozyme-Templated Meso-Macroporous Hollow TiO2 for Lithium Ion Battery Anode. ACS Appl. Nano Mater. 2018, 1 (2), 698–710.
- (274) Balogun, M.-S.; Zhu, Y.; Qiu, W.; Luo, Y.; Huang, Y.; Liang, C.; Lu, X.; Tong, Y. Chemically Lithiated TiO2 Heterostructured Nanosheet Anode with Excellent Rate Capability and Long Cycle Life for High-Performance Lithium-Ion Batteries. *ACS Appl. Mater. Interfaces* **2015**, 7 (46), 25991–26003.
- (275) Ha, J. U.; Lee, J.; Abbas, M. A.; Lee, M. D.; Lee, J.; Bang, J. H. Designing Hierarchical Assembly of Carbon-Coated TiO2 Nanocrystals and Unraveling the Role of TiO2/Carbon Interface in Lithium-Ion Storage in TiO2. ACS Appl. Mater. Interfaces 2019, 11 (12), 11391–11402.
- (276) Liu, D.; Yu, Q.; Liu, S.; Qian, K.; Wang, S.; Sun, W.; Yang, X.-Q.; Kang, F.; Li, B. Evolution of Solid Electrolyte Interface on TiO2 Electrodes in an Aqueous Li-Ion Battery Studied Using Scanning Electrochemical Microscopy. *J. Phys. Chem. C* **2019**, 123 (20), 12797–12806.
- (277) Ren, W.; Zhou, W.; Zhang, H.; Cheng, C. ALD TiO2-Coated Flower-like MoS2 Nanosheets on Carbon Cloth as Sodium Ion Battery Anode with Enhanced Cycling Stability and Rate Capability. *ACS Appl. Mater. Interfaces* **2017**, *9* (1), 487–495.
- (278) Deng, J.; Wang, X.; Duan, X.; Liu, P. Facile Preparation of MnO2/Graphene Nanocomposites with Spent Battery Powder for Electrochemical Energy Storage. ACS Sustainable Chem. Eng. 2015, 3 (7), 1330–1338.
- (279) Rashad, M.; Li, X.; Zhang, H. Magnesium/Lithium-Ion Hybrid Battery with High Reversibility by Employing NaV3O8-1.69H2O Nanobelts as a Positive Electrode. ACS Appl. Mater. Interfaces 2018, 10 (25), 21313–21320.
- (280) Wang, L.; Asheim, K.; Vullum, P. E.; Svensson, A. M.; Vullum-Bruer, F. Sponge-Like Porous Manganese(II,III) Oxide as a Highly Efficient Cathode Material for Rechargeable Magnesium Ion Batteries. *Chem. Mater.* **2016**, 28 (18), 6459–6470.
- (281) Truong, Q. D.; Kempaiah Devaraju, M.; Tran, P. D.; Gambe, Y.; Nayuki, K.; Sasaki, Y.; Honma, I. Unravelling the Surface Structure of MgMn2O4 Cathode Materials for Rechargeable Magnesium-Ion Battery. *Chem. Mater.* **2017**, *29* (15), 6245–6251.
- (282) Shi, H.; Zhao, G. Water Oxidation on Spinel NiCo <sub>2</sub> O <sub>4</sub> Nanoneedles Anode: Microstructures, Specific Surface Character, and the Enhanced Electrocatalytic Performance. *J. Phys. Chem. C* **2014**, 118 (45), 25939–25946.
- (283) Bao, J.; Zhang, X.; Fan, B.; Zhang, J.; Zhou, M.; Yang, W.; Hu, X.; Wang, H.; Pan, B.; Xie, Y. Ultrathin Spinel-Structured Nanosheets Rich in Oxygen Deficiencies for Enhanced Electrocatalytic Water Oxidation. *Angew. Chem., Int. Ed.* **2015**, *54* (25), 7399–7404.
- (284) Zhuang, L.; Ge, L.; Yang, Y.; Li, M.; Jia, Y.; Yao, X.; Zhu, Z. Ultrathin Iron-Cobalt Oxide Nanosheets with Abundant Oxygen Vacancies for the Oxygen Evolution Reaction. *Adv. Mater.* **2017**, 29 (17), 1606793.
- (285) He, H.; Berglund, S. P.; Rettie, A. J. E.; Chemelewski, W. D.; Xiao, P.; Zhang, Y.; Mullins, C. B. Synthesis of BiVO 4 Nanoflake

- Array Films for Photoelectrochemical Water Oxidation. J. Mater. Chem. A 2014, 2 (24), 9371–9379.
- (286) Jeong, H. W.; Jeon, T. H.; Jang, J. S.; Choi, W.; Park, H. Strategic Modification of BiVO <sub>4</sub> for Improving Photoelectrochemical Water Oxidation Performance. *J. Phys. Chem. C* **2013**, *117* (18), 9104–9112.
- (287) Lu, B.; Cao, D.; Wang, P.; Wang, G.; Gao, Y. Oxygen Evolution Reaction on Ni-Substituted Co3O4 Nanowire Array Electrodes. *Int. J. Hydrogen Energy* **2011**, *36* (1), 72–78.
- (288) Su, Y.-Z.; Xu, Q.-Z.; Chen, G.-F.; Cheng, H.; Li, N.; Liu, Z.-Q. One Dimensionally Spinel NiCo2O4 Nanowire Arrays: Facile Synthesis, Water Oxidation, and Magnetic Properties. *Electrochim. Acta* 2015, 174, 1216–1224.
- (289) Zhang, T.; Su, J.; Guo, L. Morphology Engineering of WO <sub>3</sub>/BiVO <sub>4</sub> Heterojunctions for Efficient Photocatalytic Water Oxidation. *CrystEngComm* **2016**, *18* (46), 8961–8970.
- (290) Yu, M. Q.; Li, Y. H.; Yang, S.; Liu, P. F.; Pan, L. F.; Zhang, L.; Yang, H. G. Mn  $_3$  O  $_4$  Nano-Octahedrons on Ni Foam as an Efficient Three-Dimensional Oxygen Evolution Electrocatalyst. *J. Mater. Chem. A* **2015**, 3 (27), 14101–14104.
- (291) Si, C.; Zhang, Y.; Zhang, C.; Gao, H.; Ma, W.; Lv, L.; Zhang, Z. Mesoporous Nanostructured Spinel-Type MFe 2 O 4 (M = Co, Mn, Ni) Oxides as Efficient Bi-Functional Electrocatalysts towards Oxygen Reduction and Oxygen Evolution. *Electrochim. Acta* **2017**, 245, 829–838.
- (292) Wei, R.; Fang, M.; Dong, G.; Lan, C.; Shu, L.; Zhang, H.; Bu, X.; Ho, J. C. High-Index Faceted Porous Co <sub>3</sub> O <sub>4</sub> Nanosheets with Oxygen Vacancies for Highly Efficient Water Oxidation. *ACS Appl. Mater. Interfaces* **2018**, *10* (8), 7079–7086.
- (293) Li, M.; Xiong, Y.; Liu, X.; Bo, X.; Zhang, Y.; Han, C.; Guo, L. Facile Synthesis of Electrospun MFe  $_2$  O  $_4$  (M = Co, Ni, Cu, Mn) Spinel Nanofibers with Excellent Electrocatalytic Properties for Oxygen Evolution and Hydrogen Peroxide Reduction. *Nanoscale* **2015**, 7 (19), 8920–8930.
- (294) Chanda, D.; Hnát, J.; Paidar, M.; Bouzek, K. Evolution of Physicochemical and Electrocatalytic Properties of NiCo2O4 (AB2O4) Spinel Oxide with the Effect of Fe Substitution at the A Site Leading to Efficient Anodic O2 Evolution in an Alkaline Environment. *Int. J. Hydrogen Energy* **2014**, 39 (11), 5713–5722.
- (295) Jiang, Z.; Liu, Y.; Jing, T.; Huang, B.; Zhang, X.; Qin, X.; Dai, Y.; Whangbo, M.-H. Enhancing the Photocatalytic Activity of BiVO <sub>4</sub> for Oxygen Evolution by Ce Doping: Ce <sup>3+</sup> Ions as Hole Traps. *J. Phys. Chem. C* **2016**, *120* (4), 2058–2063.
- (296) Zhu, Y.; Zhou, W.; Yu, J.; Chen, Y.; Liu, M.; Shao, Z. Enhancing Electrocatalytic Activity of Perovskite Oxides by Tuning Cation Deficiency for Oxygen Reduction and Evolution Reactions. *Chem. Mater.* **2016**, 28 (6), 1691–1697.
- (297) Wang, W.; Zhang, Y.; Huang, X.; Bi, Y. Engineering the Surface Atomic Structure of FeVO  $_4$  Nanocrystals for Use as Highly Active and Stable Electrocatalysts for Oxygen Evolution. *J. Mater. Chem. A* **2019**, 7 (18), 10949–10953.
- (298) Castro, E. Electrodeposited Ni-Co-Oxide Electrodes:Characterization and Kinetics of the Oxygen Evolution Reaction. *Int. J. Hydrogen Energy* **2000**, 25 (12), 1163–1170.
- (299) Zhang, Z.; Zhang, J.; Wang, T.; Li, Z.; Yang, G.; Bian, H.; Li, J.; Gao, D. Durable Oxygen Evolution Reaction of One Dimensional Spinel CoFe <sub>2</sub> O <sub>4</sub> Nanofibers Fabricated by Electrospinning. *RSC Adv.* **2018**, *8* (10), 5338–5343.
- (300) Nie, Z.-P.; Ma, D.-K.; Fang, G.-Y.; Chen, W.; Huang, S.-M. Concave Bi <sub>2</sub> WO <sub>6</sub> Nanoplates with Oxygen Vacancies Achieving Enhanced Electrocatalytic Oxygen Evolution in near-Neutral Water. *J. Mater. Chem. A* **2016**, *4* (7), 2438–2444.
- (301) Zhang, G.; Yang, J.; Wang, H.; Chen, H.; Yang, J.; Pan, F. Co  $_3$  O  $_{4-\delta}$  Quantum Dots As a Highly Efficient Oxygen Evolution Reaction Catalyst for Water Splitting. ACS Appl. Mater. Interfaces **2017**, 9 (19), 16159–16167.
- (302) Han, H. S.; Shin, S.; Kim, D. H.; Park, I. J.; Kim, J. S.; Huang, P.-S.; Lee, J.-K.; Cho, I. S.; Zheng, X. Boosting the Solar Water

- Oxidation Performance of a BiVO 4 Photoanode by Crystallographic Orientation Control. *Energy Environ. Sci.* **2018**, *11* (5), 1299–1306.
- (303) Zhao, B.; Zhang, L.; Zhen, D.; Yoo, S.; Ding, Y.; Chen, D.; Chen, Y.; Zhang, Q.; Doyle, B.; Xiong, X.; Liu, M. E. T. A Tailored Double Perovskite Nanofiber Catalyst Enables Ultrafast Oxygen Evolution. *Nat. Commun.* **2017**, *8* (1), 14586.
- (304) Wang, H.; Yan, L.; Nakotte, T.; Xu, W.; Zhou, M.; Ding, D.; Luo, H. IrO <sub>2</sub> -Incorporated La <sub>0.8</sub> Sr <sub>0.2</sub> MnO <sub>3</sub> as a Bifunctional Oxygen Electrocatalyst with Enhanced Activities. *Inorg. Chem. Front.* **2019**, *6* (4), 1029–1039.
- (305) Ding, C.; Shi, J.; Wang, D.; Wang, Z.; Wang, N.; Liu, G.; Xiong, F.; Li, C. Visible Light Driven Overall Water Splitting Using Cocatalyst/BiVO4 Photoanode with Minimized Bias. *Phys. Chem. Phys.* **2013**, *15* (13), 4589.
- (306) Parmar, K. P. S.; Kang, H. J.; Bist, A.; Dua, P.; Jang, J. S.; Lee, J. S. Photocatalytic and Photoelectrochemical Water Oxidation over Metal-Doped Monoclinic BiVO 4 Photoanodes. *ChemSusChem* **2012**, 5 (10), 1926–1934.
- (307) Jo, W. J.; Jang, J.-W.; Kong, K.; Kang, H. J.; Kim, J. Y.; Jun, H.; Parmar, K. P. S.; Lee, J. S. Phosphate Doping into Monoclinic BiVO4 for Enhanced Photoelectrochemical Water Oxidation Activity. *Angew. Chem., Int. Ed.* **2012**, *51* (13), 3147–3151.
- (308) Su, J.; Guo, L.; Bao, N.; Grimes, C. A. Nanostructured WO <sub>3</sub>/BiVO <sub>4</sub> Heterojunction Films for Efficient Photoelectrochemical Water Splitting. *Nano Lett.* **2011**, *11* (5), 1928–1933.
- (309) Li, J.; Guo, L.; Lei, N.; Song, Q.; Liang, Z. Metallic Bi Nanocrystal-Modified Defective BiVO 4 Photoanodes with Exposed (040) Facets for Photoelectrochemical Water Splitting. *ChemElectroChem* **2017**, *4* (11), 2852–2861.
- (310) Hong, S. J.; Lee, S.; Jang, J. S.; Lee, J. S. Heterojunction BiVO4/WO3 Electrodes for Enhanced Photoactivity of Water Oxidation. *Energy Environ. Sci.* **2011**, 4 (5), 1781.
- (311) Wang, W.; Zhang, Y.; Wang, L.; Bi, Y. Facile Synthesis of Fe <sup>3+</sup> /Fe <sup>2+</sup> Self-Doped Nanoporous FeVO <sub>4</sub> Photoanodes for Efficient Solar Water Splitting. *J. Mater. Chem. A* **2017**, *5* (6), 2478–2482.
- (312) Wang, S.; Chen, P.; Yun, J.-H.; Hu, Y.; Wang, L. An Electrochemically Treated BiVO 4 Photoanode for Efficient Photoelectrochemical Water Splitting. *Angew. Chem., Int. Ed.* **2017**, *56* (29), 8500–8504.
- (313) Swierk, J. R.; McCool, N. S.; Mallouk, T. E. Dynamics of Electron Recombination and Transport in Water-Splitting Dye-Sensitized Photoanodes. *J. Phys. Chem. C* **2015**, *119* (24), 13858–13867.
- (314) Mirbagheri, N.; Wang, D.; Peng, C.; Wang, J.; Huang, Q.; Fan, C.; Ferapontova, E. E. Visible Light Driven Photoelectrochemical Water Oxidation by Zn- and Ti-Doped Hematite Nanostructures. *ACS Catal.* **2014**, *4* (6), 2006–2015.
- (315) Kim, J. Y.; Magesh, G.; Youn, D. H.; Jang, J.-W.; Kubota, J.; Domen, K.; Lee, J. S. Single-Crystalline, Wormlike Hematite Photoanodes for Efficient Solar Water Splitting. *Sci. Rep.* **2013**, *3* (1), 2681.
- (316) Balamurugan, M.; Yun, G.; Ahn, K.-S.; Kang, S. H. Revealing the Beneficial Effects of FeVO <sub>4</sub> Nanoshell Layer on the BiVO <sub>4</sub> Inverse Opal Core Layer for Photoelectrochemical Water Oxidation. *J. Phys. Chem. C* **2017**, 121 (14), 7625–7634.
- (317) Le Formal, F.; Tétreault, N.; Cornuz, M.; Moehl, T.; Grätzel, M.; Sivula, K. Passivating Surface States on Water Splitting Hematite Photoanodes with Alumina Overlayers. *Chem. Sci.* **2011**, 2 (4), 737–743.
- (318) Cummings, C. Y.; Marken, F.; Peter, L. M.; Upul Wijayantha, K. G.; Tahir, A. A. New Insights into Water Splitting at Mesoporous  $\alpha$ -Fe  $_2$  O  $_3$  Films: A Study by Modulated Transmittance and Impedance Spectroscopies. *J. Am. Chem. Soc.* **2012**, *134* (2), 1228–1234.
- (319) Trześniewski, B. J.; Digdaya, I. A.; Nagaki, T.; Ravishankar, S.; Herraiz-Cardona, I.; Vermaas, D. A.; Longo, A.; Gimenez, S.; Smith, W. A. Near-Complete Suppression of Surface Losses and Total Internal Quantum Efficiency in BiVO 4 Photoanodes. *Energy Environ. Sci.* 2017, 10 (6), 1517–1529.

- (320) Lopes, T.; Andrade, L.; Le Formal, F.; Gratzel, M.; Sivula, K.; Mendes, A. Hematite Photoelectrodes for Water Splitting: Evaluation of the Role of Film Thickness by Impedance Spectroscopy. *Phys. Chem. Chem. Phys.* **2014**, *16* (31), 16515.
- (321) Klotz, D.; Grave, D. A.; Dotan, H.; Rothschild, A. Empirical Analysis of the Photoelectrochemical Impedance Response of Hematite Photoanodes for Water Photo-Oxidation. *J. Phys. Chem. Lett.* **2018**, 9 (6), 1466–1472.
- (322) Shimizu, K.; Lasia, A.; Boily, J.-F. Electrochemical Impedance Study of the Hematite/Water Interface. *Langmuir* **2012**, *28* (20), 7914–7920.
- (323) Mao, L.; Mohan, S.; Mao, Y. Delafossite CuMnO <sub>2</sub> as an Efficient Bifunctional Oxygen and Hydrogen Evolution Reaction Electrocatalyst for Water Splitting. *J. Electrochem. Soc.* **2019**, *166* (6), H233–H242.
- (324) Klahr, B.; Gimenez, S.; Zandi, O.; Fabregat-Santiago, F.; Hamann, T. Competitive Photoelectrochemical Methanol and Water Oxidation with Hematite Electrodes. *ACS Appl. Mater. Interfaces* **2015**, *7* (14), 7653–7660.
- (325) Le Formal, F.; Pendlebury, S. R.; Cornuz, M.; Tilley, S. D.; Grätzel, M.; Durrant, J. R. Back Electron—Hole Recombination in Hematite Photoanodes for Water Splitting. *J. Am. Chem. Soc.* **2014**, 136 (6), 2564–2574.
- (326) Zhao, X.; Hu, J.; Chen, S.; Chen, Z. An Investigation on the Role of W Doping in BiVO 4 Photoanodes Used for Solar Water Splitting. *Phys. Chem. Chem. Phys.* **2018**, 20 (19), 13637–13645.
- (327) Du, Z.; Xiong, D.; Verma, S. K.; Liu, B.; Zhao, X.; Liu, L.; Li, H. A Low Temperature Hydrothermal Synthesis of Delafossite CuCoO <sub>2</sub> as an Efficient Electrocatalyst for the Oxygen Evolution Reaction in Alkaline Solutions. *Inorg. Chem. Front.* **2018**, 5 (1), 183–188
- (328) Hu, J.; Zhao, X.; Chen, W.; Chen, Z. Enhanced Charge Transport and Increased Active Sites on  $\alpha$ -Fe  $_2$  O  $_3$  (110) Nanorod Surface Containing Oxygen Vacancies for Improved Solar Water Oxidation Performance. ACS Omega 2018, 3 (11), 14973–14980.
- (329) Zhang, J.; Eslava, S. Understanding Charge Transfer, Defects and Surface States at Hematite Photoanodes. *Sustain. Energy Fuels* **2019**, 3 (6), 1351–1364.
- (330) Adler, S. B. Mechanism and Kinetics of Oxygen Reduction on Porous La12xSrxCoO32d Electrodes. *Solid State Ionics* **1998**, *111* (1–2), 125–134.
- (331) Cheriti, M.; Kahoul, A. Double Perovskite Oxides Sr2MMoO6 (M = Fe and Co) as Cathode Materials for Oxygen Reduction in Alkaline Medium. *Mater. Res. Bull.* **2012**, *47* (1), 135–141.
- (332) Pei, D.-N.; Gong, L.; Zhang, A.-Y.; Zhang, X.; Chen, J.-J.; Mu, Y.; Yu, H.-Q. Defective Titanium Dioxide Single Crystals Exposed by High-Energy {001} Facets for Efficient Oxygen Reduction. *Nat. Commun.* **2015**, *6* (1), 8696.
- (333) May, K. J.; Fenning, D. P.; Ming, T.; Hong, W. T.; Lee, D.; Stoerzinger, K. A.; Biegalski, M. D.; Kolpak, A. M.; Shao-Horn, Y. Thickness-Dependent Photoelectrochemical Water Splitting on Ultrathin LaFeO3 Films Grown on Nb:SrTiO3. *J. Phys. Chem. Lett.* **2015**, *6*, 977.
- (334) Lee, D.; Jacobs, R.; Jee, Y.; Seo, A.; Sohn, C.; Ievlev, A. V.; Ovchinnikova, O. S.; Huang, K.; Morgan, D.; Lee, H. N. Stretching Epitaxial La0.6Sr0.4CoO3 $-\delta$  for Fast Oxygen Reduction. *J. Phys. Chem. C* **2017**, *121* (46), 25651–25658.
- (335) Crumlin, E. J.; Mutoro, E.; Liu, Z.; Grass, M. E.; Biegalski, M. D.; Lee, Y.-L.; Morgan, D.; Christen, H. M.; Bluhm, H.; Shao-Horn, Y. Surface Strontium Enrichment on Highly Active Perovskites for Oxygen Electrocatalysis in Solid Oxide Fuel Cells. *Energy Environ. Sci.* **2012**, *5* (3), 6081.
- (336) Jin, C.; Lu, F.; Cao, X.; Yang, Z.; Yang, R. Facile Synthesis and Excellent Electrochemical Properties of NiCo2O4 Spinel Nanowire Arrays as a Bifunctional Catalyst for the Oxygen Reduction and Evolution Reaction. *J. Mater. Chem. A* **2013**, *1* (39), 12170.
- (337) Devaguptapu, S. V.; Hwang, S.; Karakalos, S.; Zhao, S.; Gupta, S.; Su, D.; Xu, H.; Wu, G. Morphology Control of Carbon-Free Spinel NiCo  $_2$  O  $_4$  Catalysts for Enhanced Bifunctional Oxygen Reduction

- and Evolution in Alkaline Media. ACS Appl. Mater. Interfaces 2017, 9 (51), 44567–44578.
- (338) Lee, D.; Grimaud, A.; Crumlin, E. J.; Mezghani, K.; Habib, M. A.; Feng, Z.; Hong, W. T.; Biegalski, M. D.; Christen, H. M.; Shao-Horn, Y. Strain Influence on the Oxygen Electrocatalysis of the (100)-Oriented Epitaxial La2NiO4+ $\delta$  Thin Films at Elevated Temperatures. *J. Phys. Chem. C* **2013**, *117* (37), 18789–18795.
- (339) Baran Aydın, E.; Sığırcık, G. Preparations of Different ZnO Nanostructures on TiO2 Nanotube via Electrochemical Method and Its Application in Hydrogen Production. *Int. J. Hydrogen Energy* **2019**, 44 (23), 11488–11502.
- (340) Yuan, M.; Zhu, Y.; Deng, L.; Ming, R.; Zhang, A.; Li, W.; Chai, B.; Ren, Z. IrO <sub>2</sub> TiO <sub>2</sub> Electrocatalysts for the Hydrogen Evolution Reaction in Acidic Water Electrolysis without Activation. *New J. Chem.* **2017**, *41* (14), 6152–6159.
- (341) Khettab, M.; Omeiri, S.; Sellam, D.; Ladjouzi, M. A.; Trari, M. Characterization of LaNiO3 Prepared by Sol–Gel: Application to Hydrogen Evolution under Visible Light. *Mater. Chem. Phys.* **2012**, 132 (2–3), 625–630.
- (342) Zhao, P.; Li, Y.; Li, L.; Bu, S.; Fan, W. Oxygen Vacancy-Modified B-/N-Codoped ZnGa <sub>2</sub> O <sub>4</sub> Nanospheres with Enhanced Photocatalytic Hydrogen Evolution Performance in the Absence of a Pt Cocatalyst. *J. Phys. Chem. C* **2018**, *122* (20), 10737–10748.
- (343) Xu, X.; Azad, A. K.; Irvine, J. T. S. Photocatalytic H2 Generation from Spinels ZnFe2O4, ZnFeGaO4 and ZnGa2O4. *Catal. Today* **2013**, *199*, 22–26.
- (344) Atta, N. F.; Galal, A.; Ali, S. M. The Catalytic Activity of Ruthenates ARuO3 (A= Ca, Sr or Ba) for the Hydrogen Evolution Reaction in Acidic Medium. *Int. J. Electrochem Sci.* **2012**, *7*, 22.
- (345) Yan, X.; Tian, L.; He, M.; Chen, X. Three-Dimensional Crystalline/Amorphous Co/Co <sub>3</sub> O <sub>4</sub> Core/Shell Nanosheets as Efficient Electrocatalysts for the Hydrogen Evolution Reaction. *Nano Lett.* **2015**, *15* (9), 6015–6021.
- (346) Zhao, Y.; Chang, C.; Teng, F.; Zhao, Y.; Chen, G.; Shi, R.; Waterhouse, G. I. N.; Huang, W.; Zhang, T. Defect-Engineered Ultrathin  $\delta$ -MnO  $_2$  Nanosheet Arrays as Bifunctional Electrodes for Efficient Overall Water Splitting. *Adv. Energy Mater.* **2017**, 7 (18), 1700005.
- (347) Zhu, Y.; Zhou, W.; Zhong, Y.; Bu, Y.; Chen, X.; Zhong, Q.; Liu, M.; Shao, Z. A Perovskite Nanorod as Bifunctional Electrocatalyst for Overall Water Splitting. *Adv. Energy Mater.* **2017**, 7 (8), 1602122.
- (348) Crumlin, E. J.; Mutoro, E.; Ahn, S.-J.; la O', G. J.; Leonard, D. N.; Borisevich, A.; Biegalski, M. D.; Christen, H. M.; Shao-Horn, Y. Oxygen Reduction Kinetics Enhancement on a Heterostructured Oxide Surface for Solid Oxide Fuel Cells. *J. Phys. Chem. Lett.* **2010**, *1* (21), 3149–3155.
- (349) Li, Y.; Chen, X.; Yang, Y.; Jiang, Y.; Xia, C. Mixed-Conductor Sr  $_2$  Fe  $_{1.5}$  Mo  $_{0.5}$  O  $_{6-\delta}$  as Robust Fuel Electrode for Pure CO  $_2$  Reduction in Solid Oxide Electrolysis Cell. ACS Sustainable Chem. Eng. 2017, 5 (12), 11403–11412.
- (350) Doyle, R. L.; Lyons, M. E. G. An Electrochemical Impedance Study of the Oxygen Evolution Reaction at Hydrous Iron Oxide in Base. *Phys. Chem. Chem. Phys.* **2013**, *15* (14), 5224.
- (351) Anantharaj, S.; Ede, S. R.; Karthick, K.; Sam Sankar, S.; Sangeetha, K.; Karthik, P. E.; Kundu, S. Precision and Correctness in the Evaluation of Electrocatalytic Water Splitting: Revisiting Activity Parameters with a Critical Assessment. *Energy Environ. Sci.* **2018**, *11* (4), 744–771.
- (352) Zhang, T.; Low, J.; Koh, K.; Yu, J.; Asefa, T. Mesoporous TiO <sup>2</sup> Comprising Small, Highly Crystalline Nanoparticles for Efficient CO <sup>2</sup> Reduction by H <sup>2</sup> O. ACS Sustainable Chem. Eng. **2018**, 6 (1), 531–540.
- (353) Audichon, T.; Napporn, T. W.; Canaff, C.; Morais, C.; Comminges, C.; Kokoh, K. B. IrO <sub>2</sub> Coated on RuO <sub>2</sub> as Efficient and Stable Electroactive Nanocatalysts for Electrochemical Water Splitting. *J. Phys. Chem. C* **2016**, *120* (5), 2562–2573.

- (354) Mahala, C.; Basu, M. Nanosheets of NiCo <sub>2</sub> O <sub>4</sub> /NiO as Efficient and Stable Electrocatalyst for Oxygen Evolution Reaction. *ACS Omega* **2017**, 2 (11), 7559–7567.
- (355) Zhang, Y.; Ding, F.; Deng, C.; Zhen, S.; Li, X.; Xue, Y.; Yan, Y.-M.; Sun, K. Crystal Plane-Dependent Electrocatalytic Activity of Co3O4 toward Oxygen Evolution Reaction. *Catal. Commun.* **2015**, 67, 78–82.
- (356) Poulain, R.; Klein, A.; Proost, J. Electrocatalytic Properties of (100)-, (110)-, and (111)-Oriented NiO Thin Films toward the Oxygen Evolution Reaction. *J. Phys. Chem. C* **2018**, *122* (39), 22252–22263
- (357) Yun, G.; Balamurugan, M.; Kim, H.-S.; Ahn, K.-S.; Kang, S. H. Role of WO  $_3$  Layers Electrodeposited on SnO  $_2$  Inverse Opal Skeletons in Photoelectrochemical Water Splitting. *J. Phys. Chem. C* **2016**. *120* (11), 5906–5915.
- (358) Zheltikov, A. Impedance Spectroscopy: Theory, Experiment, and Applications Second Edition. Evgenij Barsoukov and J. Ross Macdonald (Eds). John Wiley & Sons, Inc., Hoboken, New Jersey, 2005, Pp. 595. *J. Raman Spectrosc.* **2007**, 38 (1), 122–122.
- (359) Ghobadi, A.; Ghobadi, T. G. U.; Karadas, F.; Ozbay, E. Angstrom Thick ZnO Passivation Layer to Improve the Photoelectrochemical Water Splitting Performance of a TiO2 Nanowire Photoanode: The Role of Deposition Temperature. *Sci. Rep.* **2018**, 8 (1), 16322.
- (360) Kim, C. W.; Yeob, S. J.; Cheng, H.-M.; Kang, Y. S. A Selectively Exposed Crystal Facet-Engineered TiO <sub>2</sub> Thin Film Photoanode for the Higher Performance of the Photoelectrochemical Water Splitting Reaction. *Energy Environ. Sci.* **2015**, 8 (12), 3646–3653.
- (361) Hussein, A. M.; Mahoney, L.; Peng, R.; Kibombo, H.; Wu, C.-M.; Koodali, R. T.; Shende, R. Mesoporous Coupled ZnO/TiO <sub>2</sub> Photocatalyst Nanocomposites for Hydrogen Generation. *J. Renewable Sustainable Energy* **2013**, *5* (3), 033118.
- (362) Ren, X.; Sangle, A.; Zhang, S.; Yuan, S.; Zhao, Y.; Shi, L.; Hoye, R. L. Z.; Cho, S.; Li, D.; MacManus-Driscoll, J. L. Photoelectrochemical Water Splitting Strongly Enhanced in Fast-Grown ZnO Nanotree and Nanocluster Structures. *J. Mater. Chem. A* **2016**, *4* (26), 10203–10211.
- (363) Alves, V. A.; da Silva, L. A.; Boodts, J. F. C. Surface Characterisation of IrO2/TiO2/CeO2 Oxide Electrodes and Faradaic Impedance Investigation of the Oxygen Evolution Reaction from Alkaline Solution. *Electrochim. Acta* 1998, 44 (8), 1525–1534.
- (364) Tang, P.; Arbiol, J. Engineering Surface States of Hematite Based Photoanodes for Boosting Photoelectrochemical Water Splitting. *Nanoscale Horiz* **2019**, *4*, 1256–1276.
- (365) Bisquert, J. Theory of the Impedance of Charge Transfer via Surface States in Dye-Sensitized Solar Cells. *J. Electroanal. Chem.* **2010**, *646* (1), 43–51.
- (366) Hens, Z.; Gomes, W. P. The Electrochemical Impedance of One-Equivalent Electrode Processes at Dark Semiconductor/Redox Electrodes Involving Charge Transfer through Surface States. 2. The n-GaAs/Fe <sup>3+</sup> System as an Experimental Example. *J. Phys. Chem. B* **1999**, *103* (1), 130–138.
- (367) Leng, W. H.; Zhang, Z.; Zhang, J. Q.; Cao, C. N. Investigation of the Kinetics of a TiO <sub>2</sub> Photoelectrocatalytic Reaction Involving Charge Transfer and Recombination through Surface States by Electrochemical Impedance Spectroscopy. *J. Phys. Chem. B* **2005**, *109* (31), 15008–15023.
- (368) Vanmaekelbergh, D.; Cardon, F. Calculation of the Electrical Impedance Associated with the Surface Recombination of Free Carriers at an Illuminated Semiconductor/Electrolyte Interface. *J. Phys. D: Appl. Phys.* **1986**, *19* (4), 643–656.